



Renato Bichara Vieira

**Thermography Applied to the Study of
Fatigue in Polycarbonate**

Dissertação de Mestrado

Thesis presented to the Programa de Pós-Graduação em Engenharia Mecânica of the Departamento de Engenharia Mecânica do Centro Técnico Científico da PUC-Rio, as partial fulfillment of the requirements for the degree of Mestre.

Advisor: Prof. José Luiz de França Freire

Rio de Janeiro
April 2016



Renato Bichara Vieira

**Thermography Applied to the Study of
Fatigue in Polycarbonate**

Thesis presented to the Programa de Pós-Graduação em Engenharia Mecânica of the Departamento de Engenharia Mecânica do Centro Técnico Científico da PUC-Rio, as partial fulfillment of the requirements for the degree of Mestre.

Prof. José Luiz de França Freire

Advisor

Departamento de Engenharia Mecânica – PUC-Rio

Prof. Jaime Tupiassú Pinho de Castro

Departamento de Engenharia Mecânica – PUC-Rio

Prof. Sergio Damasceno Soares

Centro de Pesquisas da PETROBRAS - CENPES

Prof. Arthur Martins Barbosa Braga

Departamento de Engenharia Mecânica – PUC-Rio

Prof. Marcio da Silveira Carvalho

Coordenador Setorial do Centro Técnico Científico – PUC-Rio

Rio de Janeiro, Abril, 2016

All rights reserved.

Renato Bichara Vieira

Graduated in mechanical engineering in 2013 at the Pontifical Catholic University of Rio de Janeiro. Worked since then in the area of experimental stress analysis, specifically with the various applications of thermography.

Ficha Catalográfica

Vieira, Renato Bichara

Thermography applied to the study of fatigue in polycarbonate. / Renato Bichara Vieira; orientador: José Luiz de França Freire. – 2016.

139 f. : il.(color.) ; 30 cm

Dissertação (mestrado)-Pontifícia Universidade Católica do Rio de Janeiro, Departamento de Engenharia Mecânica, 2016.

Inclui Bibliografia

1. Engenharia mecânica – Teses. 2. Termografia Infravermelha. 3. Fadiga. 4. Policarbonato. 5. Análise Termoelástica de Tensões. 6. Método Termográfico. 7. Fator de Concentração de Tensões. 8. Limite de Fadiga. 9. Curva de Wöhler. 10. Fator de Intensidade de Tensões. 11. Lei de Paris. I. Freire, José Luiz de França. II. Pontifícia Universidade Católica do Rio de Janeiro. Departamento de Engenharia Mecânica. III. Título.

CDD: 621

Acknowledgments

I would like to thank my advisor Professor José Luiz de França Freire for all his teachings, not only academic, but for all the life lessons as well.

I have to thank CNPq (Conselho Nacional de Desenvolvimento Científico e Tecnológico) and FAPERJ (Fundação de Amparo à Pesquisa do Estado do Rio de Janeiro) for their financial support, through the scholarships I was awarded.

I want to thank my family, especially my mother Thais and my father Ronaldo, for all the unconditional support, love and help they provided me. They are my inspiration and my reference.

Furthermore, I would like to thank my laboratory colleagues Felipe, Jesus, Jorge, Marco and Vitor for making the process less straining. A special thanks goes to Giancarlo, for the indispensable help during most of the experiments.

I have to thank ITUC, in special Adrian and Ana Rosa, for the support during some of the experiments and for letting me use their equipment.

Finally, I like to give a big thanks to my friends, who helped me indirectly in the process of getting my master's degree. They are one major pillar on which I support my life. Each one of them know who they are.

Abstract

Vieira, Renato Bichara; Freire, José Luiz de França (Advisor). **Thermography Applied to the Study of Fatigue in Polycarbonate**. Rio de Janeiro, 2016. 139p. MSc. Dissertation - Departamento de Engenharia Mecânica, Pontifícia Universidade Católica do Rio de Janeiro.

The theoretical basis and the experimental work done in order to assess the suitability of thermography as a tool in the study of fatigue crack initiation and propagation were discussed. In doing so, the fatigue properties of a polycarbonate sheet (PALSUN™), free from residual stresses, were determined using a range of different thermographic techniques. Active thermography was used to locate hot spot areas where fatigue is bound to happen. Thermoelastic stress analysis (TSA) was used to measure the stress fields and stress concentration factors that influence the initiation of cracks. The thermographic method was used to study the fatigue behavior of polycarbonate, determining the fatigue limit and the Wöhler coefficients in the SN approach for crack initiation. TSA was, again, used to measure stress intensity factors for mode I cracks propagated in keyhole specimens and to determine the Paris coefficients. A low-cost micro-bolometric infrared camera (FLIR A655sc) was used in all these applications combined with either the manufacturer's software (ResearchIR) or a, relatively new, commercial TSA processing software (Deltatherm2 from Stress Photonics Inc.). The practical results obtained were: the stress concentration factor of the keyhole specimens, which fell in the range of 3 to 3.25; the fatigue limit of the polycarbonate sheet determined to be in the range of 9 - 13MPa; the Wöhler curve defined by the fatigue exponent $m= 1.316$ and fatigue coefficient $C= 1.75 \cdot 10^6$ MPa; as well as the Paris law for, second phase mode I cracks, described by the range of coefficients $\alpha= 0.0004 - 0.0011$ mm/cycle and $m= 2.4 - 3.4$ for slightly variable loading conditions. Through the comparison of these results with literature predictions and classic methodologies results, the author could conclude that thermography is indeed a very powerful tool for the study of fatigue. Not only that, but demonstrated the power of the combination of low-cost, recently developed infrared cameras and new software as an inexpensive and effective option for these applications.

Keywords

Infrared Thermography; Fatigue; Polycarbonate; Thermoelastic Stress Analysis; Thermographic Method; Stress Concentration Factor; Fatigue Limit; Wöhler Curve; Stress Intensity Factor; Paris Law.

Resumo

Vieira, Renato Bichara; Freire, José Luiz de França (Orientador). **Termografia Aplicada ao Estudo de Fadiga em Policarbonato**. Rio de Janeiro, 2016. 139p. Dissertação de Mestrado - Departamento de Engenharia Mecânica, Pontifícia Universidade Católica do Rio de Janeiro.

As bases teóricas e o trabalho experimental desenvolvido na validação da termografia como ferramenta de estudo de iniciação e propagação de trincas por fadiga foram descritas. As propriedades de fadiga de uma placa de policarbonato (PALSUN™) isenta de tensões residuais foram determinadas usando-se diferentes técnicas termográficas. A termografia ativa foi usada na localização de pontos críticos onde o mecanismo de fadiga estará presente. A análise termográfica de tensões (TSA) foi usada para medir os campos de tensão e fatores de concentração de tensão que influenciam o surgimento de trincas. O método termográfico foi usado na determinação do limite de fadiga e dos coeficientes da curva de Wöhler no método SN de projeto contra iniciação de trincas. A TSA foi, novamente, usada para determinação de fatores de intensidade de tensão e na determinação dos coeficientes da lei de Paris. Em todos os experimentos, uma câmera infravermelha micro bolométrica de baixo custo (FLIR A655sc) foi usada em conjunto com o *software* da FLIR (ResearchIR) ou com um novo *software* comercial de processamento de dados de TSA (Deltatherm2 da Stress Photonics Inc.). Os resultados obtidos foram: o fator de concentração de tensão do espécime tipo *keyhole* na faixa de 3 a 3.25; o limite de fadiga determinado na faixa 9 -13MPa; a curva de Wöhler, definida pelo expoente de fadiga $m= 1.316$ e o coeficiente de fadiga $C= 1.75 \cdot 10^6$ MPa; os coeficientes da lei de Paris para a fase 2 de trincas propagadas em modo I, nas faixas $\alpha= 0.0004 - 0.0011$ mm/ciclo e $m= 2.4 - 3.4$ para pequenas variações nas condições de carregamento. Com a comparação desses resultados à literatura e com resultados obtidos mediante uso de métodos clássicos, o autor pôde concluir que a termografia é uma técnica muito poderosa no estudo de fadiga. Não só isso, mas demonstrou a possibilidade do uso de novas tecnologias, mais baratas, para câmeras infravermelhas de baixo custo em combinação com novas soluções de *software* para realização desses estudos.

Palavras chaves

Termografia Infravermelha; Fadiga; Policarbonato; Análise Termoelástica de Tensões; Método Termográfico; Fator de Concentração de Tensões; Limite de Fadiga; Curva de Wöhler; Fator de Intensidade de Tensões; Lei de Paris.

Contents

1	Introduction	16
2	Thermography	19
2.1	Introduction	19
2.2	Infrared Thermography	20
2.2.1	Principles	20
2.2.2	Infrared Sensors	24
2.3	Active Thermography	26
2.4	Passive Thermography and Thermoelastic Stress Analysis (TSA)	26
2.4.1	Physics of TSA, the Thermoelastic Effect	27
2.4.2	Calibration and Practical Application of TSA	28
2.4.3	Data Acquisition and Interpretation	29
2.4.4	'DeltaTherm 2' Software Peculiarities	30
2.4.5	Applications of TSA – Bibliographical Review	31
3	Brief Fatigue and Polycarbonate (PC) Review	32
3.1	Review of Basic Fatigue Concepts	32
3.1.1	Fatigue Crack Initiation and the Wohler curve	32
3.1.2	Stress Concentration	33
3.1.3	The Mean Stress Effect	34
3.1.4	Fatigue Crack Growth and Linear Elastic Fracture Mechanics	36
3.2	Polycarbonate Properties	40
3.2.1	Polycarbonate in Infrared Thermography	41
3.2.2	Polycarbonate in Fatigue Studies	41
4	Pre-Experimental Work	48
4.1	Introduction	48
4.2	The Specimens	48
4.2.1	Loading Cautions	49
4.2.2	Specimen Preparation	49
4.3	Cyclic Loading Machine	51
4.4	General Experimental Procedures and Cautions	52
4.4.1	Machine Cautions	52
4.4.2	Infrared Camera Cautions	53
5	Thermography Applied to Fatigue Crack Initiation	55
5.1	Locating Critical Points	55
5.2	Determining Stress Concentration Factors	56

5.2.1	Approach 1 – Simple Extrapolation of Line Data	56
5.2.2	Approach 2 – Stress Function and Principal Stresses Separation	61
5.3	Measuring Fatigue Limit Using Thermography	64
5.4	Determination of the Fatigue Curve Using Thermography	68
5.4.1	Φ Determination	70
5.4.2	SN curve determination	71
5.4.3	SN curve verification	74
6	Thermography Applied to Fatigue Crack Growth	76
6.1	Measuring Stress Intensity Factors Using TSA	76
6.1.1	The SIF Calculation Algorithm	76
6.1.2	Algorithm Inputs	77
6.1.3	Crack Tip Position Estimation and Point Coordinates Assignment	78
6.1.4	Model Validity Limits Verification	80
6.1.5	Error Function Construction and Minimization	81
6.1.6	SIF Calculation and Actual Crack Tip Location	83
6.2	Algorithm verification and Use	84
6.2.1	Numerically Generated TSA Data	84
6.2.2	SIF Measurements	85
6.3	Measuring the Crack Growth Rate	86
6.3.1	Crack Tip Accuracy of the Algorithm	86
6.3.2	da/dN Straight from Temperature Rise	88
6.4	Measuring da/dN vs ΔK_I Curves	90
7	Final Considerations and Conclusions	96
7.1	Final Considerations	96
7.2	Conclusions	100
8	Bibliography	101
Appendix 1	Simple Test on Defect Location by Active Thermography	107
Appendix 2	Simple Test on Monitoring Cracks in Welded Joints	110
Appendix 3	PALSUN™ Polycarbonate Datasheet and Tensile Tests	113
Appendix 4	Measuring the Keyhole K_t with DIC and Photoelasticity	116
Appendix 5	Finite Elements Analysis of the Keyhole Specimen	121
Appendix 6	Photos of the Specimens	125

List of Figures

Figure 1.1: Diagram showing how thermography techniques are divided.	16
Figure 1.2: Evolution of citations of Photoelasticity, TSA and DIC found by google.	17
Figure 1.3: Summary of fatigue studies throughout this work.	17
Figure 2.1: My family as seen through a thermal camera.	19
Figure 2.2: Plot of Planck's Law.	21
Figure 2.3: Atmosphere transmittance and atmospheric windows [2].	23
Figure 2.4: Cross section view of a microbolometer.	25
Figure 2.5: Camera FLIR A655sc, used in most of this work.	26
Figure 2.6: Typical TSA test procedure, adapted from [17].	29
Figure 2.7: a) Magnitude and b) Phase maps of a TSA test of a c) Notched aluminum plate, [17].	30
Figure 2.8: Screenshot of the DeltaTherm 2 interface.	31
Figure 3.1: Typical SN curve, using Juvinall's estimations for steel ($S_R=1000\text{MPa}$).	32
Figure 3.2: Concept of force lines.	33
Figure 3.3: Schematic Goodman's curve.	35
Figure 3.4: Crack opening modes.	37
Figure 3.5: Schematic da/dN curve.	39
Figure 3.6: Paris law curves showing temperature effect, adapted from [52].	42
Figure 3.7: da/dN vs ΔK curves for three different thicknesses, adapted from [54].	43
Figure 3.8: Map of crack initiation mechanism, adapted from [58].	45
Figure 3.9: SN curves for virgin and pre-stressed polycarbonate specimens, adapted from [60].	45
Figure 3.10: a) SN curve for polycarbonate specimens; b) Damage Curve, adapted from [61].	46
Figure 3.11: a) isothermal; b) non-isothermal fatigue curves for polycarbonate, adapted from [62].	46
Figure 3.12: Measured and predicted SN curves for polycarbonate, adapted from [63].	47
Figure 4.1: Dimensions of the constant radius specimens.	48

Figure 4.2: Dimensions of the Keyhole specimens.	49
Figure 4.3: Constant radius specimen mounted with custom grips.	49
Figure 4.4: a) Specimen before annealing. b) After annealing.	50
Figure 4.5: Photo of the pneumatic loading machine setup.	51
Figure 4.6: Screenshot of the program controlling the pneumatic machine.	52
Figure 5.1: Cracked T-shaped specimen and critical points, adapted from [17].	55
Figure 5.2: a) TSA magnitude map and b) critical line plot for CR specimen under $\Delta\sigma=8.18\text{MPa}$.	56
Figure 5.3: Calibration Stress vs TSA magnitude graph for 5 different $\Delta\sigma$.	57
Figure 5.4: a) TSA magnitude map; b) TSA phase map of a keyhole specimen.	57
Figure 5.5: Magnitude line data for the keyhole specimen.	58
Figure 5.6: Phase line data for the keyhole specimen.	58
Figure 5.7: Magnitude data corrected by phase angle.	59
Figure 5.8: Treated TSA data points for keyhole specimen.	59
Figure 5.9: Normalized stress vs distance from notch plot for keyhole.	60
Figure 5.10: Curve-fitted TSA data for keyhole specimen.	60
Figure 5.11: Area, in gray, for stress function fitting.	61
Figure 5.12: Fitted σ_θ field.	62
Figure 5.13: Fitted stress components for line ahead of notch.	63
Figure 5.14: TSA, DIC and Photoelasticity results for the line ahead of notch.	64
Figure 5.15: T vs N curve for cyclic load above the fatigue limit, adapted from [69].	65
Figure 5.16: Loading steps for fatigue limit evaluation.	66
Figure 5.17: T(n) vs cycles points for 4 different load levels.	66
Figure 5.18: Thermographic image at the 7th load level.	67
Figure 5.19: T(N) vs σ_a eq for polycarbonate.	68
Figure 5.20: Illustration of the testing procedure for Risitano method, adapted from [69].	70
Figure 5.21: T(n) vs cycles graph for Φ measurement (~25000cycles = approximately 1.5h test).	71

Figure 5.22: T(n) vs cycles graph of first specimen for SN curve determination.	72
Figure 5.23: T(n) vs cycles graphs of second specimen for SN curve determination.	73
Figure 5.24: SN curve measured via thermography.	74
Figure 5.25: SN curve with all data points.	74
Figure 6.1: Flowchart of the SIF calculation algorithm.	77
Figure 6.2: a)The magnitude map around a crack and b)Typical y vs $1/S^2$ plot.	79
Figure 6.3: a)The phase map around a crack and b)Typical phase vs x plot.	79
Figure 6.4: a)The radial direction where the curves are plotted and b)Typical $1/S^2$ vs r plot	81
Figure 6.5: a)Illustration of Nelder-mead method for $x \in R^2$.	82
Figure 6.6: a)Numerically generated TSA data for crack tip at (-3,-1) and b)Calculated model for estimated crack tip at (-3,0).	84
Figure 6.7: Selected data points for SIF calculation of a 14.1mm crack.	85
Figure 6.8: $\Delta K_I/\Delta P$ vs a plot for all experimental techniques and FEM	86
Figure 6.9: Determined by TSA (red) and measured with photos (green) cracks.	87
Figure 6.10: Position of 11 points along the crack path.	88
Figure 6.11: ΔT vs N plot for 11 points along crack path (left) and integration areas for curves 3, 6 and 10 (right).	89
Figure 6.12: Comparison between $\Delta T/\Delta P$ and da/dN .	90
Figure 6.13: da/dN (photos and TSA algorithm) vs ΔK_I (TSA algorithm) plot for first experiment.	91
Figure 6.14: da/dN (TSA algorithm) vs ΔK_I (TSA algorithm and FEA) plot for second experiment.	93
Figure 6.15: da/dN (temperature and photos) vs ΔK_I (FEA) plot for third experiment.	94
Figure 6.16: Plot of all da/dN results and references.	94
Figure A1.1: a)Composite and b)steel specimens for defect detection experiment.	107

Figure A1.2: a)Thermographic image and b)Temperature profile for the composite specimen.	108
Figure A1.3: a)Thermographic image and b)temporal plot of the steel specimen.	109
Figure A2.1: Welded Joint, steel specimen.	110
Figure A2.2: Development of stresses on welded specimen's surface.	110
Figure A2.3: Horizontal position of maximum stress region throughout the cycles.	111
Figure A2.4: TSA vs cycles curves for the maximum stress points.	112
Figure A2.5: Damage for all points along the horizontal critical line.	112
Figure A3.1: PALSUN Datasheet.	113
Figure A3.2: Tensile specimen dimensions.	114
Figure A3.3: Stress vs displacement plots for a)CR and b)Parallel tensile specimens.	114
Figure A3.4: Stress vs Strain curve for the tensile specimen.	115
Figure A4.1: Series of Photoelastic photos.	116
Figure A4.2: Normalized resulting photoelastic line data ahead of the notch.	117
Figure A4.3: DIC pattern.	118
Figure A4.4: DIC principal strain field result.	119
Figure A4.5: DIC stress results ahead of the notch.	119
Figure A4.6: DIC fitted principal stress ahead of the notch.	120
Figure A5.1: Meshed symmetric model for FEA of the keyhole specimen.	121
Figure A5.2: FEA resulting σ_y map for the keyhole specimen.	121
Figure A5.3: K_t vs thickness plot for the keyhole specimen.	122
Figure A5.4: Meshed model for SIF evaluation of the keyhole specimen.	122
Figure A5.5: FEA resulting σ_y map for cracked (a=10mm) keyhole specimen.	123
Figure A5.6: K_I/P vs thickness plot for the cracked a=10mm) keyhole specimen.	123
Figure A5.7: K_I/P vs a plot for the keyhole specimen.	124

Figure A6.1: Fracture surface of CR tensile specimen after tensile test.	126
Figure A6.2: Fracture surface of tensile specimen after tensile test.	126
Figure A6.3: Fracture surface of CR tensile specimen after fatigue testing.	127
Figure A6.4: Fracture surface of CR tensile specimen after fatigue testing.	127
Figure A6.5: Fracture surface of CR tensile specimen after fatigue bending testing.	128
Figure A6.6: Fracture surface of CR tensile specimen after fatigue testing.	128
Figure A6.7: Fracture surface of Keyhole specimen after fatigue testing Part 1.	129
Figure A6.8: Fracture surface of Keyhole specimen after fatigue testing Part 2.	129
Figure A6.9: Fracture surface of Keyhole specimen after fatigue testing Part 3.	130
Figure A6.10: Fracture surface of Keyhole specimen after fatigue testing.	130
Figure A6.11: Fatigue crack propagated in a Keyhole specimen.	131
Figure A6.12: Fatigue crack propagated in a Keyhole specimen (Tip detail).	131
Figure A6.13: Fatigue crack propagated in a Keyhole specimen.	132
Figure A6.14: Fatigue crack propagated in a Keyhole specimen (Tip detail).	132
Figure A6.15: Fatigue crack propagated in a Keyhole specimen.	133
Figure A6.16: Fatigue crack propagated in a Keyhole specimen (Tip detail).	133
Figure A6.17: Fatigue crack propagated in a Keyhole specimen.	134
Figure A6.18: Fatigue crack propagated in a Keyhole specimen (Tip detail).	134
Figure A6.19: Fatigue crack propagated in a Keyhole specimen.	135
Figure A6.20: Fatigue crack propagated in a Keyhole specimen (Tip detail).	135

Figure A6.21: Fretting damage and crack initiation in a CR tensile specimen.	136
Figure A6.22: Fretting damage and crack initiation in a CR tensile specimen.	136
Figure A6.23: Fretting crack in a CR tensile specimen (front view).	137
Figure A6.24: Fretting crack in a CR tensile specimen (oblique view).	137
Figure A6.25: Fretting fracture surface.	138
Figure A6.26: Fretting fracture surface (zoom).	138
Figure A6.27: Fretting fracture surface (initiation detail).	139

List of Tables

Table 2.1: Emissivity of some materials and paints.	23
Table 3.1: Average values of some polycarbonate properties.	40
Table 3.2: Reported values of Paris coefficients at various temperatures, adapted from [52].	42
Table 3.3: Paris coefficients reported for different stress ratios and thicknesses, adapted from [55].	44
Table 4.1: Temperatures and times of the adapted annealing heat treatment.	50
Table 5.1: Results for the K_I of the keyhole specimen.	64
Table 5.2: Summarized results for the fatigue limit test.	67
Table 5.3: Results of first specimen for SN curve determination.	72
Table 5.4: Results of second specimen for SN curve determination.	73
Table 6.1: Results for the SIF measurement using TSA, DIC and FEM.	85
Table 6.2: Results for crack tip position and crack length.	87
Table 6.3: Damage parameter result for 11 points along crack path.	89
Table 6.4: Results for the first crack propagation da/dN test.	91
Table 6.5: Results for the second crack propagation da/dN test.	92
Table 6.6: Results for the third crack propagation da/dN test.	93
Table A4.1: Fringe distance from notch tip.	116

1

Introduction

Thermography is a research field, which consists in using infrared radiation in order to measure the temperature map of a surface using infrared radiation. Figure 1.1 shows a diagram explaining how this field is usually divided into active and passive thermography and what techniques are used throughout this thesis.

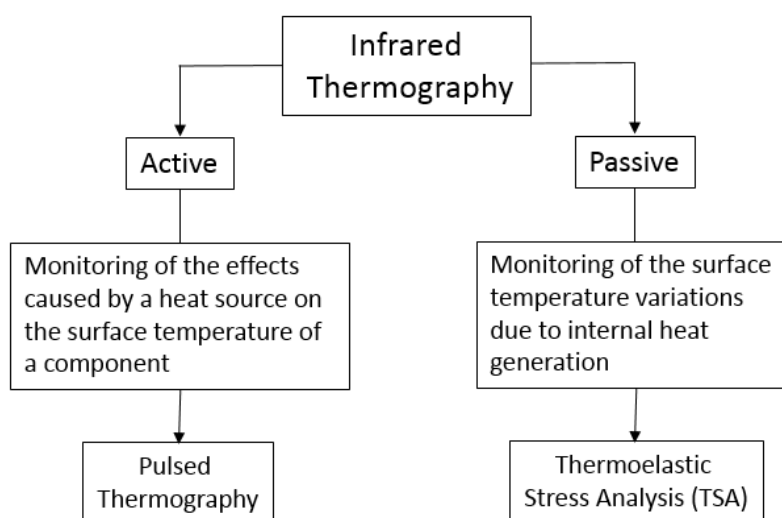


Figure 1.1: Diagram showing how thermography techniques are divided.

TSA is a relatively new experimental technique for measuring stress fields based on the thermoelastic effect, caused by cyclic loading. Figure 1.2 shows the evolution of citations found in a Google search¹ of three optical experimental mechanics techniques between 1960 and 2008. Although DIC had a spectacular ascension in the past decades, TSA shows an stabilization and a promise of a comeback, specially since the advent of the micro-bolometer and the advancements that made infrared detectors costs drop an order of magnitude.

Since the technique relies on the internal heat generation caused by cyclic loading, it has a natural connection with fatigue studies. This relationship has been used before, and is used in this work again.

The study of fatigue is usually divided into two main topics, the initiation of a crack and its growth. Figure 1.3 shows a diagram summarizing how fatigue studies are explored throughout the next chapters.

¹ <https://books.google.com/ngrams>

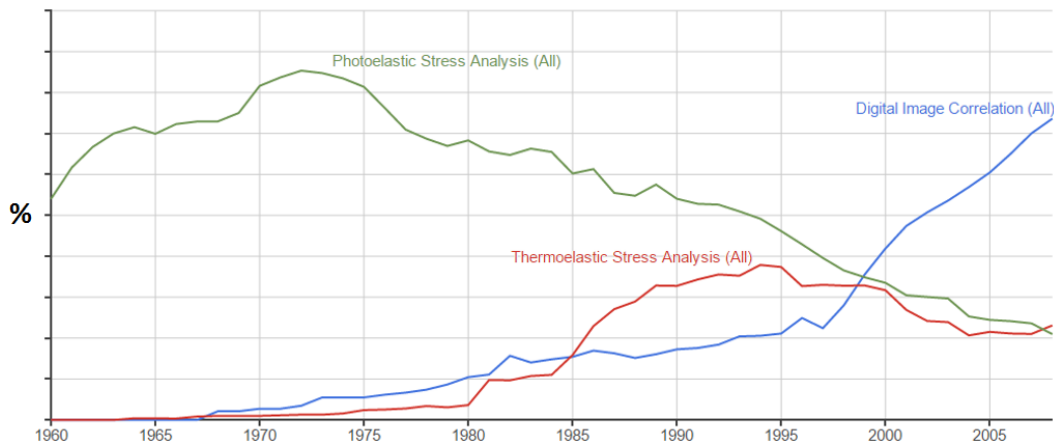


Figure 1.2: Evolution of citations of Photoelasticity, TSA and DIC found by google.

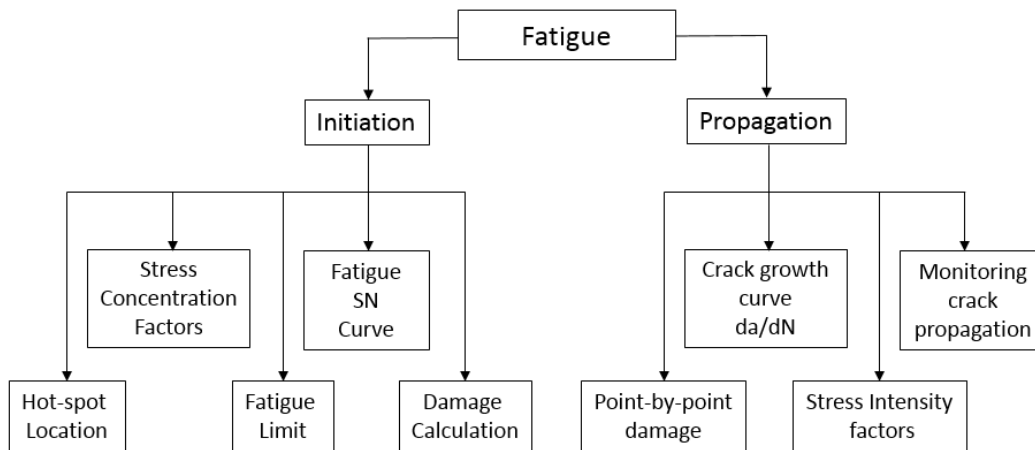


Figure 1.3: Summary of fatigue studies throughout this work.

The main objective of this work can be simply put as the assessment of the suitability of thermography, and the use of an inexpensive equipment combined with a new processing software, for the study of the fatigue behavior of polycarbonate. In order to accomplish that, a series of experiments was conducted and divided into 6 chapters and 5 appendixes summarized below.

Chapter 2 presents a review of thermography theory and experimental applications, from active to passive thermography passing through the workings of typical detectors and specifics of the equipment used in the tests described later.

Chapter 3 briefly reviews simple fatigue concepts and presents a bibliographical review of the results found for polycarbonate. The importance of this material and its fatigue properties are discussed as well.

Chapter 4 summarizes the experimental procedures and cautions related to the load-testing machine and to the infrared camera used in this investigation. It also shows the specimens used and the preparations needed.

Chapter 5 starts reporting the experimental phase of the work, discussing the use of thermography for the study of fatigue crack initiation. From hotspot detection all the way to acquiring SN data and fatigue properties of the material, such as the fatigue limit.

Chapter 6 continues reporting the experimental work, stepping into the fatigue crack growth study. It presents the development of an algorithm for stress intensity range measurement as well as the application of thermography in measuring crack growth fatigue curves for polycarbonate.

Finally, Chapter 7 summarizes all the conclusions made throughout the previous chapters and evaluates the suitability of the procedures used in the study of the fatigue behavior of polycarbonate.

Six Appendixes are located at the end of the text, showing experiments on defect location, crack growth monitoring, material characterization of the polycarbonate sheet, measurement of stress concentration factors using digital image correlation (DIC) and photoelasticity, finite elements analysis of the specimen used for fatigue crack propagation studies and the final appendix showing photos of all specimens (fractured and not-fractured).

2

Thermography

2.1

Introduction

Thermography is a specific area of study within the large field of temperature measurements. It consists of using thermal cameras in order to measure the temperature distribution of an object's surface. In general, it can be split into two different types of experiments, active and passive thermography, which will be explained in further subchapters.

The images generated in thermography, usually called thermograms, use pseudo-color techniques to display the temperature variations. This way, a color is attributed to each temperature level, continuously or discretely, making it much easier for humans to notice the intensity variations. Figure 2.1 was taken at the Deutsche Museum in Munich, and shows my family. It is easy to see the areas where the temperature is higher, because of the colors assigned.



Figure 2.1: My family as seen through a thermal camera.

In order to know the exact values, in degrees, a scale is required to correlate each one of the colors to a specific temperature level. In the picture above, the scale is missing.

The most common type of thermal camera uses infrared radiation levels to infer the temperature of a surface. Because of that, this work focuses on the use of infrared thermography.

2.2

Infrared Thermography

William Herschel's first observations of the infrared (IR) spectrum, in 1800, measured the "power" of the heat radiation of the below-red wavelengths of the electromagnetic spectrum. He concluded that the invisible portion of light carried more "power" than the visible. Because of that, infrared radiation became the most common and efficient way of measuring temperature in no-contact applications [1].

2.2.1

Principles

Any object with temperature above 0K will emit radiation. For temperatures below 773K, this radiation will lie completely within the IR wavelengths (900 – 14000nm). In addition to emitting radiation, a body will react to it in three different ways, depending on its properties. It will absorb, reflect and transmit portions of the radiation. This behavior originates the Total Radiation Law, which can be written as: [2]

$$\mathbf{1} = \alpha + \rho + \tau \quad (2.1)$$

where α , ρ and τ are the coefficients that describe the object's incident energy absorption, reflection and transmission respectively.

Each object will have a different set of coefficients depending on its properties, for example, a perfect blackbody would have $\rho=\tau=0$ and $\alpha=1$, since, by definition, it absorbs all the incident radiation.

The concept of a blackbody, that is a perfect absorber and emitter of radiant energy, comes from Kirchoff's Law of thermal radiation, which states that the emissivity (ε) of a body is equal to its absorptivity (α):

$$\alpha = \varepsilon \quad (2.2)$$

Using equation 2.2 into equation 2.1, and assuming a perfect blackbody ($\tau=\rho=0$), we have:

$$\varepsilon_{bb} = 1 \quad (2.3)$$

where the subscript bb indicates a blackbody. From this, the concept of emissivity for an object that is not a perfect blackbody can be written:

$$\varepsilon = \frac{\Phi_{obj}}{\Phi_{bb}} \quad (2.4)$$

where, Φ_{obj} and Φ_{bb} are the total radiant energy emitted by a real object and by a blackbody at the same temperature, respectively.

Planck's Law describes the energy radiated by a blackbody as a function of its temperature and of the wavelength of emission.

$$\Phi_{bb}(\lambda, T) = \frac{C_1}{\lambda^5 (\exp(C_2/\lambda T) - 1)} \quad (2.5)$$

with,

$$C_1 = 2\pi c^2 h \quad (2.6)$$

$$C_2 = \frac{ch}{k} \quad (2.7)$$

where, C_1 is the first constant of radiation, C_2 is the second constant of radiation, λ is the wavelength of the emission, T is the temperature of the blackbody, c is the speed of light in the medium, h is the Planck's constant ($\sim 6.626 \times 10^{-34} \text{ m}^2 \text{ kg s}^{-1}$) and k is the Boltzmann constant ($\sim 1.381 \times 10^{-23} \text{ m}^2 \text{ kg s}^{-2} \text{ K}^{-1}$).

Figure 2.2, below, shows the plot of Planck's Law for various temperature levels:

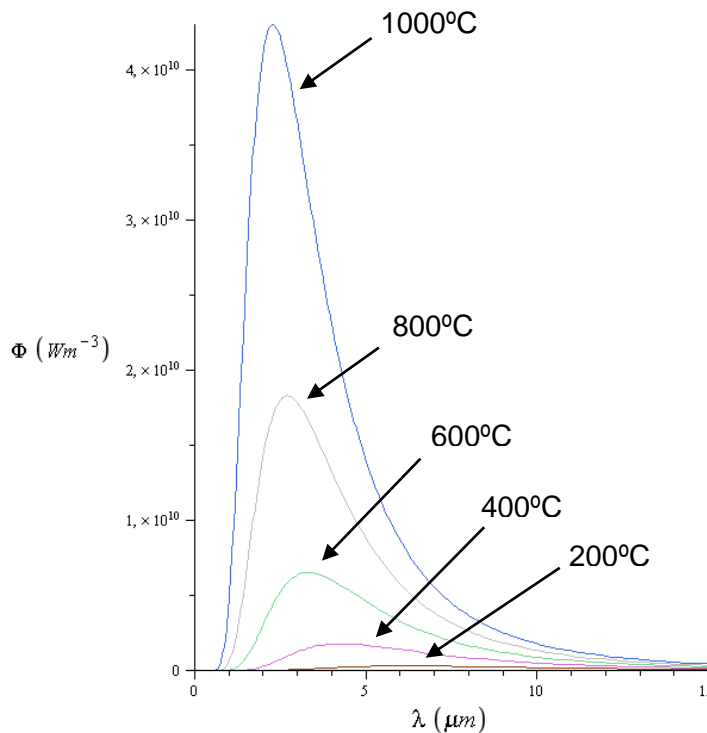


Figure 2.2: Plot of Planck's Law.

Integrating the Plank's law, the result describes the total energy radiated by a blackbody as a function of its temperature:

$$\Phi_{bb} = \int_{\lambda} \Phi_{bb}(\lambda, T) = BT^4 \quad (2.8)$$

where, B is the Stefan-Boltzmann constant ($5.670 \times 10^{-8} \text{ W m}^{-2} \text{ K}^{-4}$) and T is the blackbody's temperature.

Using equations 2.4 and 2.8 it is easy to determine the total energy emitted by an object:

$$\Phi_{obj} = \varepsilon BT^4 \quad (2.9)$$

where $0 < \varepsilon < 1$ is the object's emissivity.

In reality, emissivity is a function of the wavelength of emission $\varepsilon(\lambda)$. Because of that, equation 2.9 actually describes the total energy radiated by a theoretical object, called grey-body.

The definition of a grey-body is a body that emits radiation in constant proportion to the corresponding blackbody. For reasons still to be discussed, infrared thermography uses only small windows of wavelength to measure temperature, and because of that, the approximation of real life objects as grey-bodies is acceptable [2].

Between the surface which the temperature is being measured and the infrared sensor usually is the atmosphere. Earth's atmosphere itself interacts with radiation like any other object. It can absorb, transmit and reflect the energy. Because of that, the total radiation that reaches the sensor is the sum of three portions:

$$\Phi_{sensor} = \underbrace{\tau_{atm}}_{(1)} \Phi_{obj} + \underbrace{\rho_{obj} \tau_{atm}}_{(2)} \Phi_{amb} + \underbrace{\varepsilon_{atm}}_{(3)} \Phi_{atm} \quad (2.10)$$

where:

- (1) The energy radiated by the object Φ_{obj} after being attenuated by the atmosphere's transmittance τ_{atm} .
- (2) The energy radiated by the ambient Φ_{amb} after being reflected by the object ρ_{obj} and then attenuated by the atmosphere's transmittance τ_{atm} .
- (3) The energy radiated by the atmosphere itself.

Assuming that the object is opaque to infrared wavelength ($\tau_{obj}=0$) and that the atmosphere does not reflect radiation ($\rho_{atm}=0$), equation 2.10 is rewritten, by using the Total Radiation Law (Equation 2.1):

$$\Phi_{sensor} = \tau_{atm} \Phi_{obj} + (1 - \epsilon_{obj}) \tau_{atm} \Phi_{amb} + (1 - \tau_{atm}) \Phi_{atm} \quad (2.11)$$

(1) (2) (3)

The conclusions from equation 2.11 are that maximizing the atmosphere's transmittance and the object's emissivity are the key to amplifying the portion of the energy that reaches the sensor that is radiated by the object, while reducing the noise. In order to do that, infrared sensors use so-called "atmospheric windows", specific wavelength intervals that are almost not absorbed by Earth's atmosphere. Figure 2.3 shows the infrared atmospheric transmittance and the two typical "windows" used by commercial sensors (3-5 μ m and 8-14 μ m):

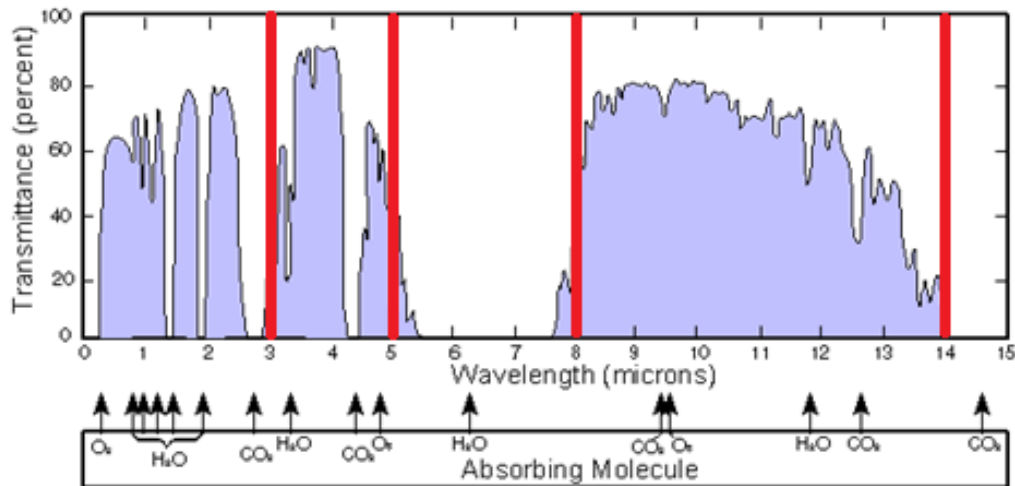


Figure 2.3: Atmosphere transmittance and atmospheric windows [2].

Table 2.1 shows the emissivity of typical material and paints that are typically used to maximize the surface's emissivity:

Aluminum	Polished	0.04-0.05
	Oxidized	0.10-0.31
	Anodized	0.55-0.72
Steel	Polished	0.07-0.09
	Oxidized	0.79
Paint	Matt Black lacquer	0.97
	White enamel	0.92
	oil	0.89-0.97
PVC		0.91-0.93
Insulating Tape	Black	0.97

Table 2.1: Emissivity of some materials and paints.

2.2.2

Infrared Sensors

Infrared sensors can be divided into two categories: Cooled detectors and Uncooled detectors. Both have advantages and disadvantages that are discussed below [2]:

Cooled detectors

Also known as quantum or photon detectors, this kind of infrared sensor uses the same principle of most common digital cameras, the only difference being the constituent materials. Basically, when a photon of a specific wavelength range hits the semiconductor it is absorbed, causing an electron of an atom to jump to a higher energy state. What is then measured is the change in conductivity caused by this phenomenon.

Because of how they work, and the high sensitivity of the process, the quantum detectors must be cooled to very low temperatures, typically around the 60-100K range. This need causes these sensors to be very expensive not only to produce but to operate as well, since the cooling process is very energy-intensive and time-consuming.

Although much more expensive, the photon detectors have higher sensitivity and accuracy, because of that, they can achieve much higher resolution cameras. Another advantage is the possibility of using both atmospheric windows (3-5 and 8-14 μm), depending on the constitution and construction of the sensor.

Until recently, photon detectors were the only viable choice for practical thermography applications. Reference [3] presents a comprehensive guide to photon detectors.

Uncooled detectors

This kind of sensor works based on a simpler principle. It absorbs the infrared radiation causing its temperature to rise, this rise in temperature then causes a change in an electrical property, such as resistance, which is then read by a proper circuit. Because of how it works, it is sometimes called thermal detector.

Exactly because it depends on a change in its temperature, the thermal detector does not need to be cooled down. Because of that, its cost is an order of magnitude lower than the cooled ones, both to produce and to operate.

The main disadvantages of the uncooled detectors are the lower sensitivity and the restriction to the higher wavelength atmospheric window (8-14 μm). It was not until recent advancements that these sensors became viable for practical thermography.

The American astronomer Samuel Pierpont Langley discovered, in 1878, the main type of thermal detector, the bolometer [4]. By the late 70's, microbolometers were developed by Honeywell for the US Department of Defense, being declassified in 1992 when a series of manufacturers started producing and developing cameras with microbolometer arrays. From then on, thermal detectors would start to see more use in scientific applications [5].

Figure 2.4 shows a scheme of a microbolometer making it easier to understand how it works.

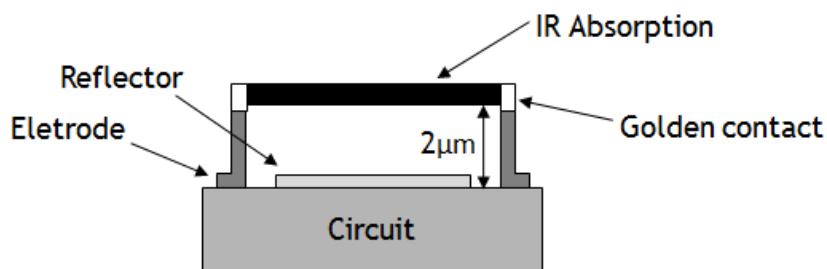


Figure 2.4: Cross section view of a microbolometer.

Because of the principle on which the bolometer is based, it has an intrinsic disadvantage. When compared to cooled detectors, they present a rather slow thermal time constant, proportional to the time required for the mass of the absorber to reach a stable temperature. This time is reported to be of the order of 40-50ms, which results in a maximum frame rate of about 25Hz. For applications where the temperature transient is much faster than this, quantum detectors must be used to read accurate temperature values [6].

The camera used on most of this work is a FLIR A655sc bought from FLIR Systems in early 2015. It uses a focal plane array (FPA) of 640 by 480 pixels of 17 microns each, data acquiring frequency of 50Hz on full frame configuration up to 200Hz for a quarter frame and spectral range from 7.5 to 14 μm . Figure 2.5 shows the camera.



Figure 2.5: Camera FLIR A655sc, used in most of this work.

It can switch between two different temperature ranges ($-40 - 150^{\circ}\text{C}$ and $100 - 650^{\circ}\text{C}$) with a $<30\text{mK}$ sensitivity in both of them.

2.3

Active Thermography

Active thermography consists of measuring the effects of a heat source on an object. Usually measuring differences on the rates of heating or decaying, it can be used to detect features that do not generate heat by themselves. One use, outside the engineering research field, are the active night-vision goggles, that combine infrared illuminators with detectors and make it possible to see a monochromatic view of a low light ambient.

In mechanical engineering, the most common use of active thermography is the detection of defects in structures. Ibarra-Castanedo [7], presents a great discussion about this use of thermography, emphasizing the use of pulsed thermography. This technique, as well as pulsed-phase and lock-in thermography, have been used many times to locate defects and predict their sizes and depths [7]-[11].

Appendix 1 describes a simple test on defect location using pulsed thermography that was developed during the experimental phase of the present work.

2.4

Passive Thermography and Thermoelastic Stress Analysis (TSA)

While active thermography requires a heat source, passive thermography, as the name suggests, does not. It relies on temperature variations already existent in the analyzed object, usually caused by heat generation within it.

Passive thermography has many applications in various fields of study. Some examples are: Passive night-vision, for defense and surveillance, for electronic components monitoring and for medical examinations [12]. A very recent application that was employed in many airports worldwide was to examine passengers for fever during the 2009 swine flu (H1N1 Influenza) pandemic.

In the experimental mechanics field, maybe the most used passive thermography technique, and main focus of the present work, is the so-called Thermoelastic Stress Analysis (TSA) technique.

2.4.1

Physics of TSA, the Thermoelastic Effect

Towards the end of the 19th century, William Thomson (Lord Kelvin) documented the thermoelastic effect for the first time [13].

He discovered that when a solid materials is subjected to tensile stress its temperature rises slightly and when a compressive stress is applied, the temperature drops in the same proportion.

In reality, the change in temperature caused by the thermoelastic effect is proportional to the sum of the principal stresses acting in the body. The following equation describes this phenomenon:

$$\Delta T = \frac{-\alpha T_0}{\rho c_p} (\Delta \sigma_1 + \Delta \sigma_2) \quad (2.12)$$

where, α is the linear thermal expansion coefficient, T_0 is a reference temperature, ρ is the density of the material, c_p is the specific heat at constant pressure and σ_1 and σ_2 are the principal stresses.

A simplified deduction of equation 2.12 is shown herein, while the complete thermodynamics arguments for it can be found in the literature [14].

A small change in temperature in a body depends on its stress state, the strains that are being applied and the heat exchange profile (conduction) within the solid [15].

$$\dot{T} = \frac{T_0}{\rho C_\epsilon} \frac{\partial \sigma_{ij}}{\partial T} \dot{\epsilon}_{ij} + \frac{\dot{Q}}{\rho C_\epsilon} \quad (2.13)$$

where, T_0 is a reference temperature, ρ is the density of the material, C_ϵ is the specific heat at constant strain, σ_{ij} is the stress tensor, $\dot{\epsilon}_{ij}$ is the rate of change in the strain tensor and \dot{Q} is the rate of heat production per unit volume.

In TSA, the standard approach is to apply a cyclic load to the specimen at a frequency in which no heat conduction takes place, making it possible to neglect the second term of equation 2.13. Because of that, it is safe to say that the sensor will only be measuring the surface temperature variation, and the stress-strain-temperature relationship for an isotropic material in plane stress conditions have to be used.

$$\sigma_{ij} = 2\mu\varepsilon_{ij} + (\lambda\varepsilon_{kk} - \beta\delta T)\delta_{ij} \quad (2.14)$$

where δ_{ij} is the Kronecker delta and

$$\mu = \frac{E}{2(1+\nu)} \quad \lambda = \frac{\nu E}{(1+\nu)(1-2\nu)} \quad \beta = (3\lambda + 2\mu)\alpha \quad (2.15)$$

where, ν is the Poisson's coefficient, E is the Young's modulus and α is the linear thermal expansion coefficient.

Deriving equation 2.14 with respect to T , and assuming that the linear constants do not vary with temperature:

$$\frac{\partial \sigma_{ij}}{\partial T} = -\beta\delta_{ij} \quad (2.16)$$

Then, substituting equation 2.16 into equation 2.13:

$$\dot{T} = -\frac{T_0\beta}{\rho C_\varepsilon} \dot{\varepsilon}_{kk} \quad (2.17)$$

Using equations 2.14 and 2.15:

$$\dot{T} = -\alpha \left[\frac{T_0}{\rho C_\varepsilon} + \frac{1-2\nu}{3\alpha^2 E} \right] \dot{\sigma}_{kk} \quad (2.18)$$

Knowing that C_ε can be written as a function of C_p :

$$C_\varepsilon = C_p - \frac{3E\alpha T_0}{\rho(1-2\nu)} \quad (2.19)$$

Plugging equation 2.19 into equation 2.18 and integrating it, the result is equation 2.12.

2.4.2

Calibration and Practical Application of TSA

As discussed before, for the application of TSA, infrared cameras, governed by equation 2.9, are used. Deriving equation 2.9:

$$\Delta\Phi_{obj} = 4\varepsilon BT^3 \Delta T \quad (2.20)$$

Plugging equation 2.19 into equation 2.20 and rearranging it results in:

$$\Delta\sigma_1 + \Delta\sigma_2 = -\frac{\Delta\Phi_{obj}}{4\varepsilon BT^3} \frac{\rho c_p}{\alpha T_o} \quad (2.21)$$

Considering the response S from the detector as being proportional to $\Delta\Phi_{obj}$ by a gain Z (property of the sensor):

$$S = \frac{-4Z\varepsilon BT^3 \alpha T_o}{\rho c_p} (\Delta\sigma_1 + \Delta\sigma_2) \quad (2.22)$$

Finally, in practical uses of the TSA technique, measuring all the material and sensor properties is not needed. The typical application uses a simple calibration process that consists of using an object with a known stress state ($\Delta\sigma_1 + \Delta\sigma_2$), like a simple tensile specimen, to determine a coefficient A that is used as described [16]:

$$A S = (\Delta\sigma_1 + \Delta\sigma_2) \quad (2.23)$$

2.4.3

Data Acquisition and Interpretation

As stated before, typical TSA applications require a cyclic loading, and by combining the thermographic signal and the load signal in what is called a lock-in process, the magnitude and signal of the first invariant of the stress tensor can be determined [15]. Figure 2.6 shows, schematically, a typical TSA test.

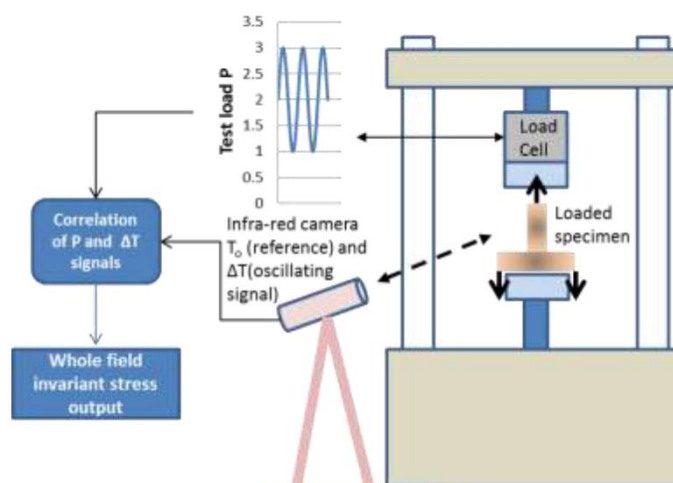


Figure 2.6: Typical TSA test procedure, adapted from [17].

From the infrared camera signal and through equation 2.23, the magnitude of the stress invariant is determined. By correlating both signals, the phase map is

determined, from which the signal of the invariant can be determined. Figure 2.7 shows the maps for both those results from a TSA test of a notched aluminum plate.

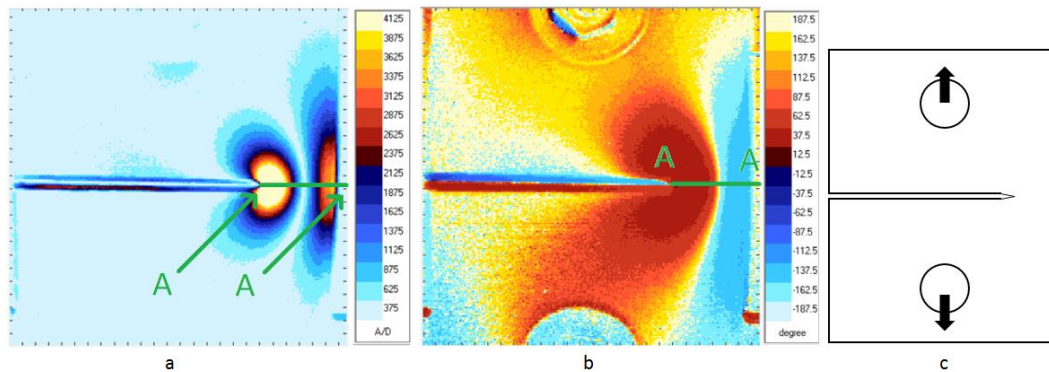


Figure 2.7: a) Magnitude and b) Phase maps of a TSA test of a c) Notched aluminum plate, [17].

From Figure 2.7a, it is possible to see the expected profile for the magnitude of stresses, since in this case only σ_1 is not zero at the boundaries (points A). Near the notch, the stress concentration shows as a white color, representing a higher magnitude for the invariant. The same happens at the opposite end of the specimen, which is under a high stress state. While the notch sees a tensile stress, the opposite face sees a compressive one, and vice versa.

Figure 2.7b clearly shows this difference in phase between these two regions. It was obtained by setting the points of zero stress as a reference and then comparing each point magnitude signal to the load signal. The lock-in process, which determines the phase map, is necessary to interpret TSA results.

2.4.4

'DeltaTherm 2' Software Peculiarities

'DeltaTherm 2' is a commercial TSA software developed by Stress Photonics Inc. It was used in the entirety of this work, unless otherwise specified.

The main advantage of this software, when compared to the typical TSA approach described above, is the bypass of the load signal requirement. DeltaTherm 2 allows the user to select a reference region on the sensor image, and uses the phase information from this region as the load signal [18]. By doing this, the lock-in process becomes automatic and setting up a TSA test becomes an almost trivial task.

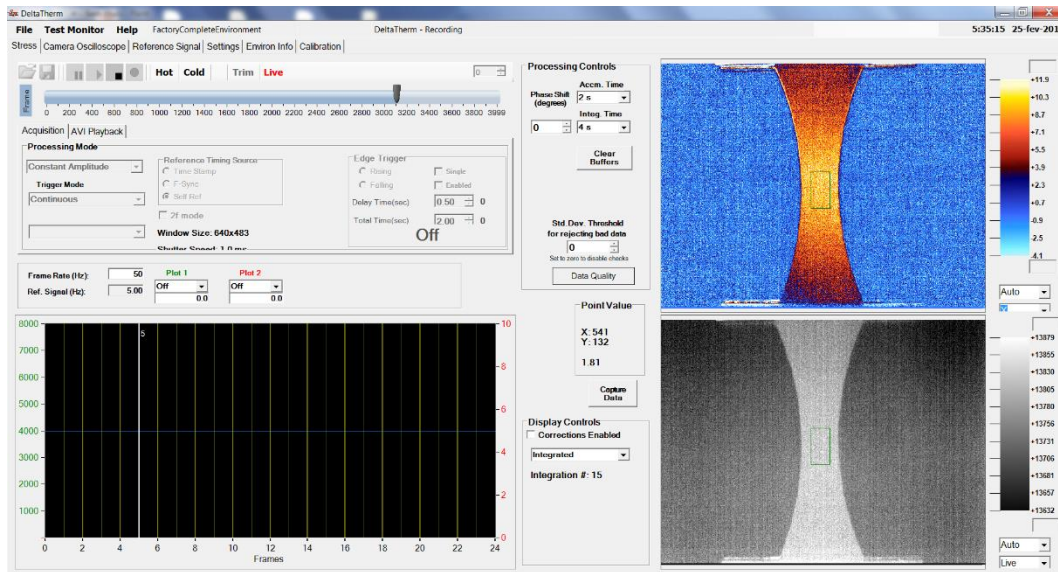


Figure 2.8: Screenshot of the DeltaTherm 2 interface.

2.4.5

Applications of TSA – Bibliographical Review

The TSA technique is a very powerful tool for experimental mechanics in many fields of study.

It has been frequently used to measure the stress fields in complicated geometries and around discontinuities, coupled with numerical methods and stress functions to separate the principal stresses [19]-[22].

The combination of TSA with other experimental techniques in order to improve some of its weak aspects is another research area. Like the separation of stresses (combined with photoelasticity) [23] and [24] and accounting for specimen motion (combined with Digital Image Correlation) [25] and [26].

The effects of mean stress in the thermoelastic coefficient was used to develop a method to measure residual stresses [27]-[30].

In fatigue studies, TSA has been used to assess damage initiation and evolution on composites [31]-[33]. It was also successfully used to measure stress intensity factors (SIFs) of fatigue cracks through interpolation of the stress field around the crack tip and J-integral approach [34]-[41]. Crack closure [40] and the effect of overloads [41] were also studied and satisfactory fatigue life [42] and crack path [43] predictions were made.

Appendix 2 describes a simple experiment that monitored cracks on welded joints. It shows how easily the cracks can be located and their paths predicted and monitored.

3

Brief Fatigue and Polycarbonate (PC) Review

3.1

Review of Basic Fatigue Concepts

The study of fatigue is usually divided in two main fields. Crack initiation and crack growth. Basic concepts of both fields, which are used throughout this work, are reviewed in this section.

3.1.1

Fatigue Crack Initiation and the Wohler curve

The most used approach for fatigue dimensioning is the so-called Wöhler method (or SN method). Simply put, this approach uses the correlation between the amplitude of the cyclic stresses acting at a critical point and the number of loading cycles necessary for a fatigue crack to initiate. The SN curve (Wöhler curve) is the plot of this correlation, and can be used to predict the number of cycles a specimen at a given alternate stress level can sustain before failing. The most common equation used to adjust data in the Wöhler curve is the parabolic relationship that linearizes the data in a log-log plot [44].

$$NS^m = C \quad (3.1)$$

where N is the number of cycles until failure, S is the stress amplitude ($S=\sigma_a=\Delta\sigma/2$), m and C are material constants known as fatigue exponent and fatigue coefficient, respectively. Figure 3.1 shows a typical SN curve, using Juvinall's estimations for a carbon steel with ultimate strength of 1000MPa in rotating bending test [44].

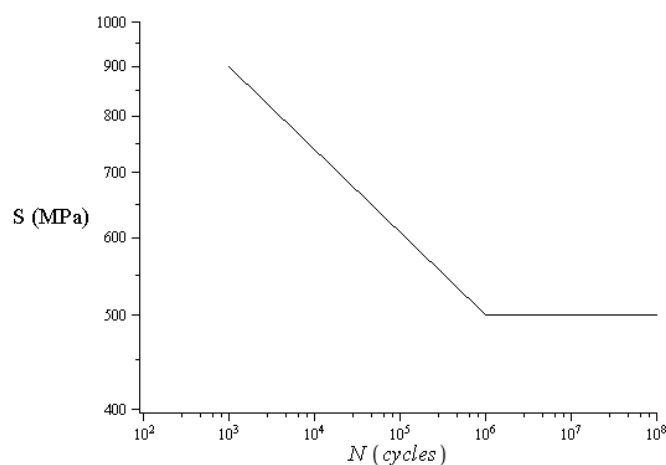


Figure 3.1: Typical SN curve, using Juvinall's estimations for steel ($S_R=1000\text{MPa}$).

In practice, although very useful, approximations like the ones made by Juvinall [44] can produce non-conservative predictions. Because of that, measured SN curves are very important, as they are capable of characterizing the fatigue behavior of a specific material.

Each point of the curve represents one specimen that was cyclic loaded until failure, and very high number of cycles are needed for the lower stress points. In addition, because fatigue is a naturally statistical problem, the data usually presents high dispersion, especially for the lower stress points. It is easy to see why measuring SN curves is very time consuming. There are some proposed methods to accelerate this process. One of these, called the Risitano method, which uses thermography to determine the Wöhler curve, is used to measure the SN curve of polycarbonate further on.

From what has been said about the SN method, it is clear that stress analysis plays a huge role in this approach, since it is very important to know the actual stresses acting at the critical point of a component in order to determine its fatigue life even when having access to a measured SN curve. Two aspects of stress analysis, that are going to be used in later chapters, are discussed next.

3.1.2

Stress Concentration

Geometrical discontinuities usually cause a phenomenon called stress concentration. The concept of force lines is very useful in understanding why that happens. Figure 3.2 illustrates this concept, showing through which path the force applied to the plate travels.

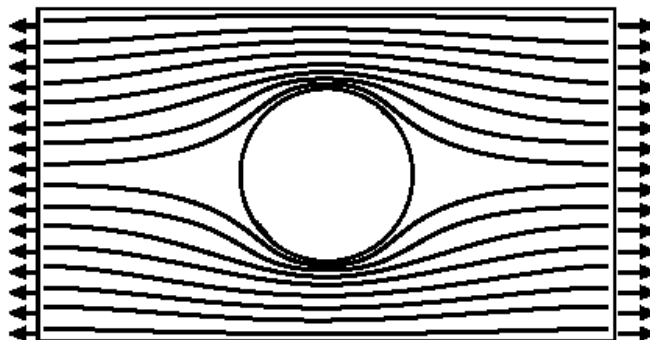


Figure 3.2: Concept of force lines.

From Figure 3.2 it is clear how the hole forces the lines to deviate and concentrate. The problem of the infinite plate with a circular hole was the first stress concentration problem solved analytically by Kirsch in 1898 [44] when calculating

the circumferential stresses around the hole boundary. He arrived at the following expression.

$$\sigma_{\theta}(r, \theta) = \frac{\sigma_n}{2} \left[\left(1 + \frac{R^2}{r^2} \right) - \left(1 + \frac{3R^4}{r^4} \right) \cos 2\theta \right] \quad (3.2)$$

where, $\sigma_{\theta}(r, \theta)$ is the circumferential stress as a function of r (the distance from the center of the hole) and θ (the angle with the direction of the stress applied to the plate), σ_n is the nominal stress applied to the plate and R is the radius of the hole.

When $r=R$ and $\theta=\pm\pi/2$, the circumferential stress assumes its maximum value. $\sigma_{max}= 3\sigma_n$. The concept of stress concentration factor (K_t) is defined as.

$$K_t = \frac{\sigma_{max}}{\sigma_n} = 3 \text{ (for Kirsch's problem)} \quad (3.3)$$

The implications of this phenomenon are that even if the hole will not change the nominal stresses applied to the plate, the real stress acting at the critical point of the component is 3 times higher. Stress concentration regions, the so-called hot spots, are where fatigue cracks initiate and cause fatigue failure.

Thermoelasticity is a very powerful tool in measuring stress concentrations, since it provides a full-field stress map of the specimen surface, and because stress concentrations usually happens at free surfaces, one of the principal stresses is always zero, making the TSA data a direct measurement of the maximum circumferential stress. TSA, in conjunction with photoelasticity and Digital Image Correlation techniques, was used to measure stress concentration factors of aluminum u-notch and polycarbonate keyhole specimens by the author in [45] and [46].

3.1.3

The Mean Stress Effect

Generally, two driving forces, maximum stress and stress range, govern fatigue effects. The usual way to consider both when predicting the fatigue life of a component is to use a constant life diagram to determine the equivalent completely alternating stress, that would result in the same life as the real stress acting on the specimen [44].

The most used model of a constant life diagram is the Goodman's rule. It linearly correlates the alternating stress (σ_a) and the mean stress (σ_m) with the following equation.

$$\frac{\sigma_a}{S_F(N)} + \frac{\sigma_m}{S_R} = 1 \quad (3.4)$$

where $S_F(N)$ is the fatigue strength for a specific number of cycles and S_R is the ultimate tensile strength.

If S_F is taken at a number of cycles high enough to be considered infinite life, S_F will be the fatigue limit of the material, and the Goodman curve plotted in Figure 3.3 determines the points which will eventually fail (above the curve) and the point which will not (below the curve).

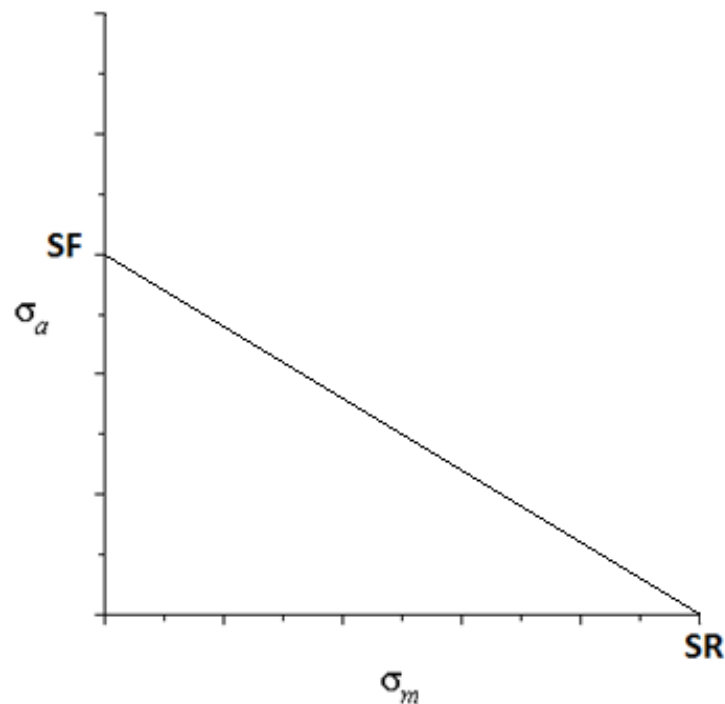


Figure 3.3: Schematic Goodman's curve.

Rearranging Equation 3.5 the equivalent alternating stress (σ_{a-eq}) is determined as:

$$\sigma_{a-eq} = \frac{\sigma_a}{1 - \frac{\sigma_m}{S_R}} \quad (3.5)$$

This rule is a complementation to the Wöhler curve. Since the SN approach usually reports data using completely alternating stresses, the Goodman's relationship is needed in order to compare real problems to it [44].

Similar rules exist in order to accomplish the same task, some of them are the Gerber's rule, Soderberg's rule and the Elliptical rule. Nonetheless, it has been

shown that the Goodman formula describes the effect of mean stress in polymers quite well, hence why it is used here [47].

3.1.4

Fatigue Crack Growth and Linear Elastic Fracture Mechanics

Basic Linear Elastic Fracture Mechanics

After a crack has initiated at the critical point of a component under cyclic loading, it will grow until it reaches a critical point resulting in terminal failure. Fatigue crack growth is a wide field of study, but here only a basic review is presented using the approach of linear elastic fracture mechanics.

The difficulty of determining fatigue life after a crack has initiated arises from the predictions of the Inglis solution to the stress concentration factor of an elliptical hole on an infinite plate:

$$K_T = 1 + 2 \sqrt{\frac{a}{\rho}} \quad (3.6)$$

where a is half the major axis of the ellipse and ρ is the radius of its tip.

A crack is then modeled as an elliptical hole of radius zero ($\rho \rightarrow 0$), and the stress concentration factor goes to infinity ($K_T \rightarrow \infty$). Then, the prediction is that the stress at the tip of a crack is always singular and infinite. The singularity of stress is not useful in practice, because it cannot be compared to a resistance in order to determine if a component will or will not fail.

That being said, real life components do resist stress even when cracked, so a model to describe their behavior was created. Williams and Irwin developed the linear elastic fracture mechanics concepts simultaneously in 1957 [48], although they took different paths (chose different stress functions), they arrived at the same result.

The idea behind linear elastic fracture mechanics is to use the stress field around a crack tip in order to describe the behavior of the cracked body. In order to do that, Williams used a stress function based on infinite series of sines and cosines [48].

$$\varphi(r, \theta) = r^2 f(r, \theta) + g(r, \theta) \quad (3.7)$$

with

$$f(r, \theta) = \sum_n r^n [A_n \cos(n\theta) + C_n \sin(n\theta)] \quad (3.8)$$

$$g(r, \theta) = \sum_n r^{n+2} \{B_n \cos[(n+2)\theta] + D_n \sin[(n+2)\theta]\}$$

where φ is the stress function, r and θ are the coordinates of the polar system with origin at the crack tip, A_n , B_n , C_n and D_n are the coefficients of the function that adjusts the stress field.

There are three possible crack-opening modes, all illustrated by Figure 3.4. This work will focus only on mode I crack opening, since it is usually the most critical and important one.

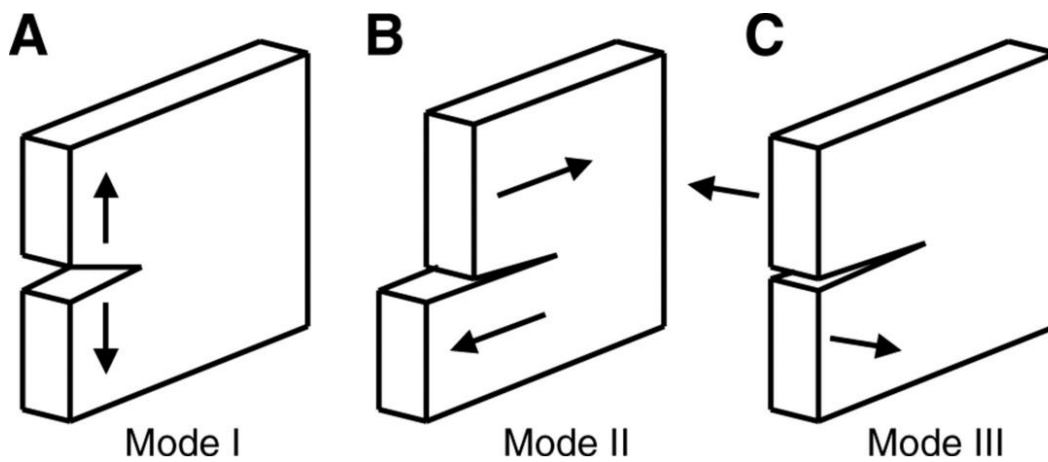


Figure 3.4: Crack opening modes.

For mode I, the stresses are symmetrical with respect to the crack plane. Thus, the sine terms are all zero. The stress function becomes:

$$\varphi I(r, \theta) = \sum_n r^{n+2} \{A_n \cos(n\theta) + B_n \cos[(n+2)\theta]\} \quad (3.9)$$

and the stress components can be determined:

$$\sigma_\theta = \frac{\partial^2 \varphi}{\partial r^2}$$

$$\sigma_r = \frac{1}{r} \frac{\partial \varphi}{\partial r} + \frac{1}{r^2} \frac{\partial^2 \varphi}{\partial \theta^2} \quad (3.10)$$

$$\sigma_{r\theta} = -\frac{\partial}{\partial r} \left(\frac{1}{r} \frac{\partial \varphi}{\partial \theta} \right)$$

Then, by applying the boundary conditions of the free surfaces of the crack ($\sigma_{\theta}(\pm\pi)=\sigma_{r\theta}(\pm\pi)=0$), the resulting stress field (near field around a crack tip), in Cartesian coordinates, comes to be:

$$\begin{aligned}\sigma_x &= \frac{KI}{\sqrt{2\pi r}} \cos\left(\frac{\theta}{2}\right) \left[1 - \sin\left(\frac{\theta}{2}\right) \sin\left(\frac{3\theta}{2}\right)\right] \\ \sigma_y &= \frac{KI}{\sqrt{2\pi r}} \cos\left(\frac{\theta}{2}\right) \left[1 + \sin\left(\frac{\theta}{2}\right) \sin\left(\frac{3\theta}{2}\right)\right] \\ \sigma_{xy} &= \frac{KI}{\sqrt{2\pi r}} \cos\left(\frac{\theta}{2}\right) \sin\left(\frac{\theta}{2}\right) \cos\left(\frac{3\theta}{2}\right)\end{aligned}\quad (3.11)$$

where the K_I term is the stress intensity factor for mode I. In order to describe the stress field farther from the crack tip, more terms are required, as seen later on.

Irwin, on the other hand, used a complex Westergaard stress function to describe the stress field around the crack tip. The stress function is:

$$\varphi(z) = Re(\bar{Z}) + y Im(\bar{Z}) \quad Z = \frac{d\bar{Z}}{dz} \quad \bar{Z} = \frac{d\bar{Z}}{dz} \quad (3.12)$$

where Z is an analytical complex function $Z(z) = f(x,y) + ig(x,y)$, z is the complex coordinate $z = x + iy$, and x and y are the Cartesian coordinates.

The near stress field is then defined, using equation 3.10:

$$\begin{aligned}\sigma_x &= ReZ - yImZ' \\ \sigma_y &= ReZ + yZ' \\ \sigma_{xy} &= -yReZ'\end{aligned}\quad (3.13)$$

For the mode one crack in an infinite plate the following complex function Z satisfies all boundary conditions and, if inserted in equation 3.13, yields the same result of equation 3.11.

$$Z = \frac{z\sigma}{\sqrt{(z^2 - a^2)}} \quad (3.14)$$

where a is half the size of the crack and σ is the nominal stress.

With the Westergaard approach, the problem is to find the appropriate complex function, which satisfies the boundary conditions and yields the correct results. This approach is used later when measuring stress intensity factors through TSA. Instead of a complex function, a complex series expansion was used to fit the data from TSA.

Application to Fatigue Crack Growth

In 1961, Paris, Gomez and Anderson reported their findings that the stress intensity factor range (ΔK) controlled the fatigue crack growth rate (da/dN) [48]. The so-called da/dN vs ΔK curve, depicted in Figure 3.5, is a plot of the crack growth rate versus the stress intensity factor, and it usually assumes an S shape.

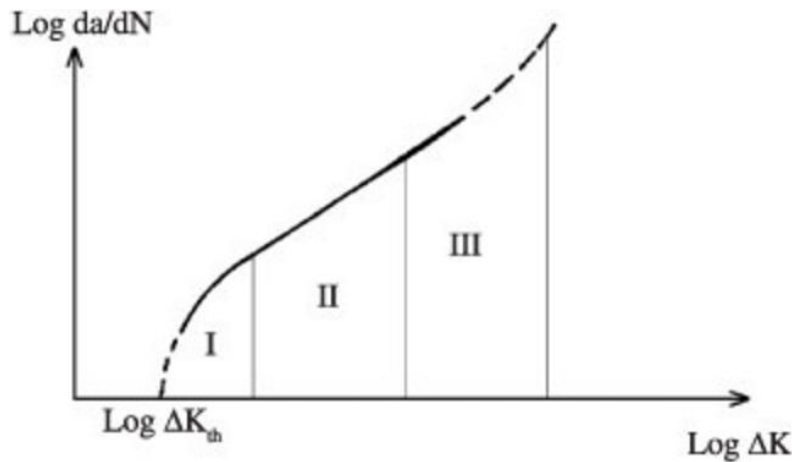


Figure 3.5: Schematic da/dN curve.

The three phases shown in Figure 3.5 can be explained by the micro-mechanisms that govern the fatigue crack growth.

The first phase, characterized by discontinuous crack growth is very dependent on mean stress, crack opening load and the material properties. The lower limit of ΔK (ΔK_{th}), the threshold below which there is no crack growth, is a property that depends on the stress ratio $R = \sigma_{min} / \sigma_{max}$.

The second phase, and focus of this and most other works on fatigue crack growth, is the phase where the crack spends most of its life. This phase is most often described by the famous Paris' law, which is a power law that fits the data points as a line in a log-log plot:

$$\frac{da}{dN} = \alpha(\Delta K)^m \quad (3.15)$$

Many other models exist, that consider multiple effects, such as the effect of R , of the crack closure and even sequence effects that can predict accelerations and retardations on crack growth [48].

The third phase, is the fastest phase, in which the crack growth rate is affected by fracture parameters such as the specimen thickness and the mean load. The highest value of stress intensity factor that can be tolerated by the crack is known as the fracture toughness K_C and is a function of the specimen thickness,

reaching its lowest value, known as K_{Ic} a material property, when the specimen is thick enough so that the stress state approximates the plane-strain condition.

The Paris law will be used in later chapters when the fatigue crack growth rate of cracked polycarbonate specimens will be measured via TSA. The hybrid thermographic technique used is capable of single handedly and automatically measure the data points for the da/dN vs ΔK curve.

3.2

Polycarbonate Properties

Polycarbonates (PCs) are polymers containing carbonate groups (-O-(C=O)-O-). They are usually very well balanced materials having relatively high temperature resistance, high ductility and high mechanical and impact strengths. Because of that, it is usually considered an engineering plastic and has a multitude of noble applications. It is used in the construction industry as transparent roofs and dome lights. The electronics industry uses it as a high temperature resistant electrical insulator. In the automotive and aircraft industries PC is laminated to make bullet-proof "glass", and is used from car headlights all the way to F-22 cockpit canopies.

As an engineering plastic, PC is often used in relatively high stress applications, couple that with the ease of manufacturing complicated geometries with high stress concentration factors. Then, considering that cyclic loading is bound to happen, in most of these applications, studying the fatigue properties of such a material becomes of utmost importance.

Polycarbonate is a thermoplastic that, as stated before, has very well balanced properties. Table 3.1 shows a list of some of these properties at room temperature [49] and [50]. Other properties are presented in Appendix 3.

Property	Value	Unit
Density	1150	kg/m ³
Young's Modulus	2300	MPa
Poisson's Coefficient	0.39	
Yield Strength	65	MPa
Nominal Tensile Stress at Rupture	60	MPa
Fracture Toughness (K_{Ic})	3	MPa m ^{1/2}
Glass Transition Temperature	420	K
Melting Temperature	573	K
Infrared Emissivity	0.9	

Table 3.1: Average values of some polycarbonate properties.

Polycarbonate is a thermoplastic engineering polymer and can sustain high amounts of plastic strain before cracking or breaking. Because of that, sometimes, it can be formed at room temperature, making these manufacturing processes much easier and cheaper.

3.2.1

Polycarbonate in Infrared Thermography

As seen in Table 3.1, polycarbonate has a high infrared emissivity, making it a good choice for infrared applications. It is almost opaque to infrared radiation, absorbing and emitting most of it. Because of that, it does not need a black painting, as most metallic objects do, in order to be analyzed through thermography.

Not only it is opaque to the infrared spectrum, it is a very good transmitter in the visible spectrum. That makes polycarbonate an interesting choice for combining thermoelasticity and photoelasticity [24].

3.2.2

Polycarbonate in Fatigue Studies

Fatigue Crack Growth

As stated before, it is very important to study the fatigue behavior of polycarbonate. Many studies have been conducted, but the field is still considered a complex one.

Hertzberg *et al.* [51] conducted fatigue crack propagation experiments in many different polymeric materials. Their findings for polycarbonate established that the use of classical fracture mechanics concepts, such as the stress intensity factor (SIF) and the Paris Law, was appropriate. Not only that, they investigated the effect of test frequency, finding that higher frequencies resulted in higher crack growth rates (da/dN) for the same SIF range (ΔK).

Gerberich *et al.* [52] corroborated by Hertzberg *et al.* [53], tested the effects of temperature in crack growth for polycarbonate specimens. Again, confirming the linear relationship between $\text{Log}(\Delta K)$ and $\text{Log}(da/dN)$ and the validity of fracture mechanics concepts. Their results showed a strange behavior. The crack propagation velocities for equal ΔK levels seemed to have a shifting point at around -50°C , which would be the point of minimum toughness. Figure 3.6 shows their results.

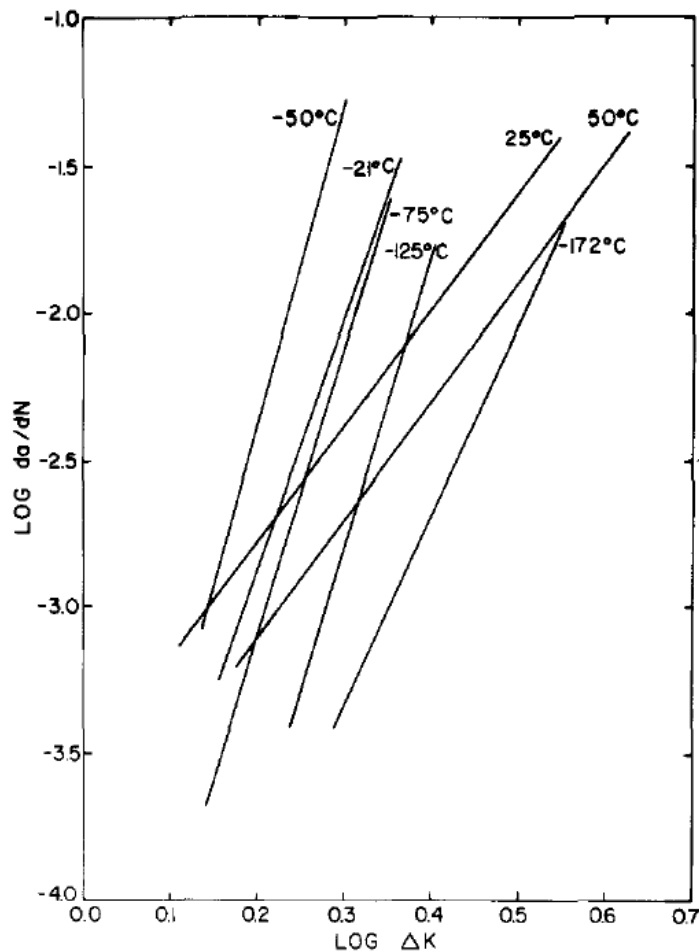


Figure 3.6: Paris law curves showing temperature effect, adapted from [52].

They explained that change in crack growth ratio by a measurable change in fracture toughness (K_{Ic}), which, in return, was explained by secondary energy losses due to the rising temperature at the crack tip.

Figure 3.6 also shows a dependency of the slope of the curve on the test temperature. The reported coefficients of the Paris curve, Equation 3.1, are listed in Table 3.2.

Temperature (°C)	α (mm/cycle)	m	Temperature (°C)	α (mm/cycle)	m
-172	5.2E-06	6.5	-21	2.5E-05	8.6
-150	1.9E-06	8.4	0	9.4E-06	7.5
-125	1.6E-06	10	25	2.7E-04	3.9
-100	1.8E-05	7.2	40	2.4E-04	3.2
-75	8.8E-06	9.8	50	1.1E-04	4.1
-50	2.9E-05	10.7	100	1.4E-03	1.2

Table 3.2: Reported values of Paris coefficients at various temperatures, adapted from [52].

Ward *et al.* [54] studied the effect of specimen thickness in crack growth rates of polycarbonate specimens. They tested 3, 6 and 9mm thick specimens and

reported a decrease in fatigue strength with an increase in thickness. Figure 3.7 shows the reported da/dN vs ΔK curves.

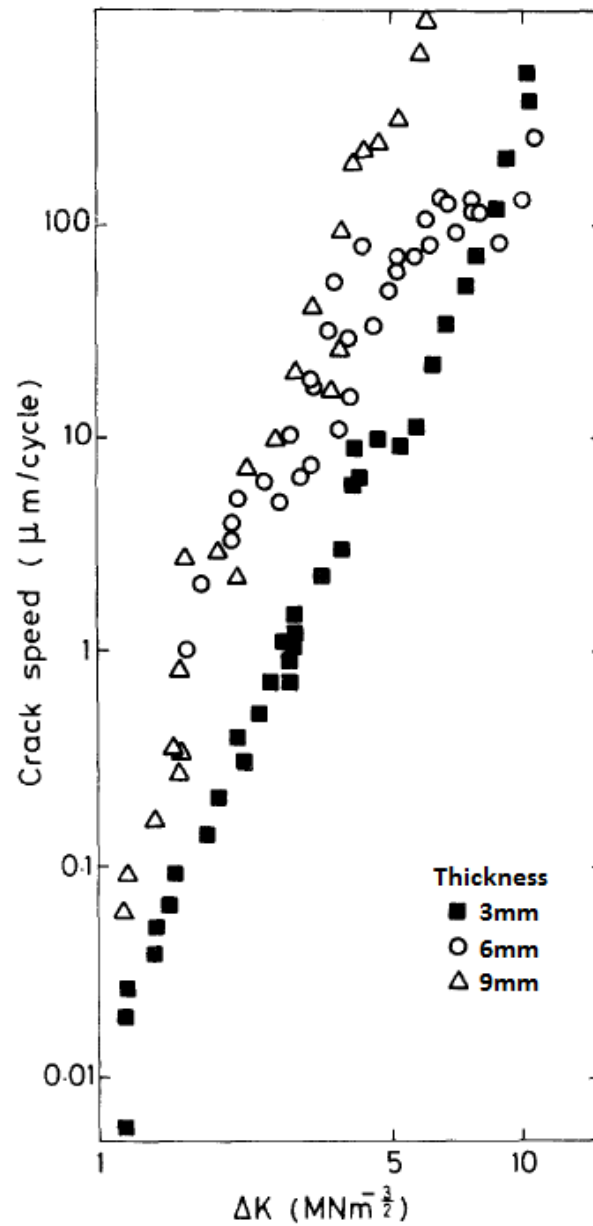


Figure 3.7: da/dN vs ΔK curves for three different thicknesses, adapted from [54].

Pruitt *et al.* [55] also explored the effects of specimen thickness, as well as the effects of stress ratio ($R = \sigma_{\min}/\sigma_{\max}$) on the fatigue behavior of polycarbonate. They corroborated the results from [54] of a decrease in toughness with an increase in thickness.

They also reported a counterintuitive result about the stress ratio effect. Their findings show an increase in toughness with an increase in stress ratio. Table 3.3 shows the reported values for the Paris coefficients.

R	Thickness (mm)	Frequency (Hz)	α	m
0.1	2.2	5 (Sine)	5.55E-04	2.87
0.2	2.2	5 (Sine)	5.60E-04	2.88
0.3	2.2	5 (Sine)	7.00E-04	5.20
0.4	2.2	5 (Sine)	2.80E-04	3.60
0.5	2.2	5 (Sine)	4.00E-05	2.70
0.1	2.2	3 (Square)	4.40E-05	2.80
0.1	5.6	3 (Square)	1.70E-04	2.60

Table 3.3: Paris coefficients reported for different stress ratios and thicknesses, adapted from [55].

Both [54] and [55] attribute their findings to the competing yielding mechanisms of polycarbonate, shear banding and crazing.

In thicker specimens, near plane-strain state, the crazing mechanism is dominant, while in thinner, near plane-stress state, the shear banding mechanisms prevails. They supposed that the shear bands could shield the crack tip from the full stress intensity, and by doing that increase the fatigue strength. The same is valid for the effect of R, the higher stress ratios presented crazing dominant yielding, while shear banding prevailed in the lower stress ratios.

Moet *et al.* [56] further investigated the effect of yielding mechanisms on fatigue crack growth in polycarbonate. The authors used Crack Layer theory (CL) to successfully predict crack growth rates. Patterson *et al.* [57] used this known effect to validate their proposed new model of near crack tip stress fields. The predicted values for ΔK coincided with values obtained using advanced optic and photoelastic experimental techniques.

Fatigue Crack Initiation

Chudnovsky *et al.* [58] and [59] studied the effects of the yielding micro-mechanisms on the fatigue crack initiation in polycarbonate specimens. The reported result, Figure 3.8, is a map of fatigue-crack initiation mechanism with respect to stress level and specimen thickness.

The three identified mechanisms are cooperative ductile (higher stresses form a big damaged zone consisting of yielded material at the notch or crack tip), solo-crack brittle (with larger thickness the damage zone is very small) and cooperative brittle (characterized by a cloud of micro-cracks that form at the notch tip in low stress, low thickness specimens).

Their results show how important it is to know the dominant mechanism when predicting fatigue crack initiation times, and, as a consequence, when designing load-bearing polycarbonate components.

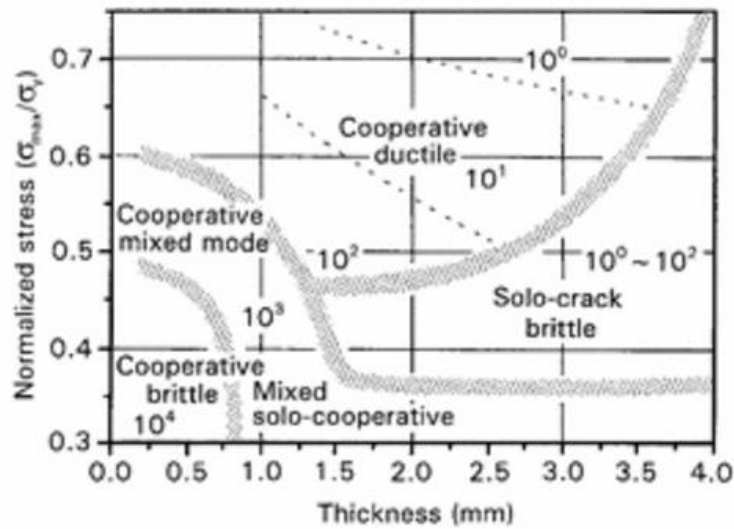


Figure 3.8: Map of crack initiation mechanism, adapted from [58].

Schultz *et al.* [60] investigated the role of crazes in fatigue crack initiation in polycarbonate specimens. They statically pre stressed some of the specimens in order to introduce crazes, then, they compared the fatigue curves (SN curves) obtained from the virgin and damaged specimens. The 6.3mm thick specimens were loaded with a stress ratio of -1, a frequency of 2Hz and at room temperature (about 25°C). Figure 3.9 Shows the reported SN curves.

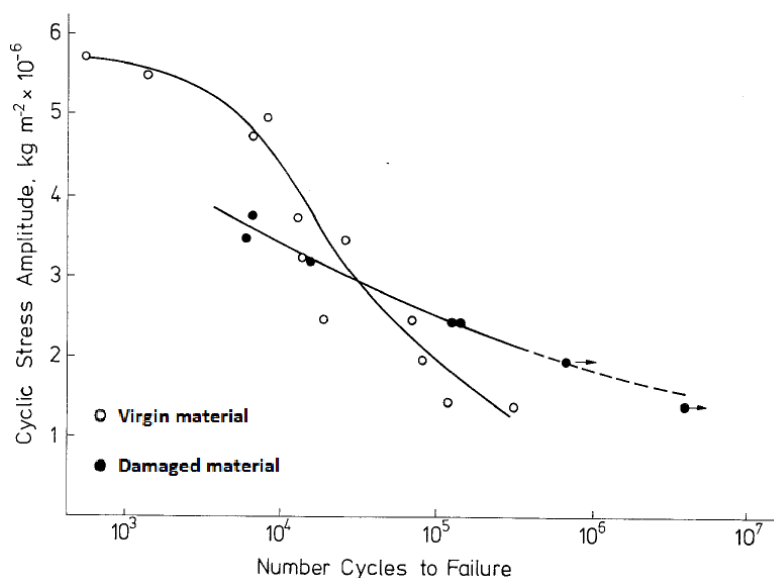


Figure 3.9: SN curves for virgin and pre-stressed polycarbonate specimens, adapted from [60].

The increased life of pre-stressed specimens at the lower stress levels was attributed to a softening effect caused by the gross crazes formed during the static loading phase.

Chen *et al.* [61] also studied fatigue crack initiation in polycarbonate. They used a damage model based on the fracture strain (ϵ_f) to predict the residual life of 6.3mm thick fatigue damaged specimens. The tests had a stress ratio of 0.1, at a constant crosshead speed of 12.7mm/min and at room temperature. Figure 3.10(a) shows their reported SN curve and Figure 3.10(b) shows the predicted damage curve.

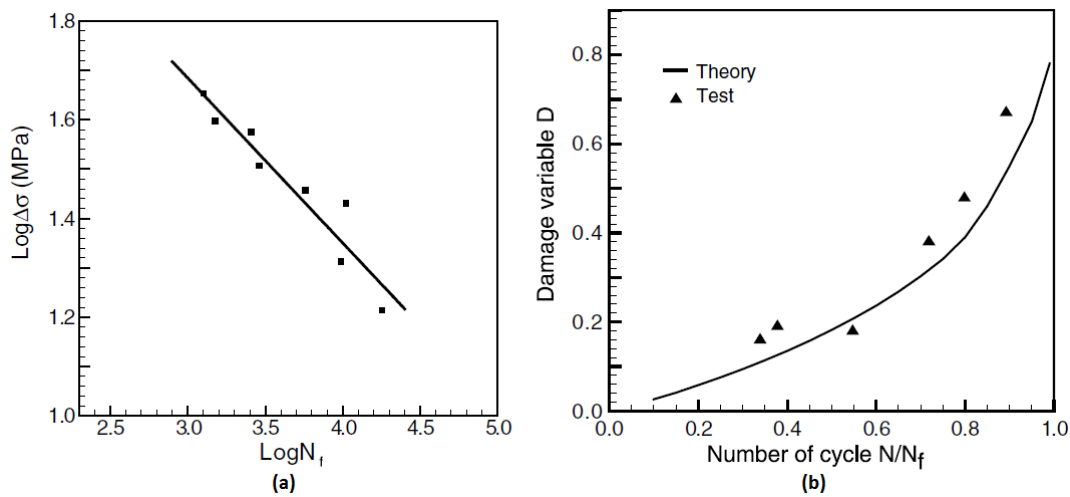


Figure 3.10: a) SN curve for polycarbonate specimens; b) Damage Curve, adapted from [61].

Meijer *et al.* [62] studied the differences between thermal and mechanical failure of polycarbonate subjected to fatigue. In order to do that, they tested two sets of specimens. The first set had isothermal conditions maintained through water cooling, while the second set did not. Figure 3.11(a) shows the reported results for isothermal fatigue and Figure 3.11(b) shows the results for non-isothermal fatigue.

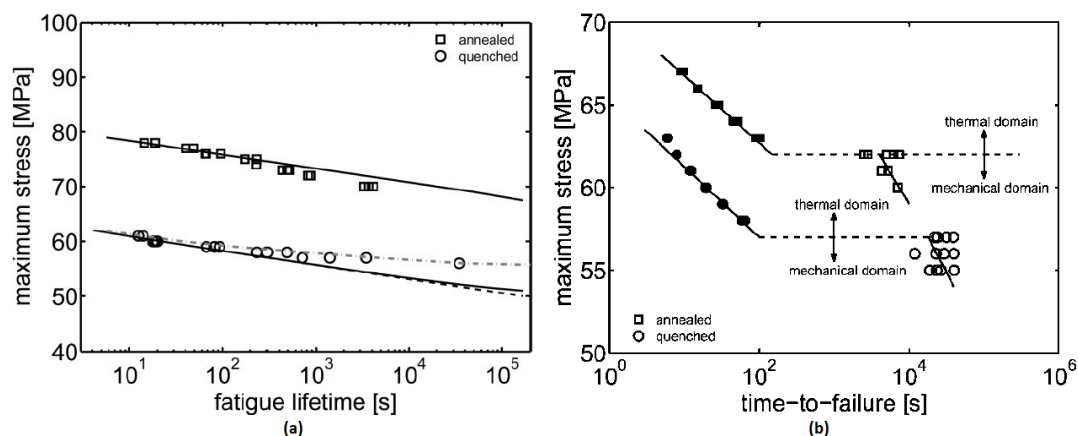


Figure 3.11: a) isothermal; b) non-isothermal fatigue curves for polycarbonate, adapted from [62].

At higher stress levels the temperature rises too much, and ductile failure is caused by dissipative heat, at lower stress levels heat does not factor in the failure process.

Lu *et al.* [63] developed a method for accelerating the fatigue testing of polycarbonate specimens. They used a modified energy activation model that predicted the effects of temperature and stress as fatigue acceleration factors. Through the time-temperature and time-stress superposition, applicable in low frequencies and isothermal conditions, the log-term data was successfully predicted. The tests were made with a stress ratio of 0.1, at 0.5Hz and at room temperature for 1.5mm thick specimens. Figure 3.12 shows the measured long-term SN curve, as well as the curve predicted by short-term data.

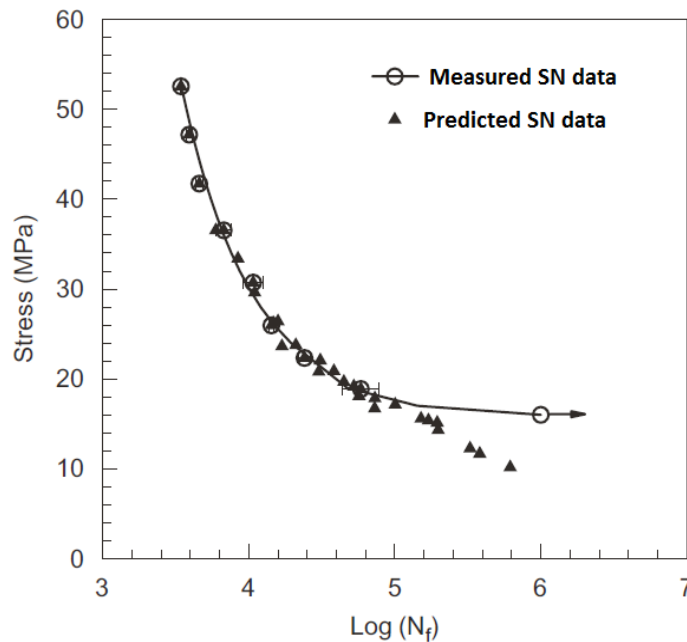


Figure 3.12: Measured and predicted SN curves for polycarbonate, adapted from [63].

4

Pre-Experimental Work

4.1

Introduction

In this chapter, all the pre-experimental details are discussed. Such as, specimen types, dimensions and preparation, loading machine and general experimental procedures and cautions. Specific procedures are presented in subsequent chapters, when needed.

4.2

The Specimens

Two types of specimens were used in the experiments described from here on. The choice of the specimen types was made based on characteristics that made possible the study of many fields at once.

The first type of specimen is the classic constant radius (CR tensile specimen) (adapted from ASTM E466 - Standard Practice for Conducting Force Controlled Constant Amplitude Axial Fatigue Tests of Metallic Materials). It consist of a tensile specimen in which the gauge section is machined with a constant radius, so that the middle cross-section is the critical one and a symmetry plane as well. Figure 4.1 shows the dimensions of the specimens, machined from a 3.9mm thick plate.

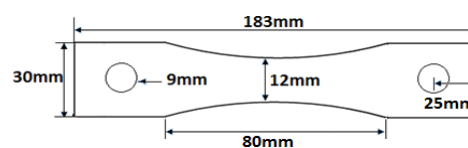


Figure 4.1: Dimensions of the constant radius specimens.

The second type of specimen is the keyhole, developed by SAE in the late 70's. This specimen has a well documented stress concentration factor, similar to typical components, it has a minimum of critical machining dimensions, and permits studies of both crack initiation and propagation [64]. Figure 4.2 shows the dimensions of the specimens, machined from a 3.9mm thick plate.

The stress concentration factor of the keyhole notch was firstly estimated by that of a circular hole in an infinite plate $K_t=3$, since it was designed to simulate this geometry. The K_t for the dimensions described in Figure 4.2 is calculated via finite elements method and experimental techniques, as shown later.

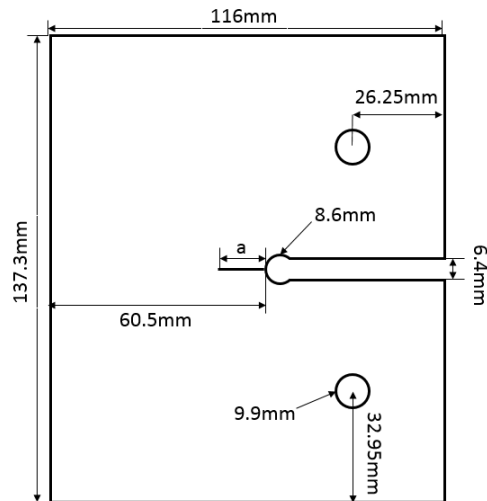


Figure 4.2: Dimensions of the Keyhole specimens.

4.2.1

Loading Cautions

For the constant radius specimens, because of the holes made to fix the specimen to the cyclic loading machine, the middle cross section no longer was the critical section and fatigue cracks were initiating at the loading hole. To remediate this problem, a custom grip was designed, which was able to transmit the load to the specimen by friction, and consequently avoid the stress concentration. Figure 4.3 shows a photo of a specimen mounted with the grips.



Figure 4.3: Constant radius specimen mounted with custom grips.

The loading of the keyhole specimens presented no problem, since the stress concentration guaranteed that fatigue cracks initiated at the notch.

4.2.2

Specimen Preparation

As stated in chapter 2, polycarbonate is a very good choice for thermography applications, since its infrared emissivity is naturally high. Because of that, painting the specimens black was unnecessary and not much preparation should be necessary.

The polycarbonate plate, from where all specimens were machined, was bought from PALRAM Inc., it is called PALSUN™ and is designed to be used as

transparent roofs. They are extruded and rolled, having UV protection applied to one side of the plate. The main material properties can be found on Appendix 3.

The UV protection, as expect, does not interfere with the infrared measurements. This was tested by simply inverting the specimens, pointing the camera to both sides and comparing the readings.

Thus, the only unknown property of the plate was the residual stresses present due to the production process. The easiest way to circumvent this problem was to submit the specimens to an annealing heat treatment, eliminating not only the unknown pre-existing residual stresses, but the ones added in the machining process as well. Figure 4.4 shows the isochromatic fringe patterns of an unloaded specimen, (a) before annealing and (b) after annealing, in a photoelastic transmission polariscope.

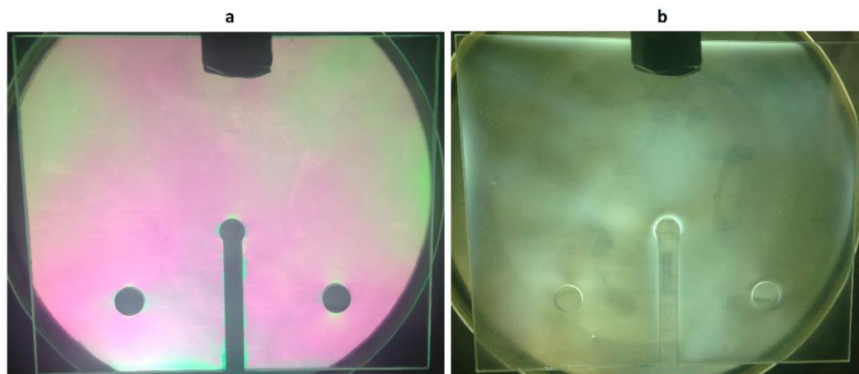


Figure 4.4: a) Specimen before annealing. b) After annealing.

The adapted annealing process consisted of a simplified version of what is described in [65]. Basically, heating the specimen above its glass transition, at a constant rate, keeping it at a constant temperature for a extended period of time, and then cooling it slowly at a constant rate². Table 4.1 show the temperatures and times of the annealing heat treatment.

Process	Temperatures (°C)	Time (Hours)
Constant rate heating	25-160	4
Constant temperature	160	6
Constant rate cooling	160-25	4

Table 4.1: Temperatures and times of the adapted annealing heat treatment.

² The annealing heat treatment was made in an electric circulation oven from Photolastic inc. coupled with a cam control unit from Partlow corp. (40-230°C), which followed the temperatures described above, and a mercury-in-glass thermometer that was used to calibrate the temperature of the oven.

The specimens were covered in talcum powder, acting as a lubricant and permitting free two-dimensional movement of the specimen between two glass plates, which prevented non-uniform deformation. After annealing, the dimensions of the specimens changed (about 1.7-2.0% in the preferential direction of the plate, along the length of the CR specimen), because of the stress relief. The dimensions reported before, in Figure 4.1 and Figure 4.2, were measured after annealing.

4.3

Cyclic Loading Machine

In order to study fatigue behavior, cyclic loading must be used. In the present work, a pneumatic loading machine developed by [66] was used.

The machine, equipped with a servo valve³ controlled via a simple computer program, applied a cyclic load with fixed frequency of 5Hz. The magnitude of the load was controlled through three valves that regulated the pressure of air entering the pneumatic muscle and how easily the air was expelled after each cycle. A load cell⁴, connected in series with the specimen, was responsible for feeding the load response to the program. Figure 4.5 shows a photo of the setup with a CR tensile specimen mounted on the grips, while Figure 4.6 shows a screenshot of the controlling program.

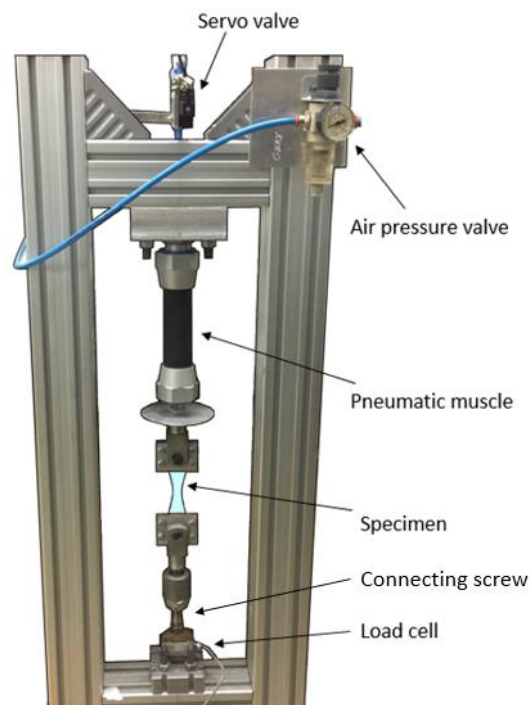


Figure 4.5: Photo of the pneumatic loading machine setup.

³ Servo-valve – FESTO MHE4-MS1H-3/2G-1/4 (-0.9 – 8bar)

⁴ Load cell – MK Controle e Instrumentação Ltda. CSR-500 (5kN)

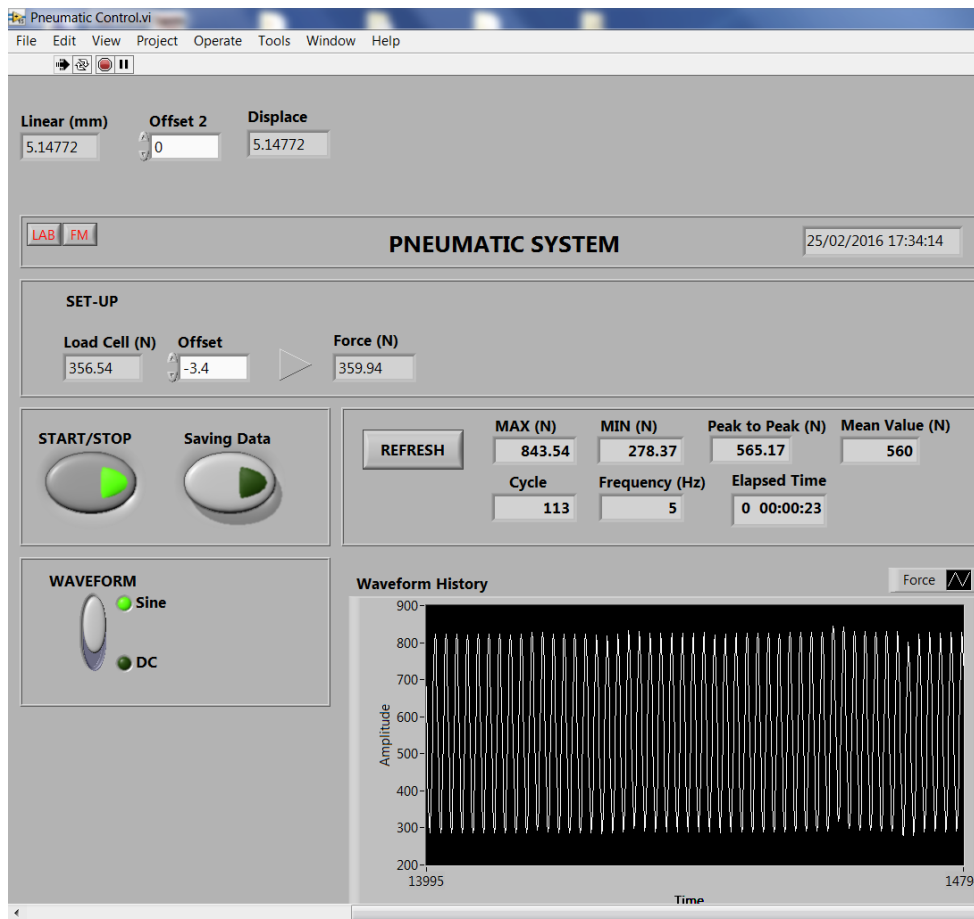


Figure 4.6: Screenshot of the program controlling the pneumatic machine.

The rather simple setup, although very efficient in applying the cyclic loading, did not allow much freedom when controlling some of the load parameters. Mainly, both the maximum and minimum loads were functions of the air pressure, making the load ratio (min load / max load) an intrinsic parameter of the machine. That being said, all tests accounted for mean stress effect, and when it would be impossible, the load ratio was made constant.

4.4

General Experimental Procedures and Cautions

This section summarizes some of the procedures and cautions that were taken throughout all experiments described in the next two chapters.

4.4.1

Machine Cautions

Because of the two different types of specimens and their different lengths, it was necessary to change the loading machine setup accordingly. Since the specimens were connected in series with the pneumatic muscle and the load cell, the distance between them needed to accommodate the lengths of both the longer

CR tensile specimen and the shorter keyhole specimens. In order to do that, two different length screws were used to connect the lower grip to the loading cell (as can be seen in Figure 4.5).

Because of the differing lengths of these screws, their weights were obviously different, and since the loading cell is connected at the bottom of the setup, the load offset had to be set for each specimen. The load measurements discounted the weight of the setup.

Another caution concerned the machine's grips that had a fixed spacing, which was different from the thickness of the polycarbonate specimens. That generated a problem of misalignment of the specimens, resulting in bending stresses. In the case of the CR tensile specimen this problem was circumvented by the use of the custom grips (as discussed before). For the keyhole specimens, spacers were added between the machine's grips and the specimens, in order to properly align them.

Lastly, because of the in-series setup of the machine, and the nature of the pneumatic muscle, the load applied to the specimen was a function of the specimen's stiffness. The problem is that a direct correlation between air pressure and load was not possible for all the experiments as a whole, but only for each specific situation separately. For the CR tensile specimens where cracks were not an issue and the stiffness was constant throughout the test, that was not much of a problem. On the other hand, for the crack propagation tests using the keyhole specimens, the air pressure needed to be constantly monitored and adjusted by hand, in order to keep the desired load levels.

4.4.2

Infrared Camera Cautions

While using the infrared camera for either active or passive thermography applications, there are some cautions to be taken. The cautions described here are specific for the non-cooled, micro bolometer camera FLIR A655sc.

Firstly, when turning on the camera before each test, it is recommended to wait some time until the camera itself reaches an equilibrium temperature. Around 10 to 15 minutes should be enough, and after that period of time the measurements can be made for very long time. The camera has been used for over 8 hours straight and measurements remained constant.

Another important aspect of the camera, specifically because of the workings of the focal plane array, it has a high non-uniform response to radiation, that means, each pixel is responding differently to the same level of infrared radiation. The A655sc has an automatic non-uniformity correction (NUC) procedure, which lowers a plate with very high emissivity in front of the detectors and uses the data collected from it, at two different temperatures, to assign a gain and an offset value to each pixel.

The manufacturer of the camera (FLIR Inc.) advises the use of this NUC procedure every 15 to 30 minutes to guarantee the precision of the measurements. The problem is that doing it in the middle of a test can throw off one's results, because the gain will change and early results will not be comparable to later ones, since the value of these gains cannot be easily obtained. The advice from the TSA software (Stress Photonics Inc.), which was followed and approved by this work, is to turn off the automatic NUC procedure and run it manually before each test. Additionally, although no effort to explain why it happens is made here, the author of this work found out that after using the camera for more than 30 minutes or so the NUC procedure barely changed the gains and offsets.

Lastly, a comment about the very high sensitivity of the camera and some effects that arise from it that may not be obvious. Anything with temperature above 0K emits infrared radiation. Because of that, almost everything around a lab environment can interfere in one's results. Things like laptops, power supplies, people walking around the lab and even the camera itself can emit considerable amounts of radiation that may be reflected by the target and back to the detector. This should not be a problem when making TSA measurements, because it uses only temperature variations, but it certainly can be a huge problem when measuring actual temperature values in active thermography, for example.

In order to minimize this problem, two cautions are advised. Placing the camera right in front of a wall so that nothing is actually happening behind it, while protecting the target and the surrounding area that is in front of the camera with some kind of infrared opaque material, wood, cloth and styrofoam have been successfully used for this purpose. Avoiding the camera's own reflection can be tricky, but can usually be accomplished by pointing the camera at the target at an angle.

5

Thermography Applied to Fatigue Crack Initiation

This chapter is divided in four main parts concerning fatigue crack initiation studies. Firstly, it discusses how to use thermography to locate critical points in a component, then, an in-depth discussion on how to measure stress concentration factors using TSA is made. Determination of fatigue limit is discussed next, laying the theoretical ground for complete SN curve measurements through pure thermography.

5.1

Locating Critical Points

In order to locate critical points, where fatigue is most likely to happen, there are two possible approaches. The active thermography approach (exemplified in Appendix 1) and the passive thermography approach, through TSA.

Considering that in most applications the critical point is located at a free surface of the component, one of the principal stress components is equal to 0 (e.g. $\sigma_2=0$) and the TSA data can be easily converted in the actual stress acting at each point of the free surface. Then, the highest stress point, also the one with highest TSA magnitude, is obviously the critical one. Difficulties may arise when a more complicated stress field is present and the critical point might not be on a free surface. In that case, some stress separation technique must be used, be it numerical or experimental, in order to obtain the actual values of σ_1 and σ_2 . Then, a criterion such as Tresca's or Mises' should be used to combine these components and determine which point is the critical one. Some of these techniques are discussed in the next section. Figure 5.1 shows how easily the critical points can be located in a cracked T-shaped specimen under cyclic loading using TSA [17].

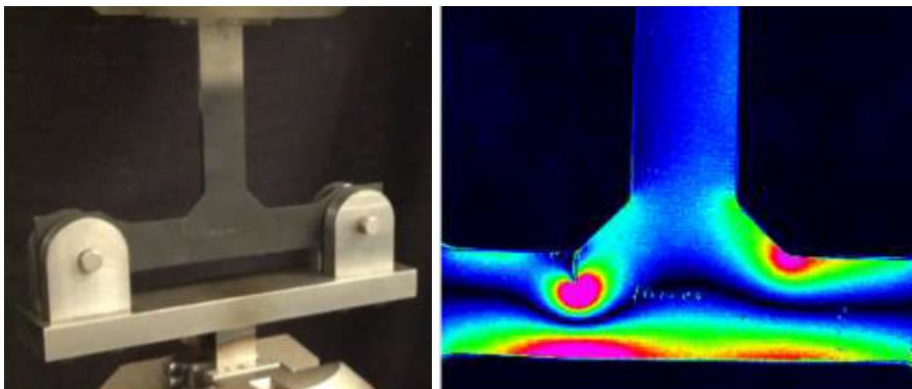


Figure 5.1: Cracked T-shaped specimen and critical points, adapted from [17].

5.2

Determining Stress Concentration Factors

By analyzing what has already been presented about TSA, it should be clear that it is very well suited for measuring stress concentrations. The only problem is a small loss of data near the edges of the specimen, exactly where the maximum stress needs to be measured. This is an issue common to most optical experimental stress analysis techniques, such as DIC and photoelasticity.

Two possible data extrapolation approaches are presented next and are used to calculate the stress concentration factor of a keyhole polycarbonate specimen.

5.2.1

Approach 1 – Simple Extrapolation of Line Data

In this approach a simple extrapolation of the line data ahead of the notch tip is used in order to calculate the K_t . This strategy has been used before by the author in [45].

Firstly, the TSA calibration was done using one of the CR tensile specimens described in chapter 4. The process, as described in chapter 2, consists of loading the specimen with a known cyclic load and using equation 2.23 to calculate the calibration factor A:

$$A S = (\Delta\sigma_1 + \Delta\sigma_2) \quad (5.1)$$

Since the CR specimen has only a σ_1 component, the calibration is easily done. Figure 5.2a shows the TSA magnitude map for the calibration specimen (with the reference window), while Figure 5.2b shows the line plot for the critical line.

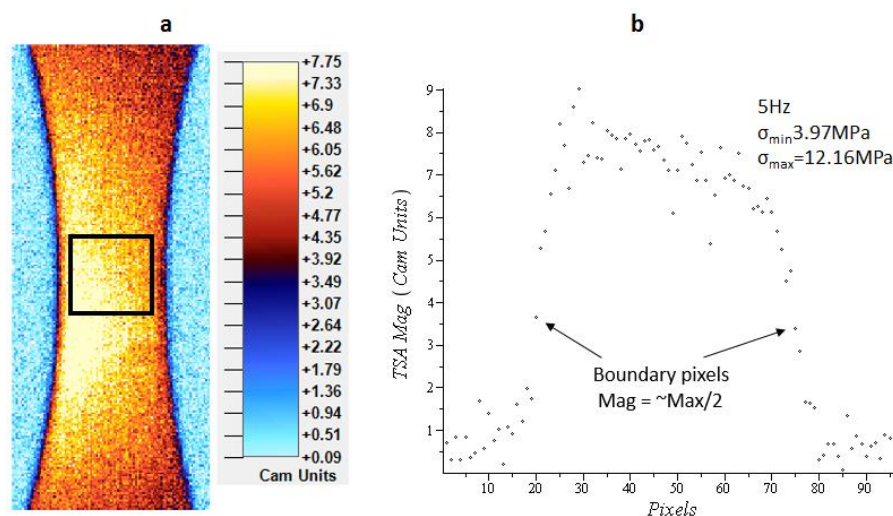


Figure 5.2: a) TSA magnitude map and b) critical line plot for CR specimen under $\Delta\sigma=8.18\text{MPa}$.

Figure 5.3 shows the plot of Stress vs TSA magnitude for 5 different $\Delta\sigma$, a linear relationship is evident and the angular coefficient is the calibration factor ($A=1.12$ MPa/Cam Units), while the linear coefficient ($B=0.015$) is very small.

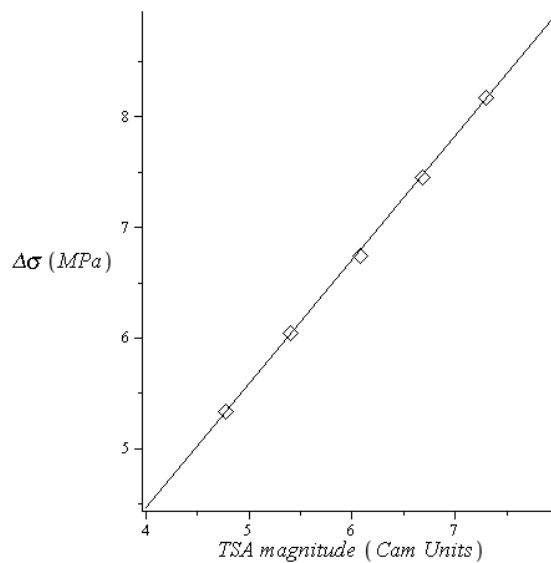


Figure 5.3: Calibration Stress vs TSA magnitude graph for 5 different $\Delta\sigma$.

With the calibration factor in hands, the next step is to cyclic load one of the keyhole specimens. Figure 5.4 a shows the resulting TSA magnitude map while b shows the phase map.

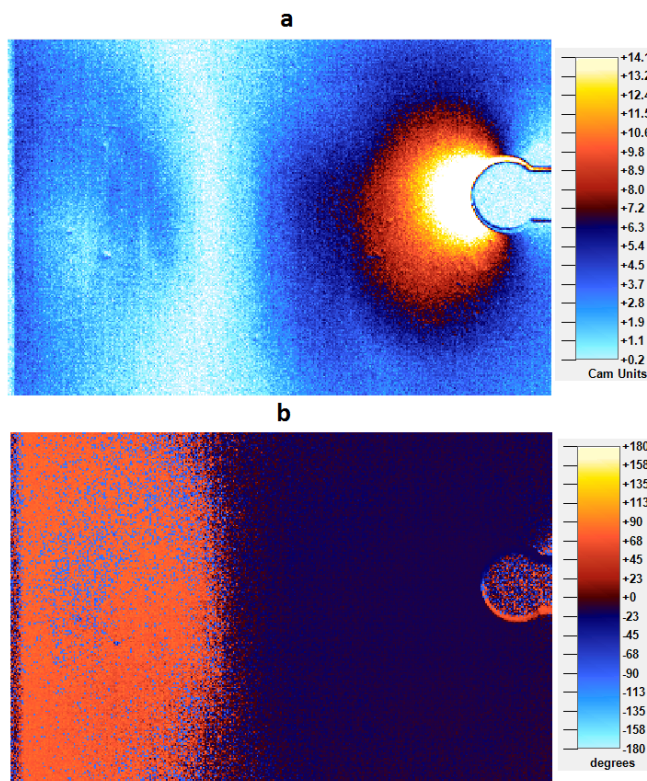


Figure 5.4: a) TSA magnitude map; b) TSA phase map of a keyhole specimen.

Then, the raw line data, determined by the line in which the maximum magnitude value occurred, is plotted in Figure 5.5 and Figure 5.6, showing the magnitude and phase data respectively.

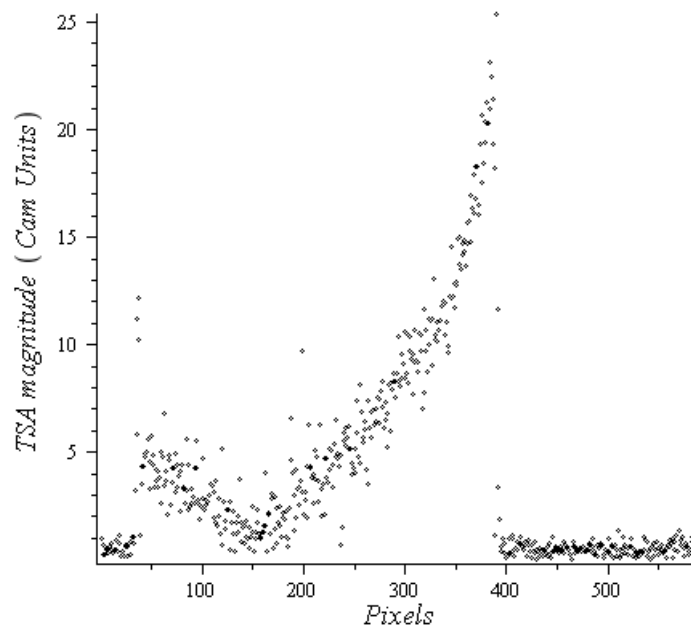


Figure 5.5: Magnitude line data for the keyhole specimen.

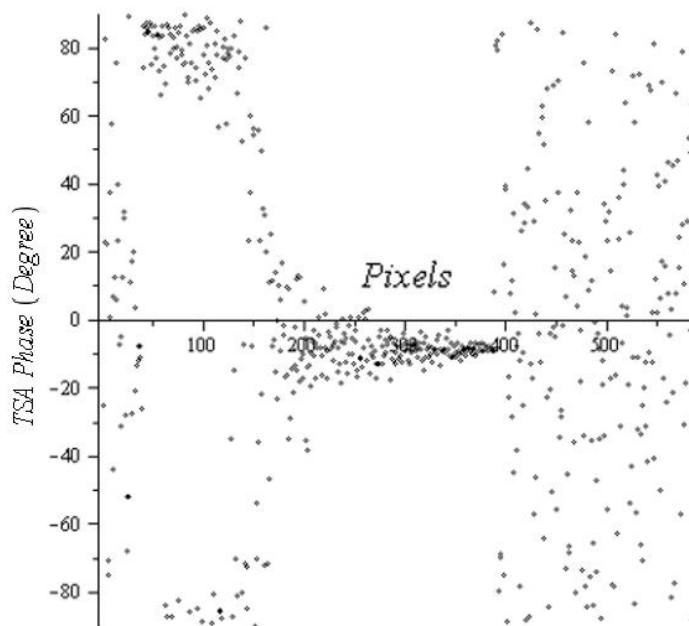


Figure 5.6: Phase line data for the keyhole specimen.

As described in chapter 2, the phase data can be used to correct the magnitude signals. The points where the phase angle differs from the phase angle seen in the tension region (pixel 150 to pixel 400) need to have their signals reversed. Figure 5.7 shows the magnitude corrected by phase data.

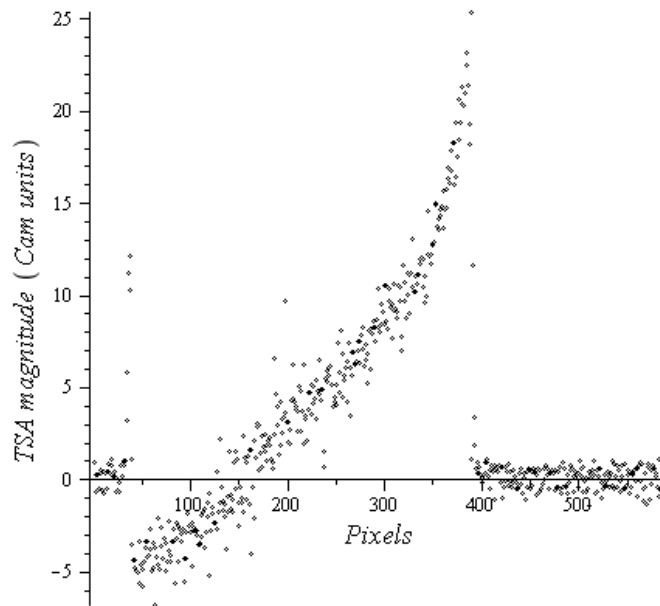


Figure 5.7: Magnitude data corrected by phase angle.

By excluding the points that are not part of the specimen's surface, and inverting the pixel numbers so that the pixel 0 is the one at the notch tip, the graph in Figure 5.8 is the result.

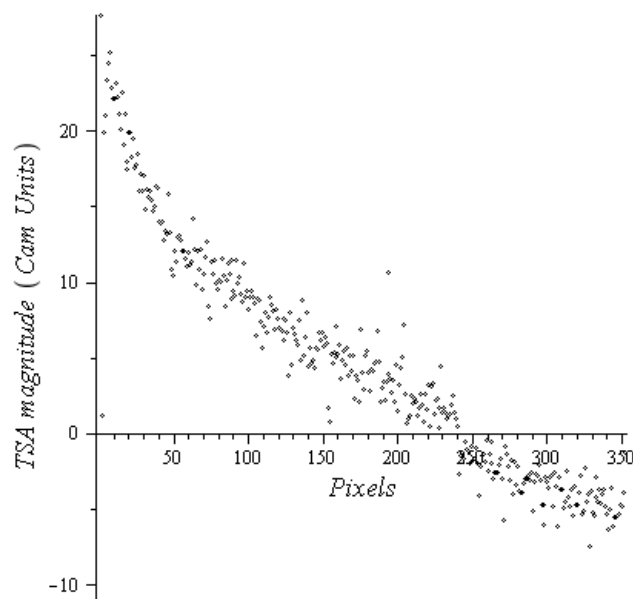


Figure 5.8: Treated TSA data points for keyhole specimen.

The next step is to apply both the stress calibration of TSA and the length scale. The length scale is simply determined by measuring the length of the section ahead of the notch (60.5mm) and dividing it by the number of pixels in Figure 5.8 (353 pixels), giving a length scale of 0.1714 mm/pixel. Figure 5.9 shows the normalized stress vs distance from notch plot, with $\Delta P=420\text{N}$ (the cyclic load) and $R=4.3\text{mm}$ (the radius of the notch).

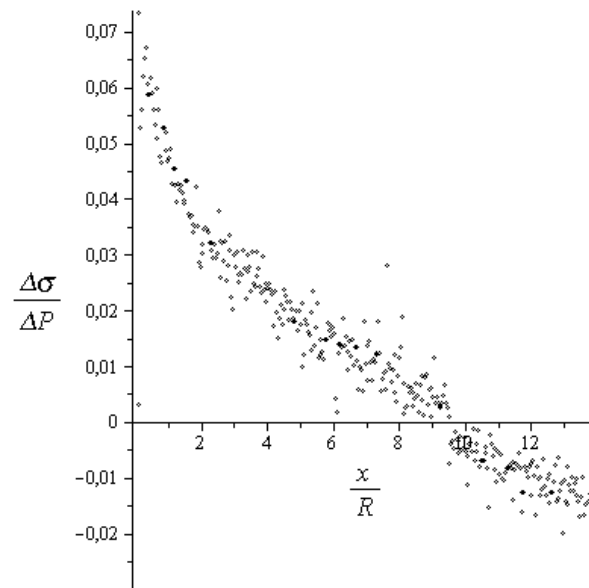


Figure 5.9: Normalized stress vs distance from notch plot for keyhole.

Figure 5.10 shows the resulting extrapolation using the data points from pixel 1 to pixel 100 to fit a curve following equation 5.2⁵

$$\frac{\Delta\sigma}{\Delta P} = \frac{C0}{(1 + x/R)^h} + C1 + C2(1 + x/R) \quad (5.2)$$

where the coefficients C0, C1 and C2, as well as the exponent h are fitting parameters to be determined via the minimum squared error method.

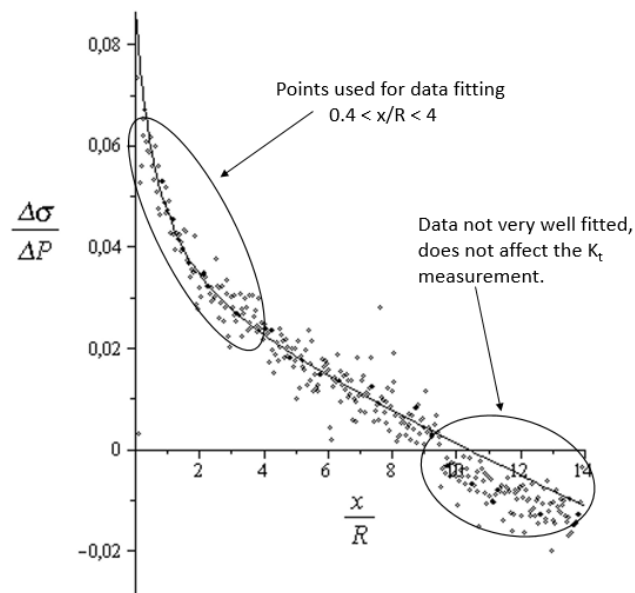


Figure 5.10: Curve-fitted TSA data for keyhole specimen.

⁵ This equation was chosen because of the expected $1/x^h$ dependency of the stresses. The other terms were added in order to fit the data farther from the notch tip.

From the fitted curve, the maximum stress at the notch tip can be determined and used to calculate the stress concentration factor. The maximum stress was $(\Delta\sigma/\Delta P)_{max} = 0.0864$, and the nominal stress was calculated as the sum of the tensile and bending stresses via equation 5.3

$$\left(\frac{\Delta\sigma}{\Delta P}\right)_{nom} = \frac{1}{t b} + \frac{1 \left(B - H_b - \frac{b}{2} \right) \left(\frac{b}{2} \right)}{\frac{t b^3}{12}} = 0.0292 \quad (5.3)$$

where t is the specimen thickness (3.9mm), b is the length of the section ahead of the notch (60.5mm), B is the total width (116mm) and H_b is the horizontal distance of the loading pin to the border (26.25mm). Then, (with a fitting exponent h of ~ 0.65) the resulting K_t is:

$$K_t = \left(\frac{\Delta\sigma}{\Delta P}\right)_{max} / \left(\frac{\Delta\sigma}{\Delta P}\right)_{nom} = 2.95 \quad (5.4)$$

5.2.2

Approach 2 – Stress Function and Principal Stresses Separation

In order to obtain better results and showcase the power of hybrid TSA, this approach uses an Airy's stress function to fit the TSA data in an area around the notch. By doing this, the stress components are determined and the K_t calculated.

Instead of collecting the data only from the line ahead of the notch tip, the procedure now collects data from the whole area show in Figure 5.11, measuring 315 pixels long and 127 pixels wide, leaving a minimum of 6 pixels between collected data and the borders of the specimen⁶.

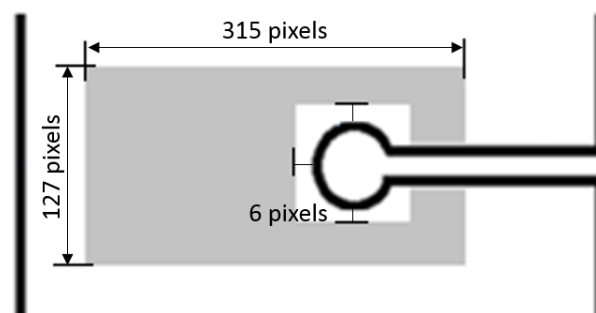


Figure 5.11: Area, in gray, for stress function fitting.

The stress function used to fit the data was adapted from [19] and is reproduced in equation 5.5 below:

⁶ The dimensions are given in pixels because in each experiment the distance from the camera to the specimen is different. The algorithms only translate the lengths to mm at the end of computations.

$$\begin{aligned} \Phi = & b_0 \ln(r) + c_0 r^2 + \left(\frac{c'_1}{r} + d'_1 r^3 \right) \cos(\theta) \\ & + \sum_{n=2}^N [(a'_n r^n + b'_n r^{n+2} + c'_n r^{-n} + d'_n r^{2-n}) \cos(n\theta)] \end{aligned} \quad (5.5)$$

where b_0 , c_0 , c'_1 , d'_1 , a'_n , b'_n , c'_n and d'_n are the fitting coefficients that are later determined via least mean squares method, r and θ are the polar coordinates of each point with respect to the origin at the center of the notch. N is one fourth of the number of terms minus 4 terms (b_0 , c_0 , c'_1 , d'_1).

Then, using equation 3.10, repeated here as equation 5.6, the stress components can be determined for all points of the specimen.

$$\begin{aligned} \sigma_\theta &= \frac{\partial^2 \Phi}{\partial r^2} \\ \sigma_r &= \frac{1}{r} \frac{\partial \Phi}{\partial r} + \frac{1}{r^2} \frac{\partial^2 \Phi}{\partial \theta^2} \\ \sigma_{r\theta} &= -\frac{\partial}{\partial r} \left(\frac{1}{r} \frac{\partial \Phi}{\partial \theta} \right) \end{aligned} \quad (5.6)$$

For the results shown, 84 terms ($N=20$) were used in the fitting of 31328 experimental data points and 30060 boundary condition points evenly distributed as $\sigma_r = \sigma_{r\theta} = 0$ at the notch border, $\sigma_x = \sigma_{xy} = 0$ at the back free surface and $\sigma_y = \sigma_{xy} = 0$ at both the slit's free surfaces. Figure 5.12 shows the tangential stress (σ_θ) distribution.

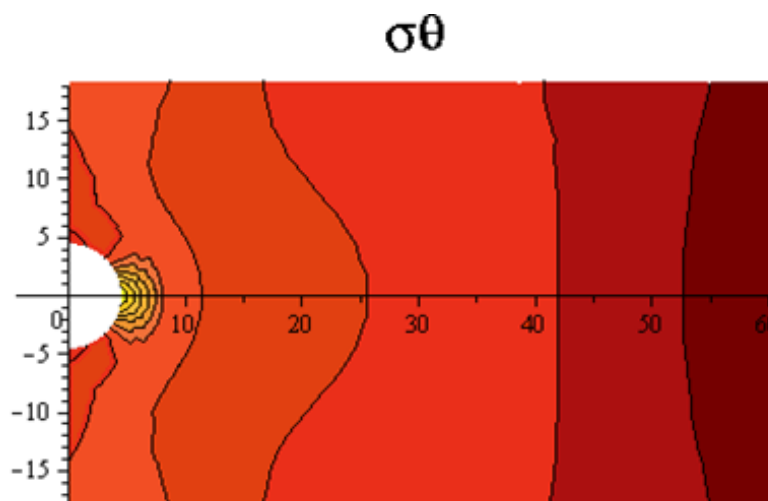


Figure 5.12: Fitted σ_θ field.

The linear least mean squares method used to fit the data is very well described in [67] and can be resumed by one matrix equation.

$$b = [[A]^T [A]]^{-1} [A]^T c \quad (5.7)$$

with

$$[A]_{m \times k} b_k = c_m \quad (5.8)$$

where, b is the vector of the Airy's coefficients, c is the vector with the experimental data and zeros for the boundary conditions and A is the matrix filled by the numerical part of the equations obtained by equation 5.6 after substituting the coordinates of each experimental and boundary point. With $m=31328+30060$ and $k=84$ ($k= n \cdot 4 + 4$).

Figure 5.13 shows the line plots of the principal stress components and their combinations (σ_1 , σ_2 , $\sigma_1 + \sigma_2$ that can be compared to the actual TSA data points and $\sigma_1 - \sigma_2$ that is compared to photoelastic data) for the line ahead of the notch.

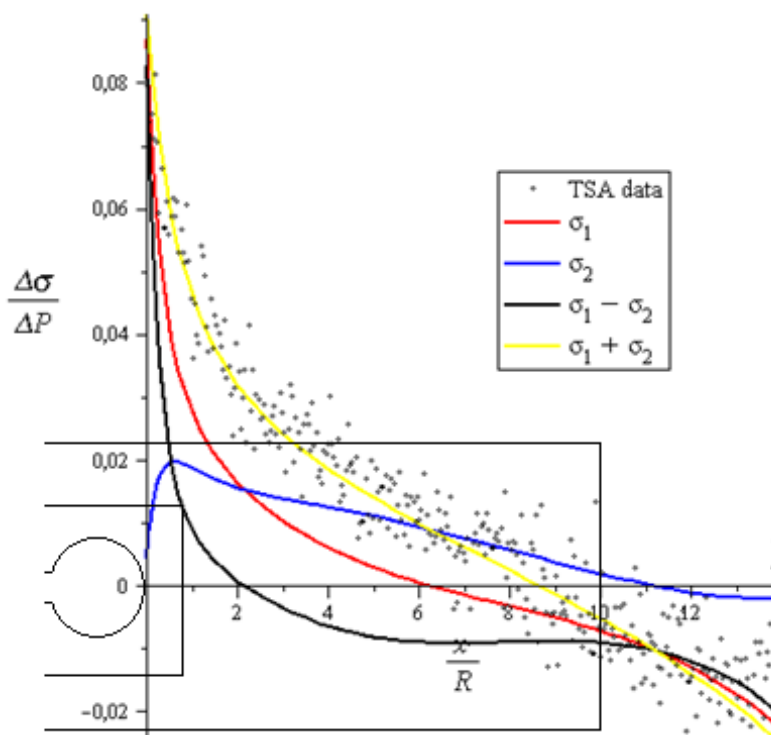


Figure 5.13: Fitted stress components for line ahead of notch.

The behavior of the stress components are as expected, with σ_2 tending to 0 near the notch tip as σ_1 gets to its maximum. The maximum value of σ_1 obtained was $\sigma_{\max}/\Delta P = 0.091$, which results in a K_t of 3.13.

For verification purposes, the stress concentration factor was measured via DIC and Photoelasticity, as well as calculated through the finite elements method. The procedures are described in Appendix 4 and Appendix 5. Table 5.1 shows the results obtained.

	TSA ap1	TSA ap2	DIC	Photoelasticity	FEM	Literature [64]
K_t	2.95	3.13	3.27	3.25	3.02	3 - 3.25

Table 5.1: Results for the K_t of the keyhole specimen.

Finally, Figure 5.14 shows the line plots ahead of the notch, obtained by the TSA approach 2, DIC and Photoelasticity measurements.

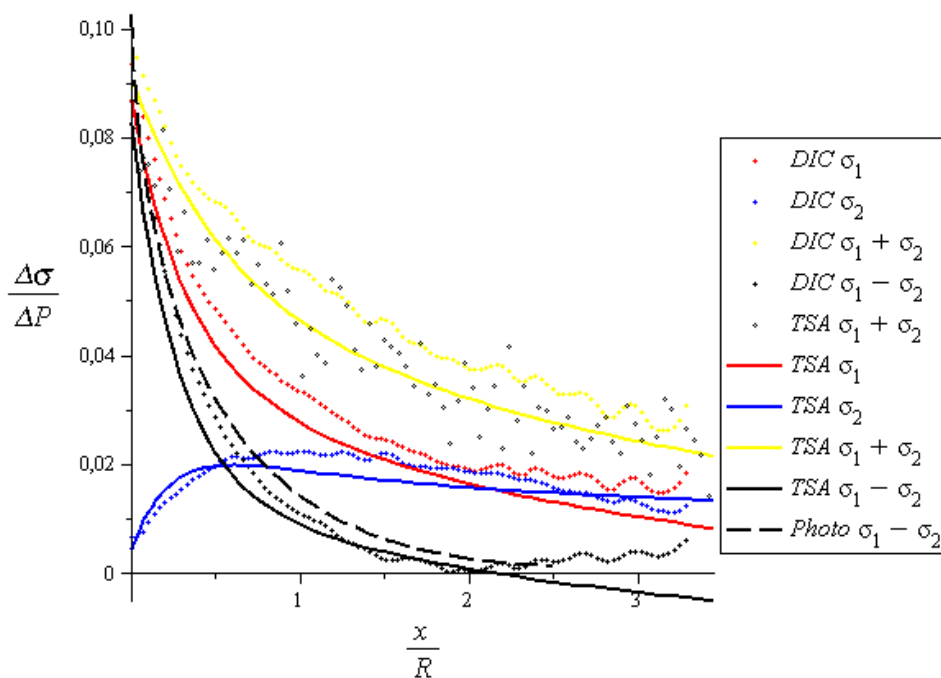


Figure 5.14: TSA, DIC and Photoelasticity results for the line ahead of notch.

5.3

Measuring Fatigue Limit Using Thermography

As pointed before, measuring the fatigue limit of a material in the traditional way takes a very long time. Risitano *et al.* [68] proposed a methodology for the rapid determination of this property using thermography.

The idea behind the method is based on the reported rise in temperature of a specimen cyclic loaded above the fatigue limit. This temperature rise is usually explained by a combination of the thermoelastic effect and internal damping within the elastic field.

When a specimen is cyclic loaded, the temperature (T) vs number of cycles (N) curve is similar to the one show in Figure 5.15 [69].

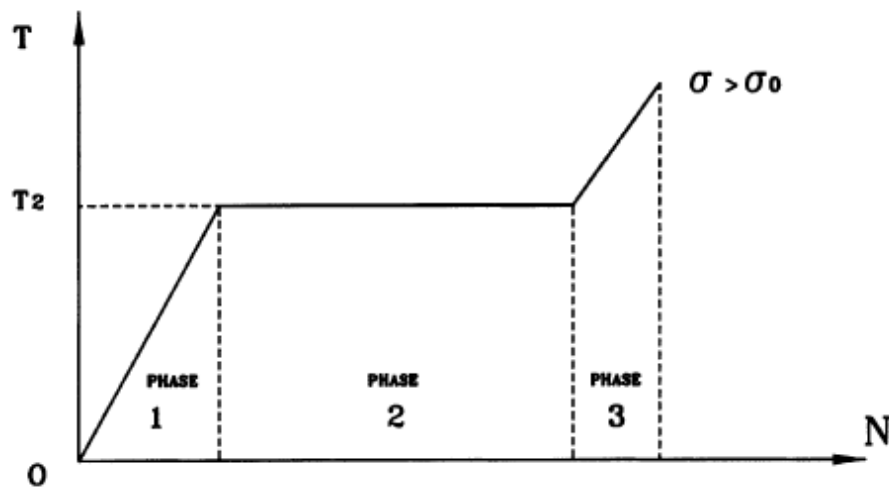


Figure 5.15: T vs N curve for cyclic load above the fatigue limit, adapted from [69].

The curve clearly shows three phases. Phase 1, where the temperature rises, and in this region, the rate of heating is higher for higher stresses. Phase 2, where the temperature stabilizes. The stabilization temperature is higher for higher stresses. Finally, phase 3, where the temperature rapidly rises again, and final failure is imminent.

The idea is to measure the stabilization temperature of several different stress levels, from lower to higher, in a single specimen. Then, subtract the initial temperature of the specimen and use an unloaded specimen placed by its side as the ambient temperature reference and use equation 5.9 to calculate the data points for each stress level.

$$T(n) = (T_{max}(n) - T_{amb}(n)) - ((T_{max}(1) - T_{amb}(1))) \quad (5.9)$$

where $T(n)$ is the temperature elevation at the cycle n , $T_{max}(n)$ is the maximum temperature of the observed area on the surface of the loaded specimen at cycle n , $T_{amb}(n)$ is the temperature of the surface of the reference specimen at cycle n , $T_{max}(1)$ and $T_{amb}(1)$ are the maximum and reference temperatures at the first cycle.

The CR tensile specimen is cyclic loaded in a stair case pattern, as shown in Figure 5.16. Because of the loading machine limitations, described in chapter 4, the mean load was not constant, and the Goodman's relationship was used to account for that. Figure 5.17 shows the $T(n)$ vs n curve for the first, fifth, seventh and ninth stress levels, while Figure 5.18 shows two thermographic images obtained before loading and during the 7th load level.

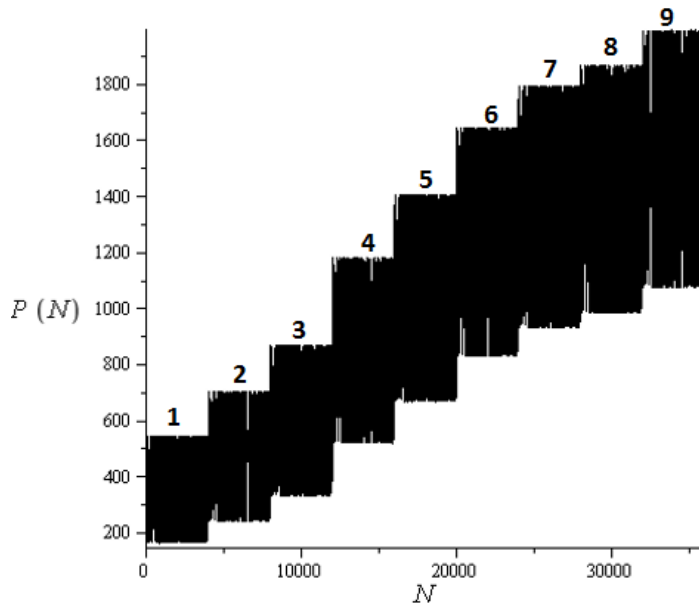


Figure 5.16: Loading steps for fatigue limit evaluation.

PUC-Rio - Certificação Digital N° 1412756/CA

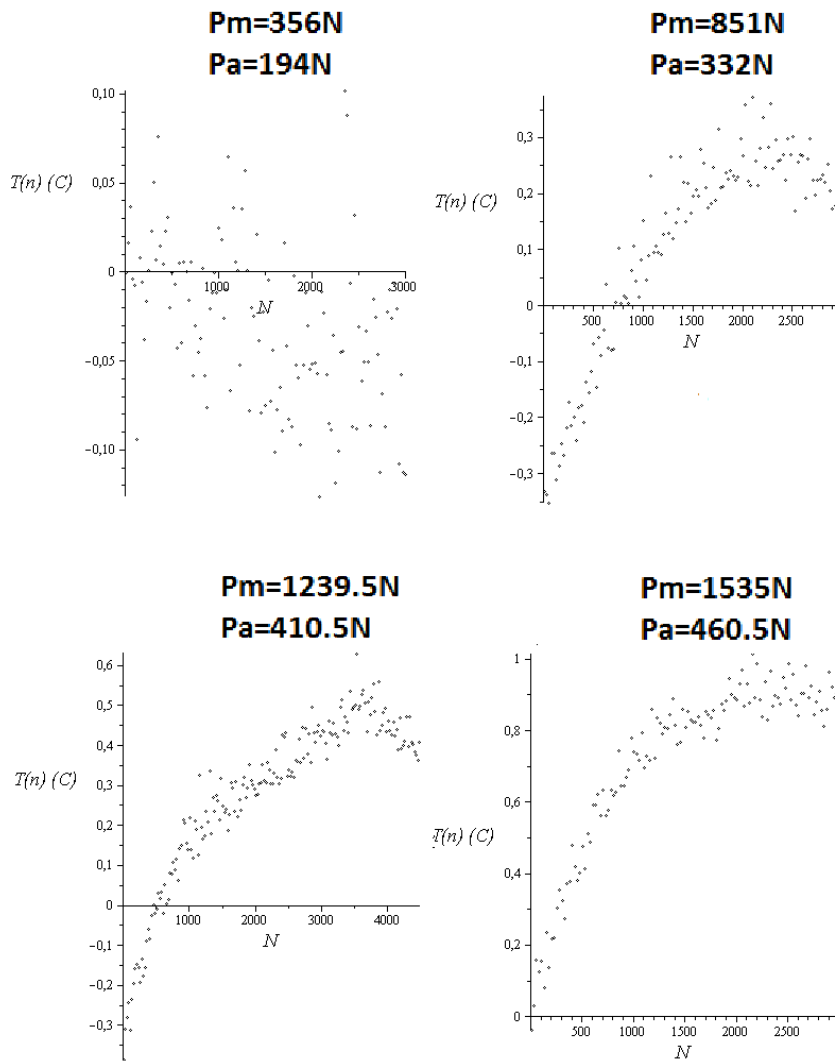


Figure 5.17: $T(n)$ vs cycles points for 4 different load levels.

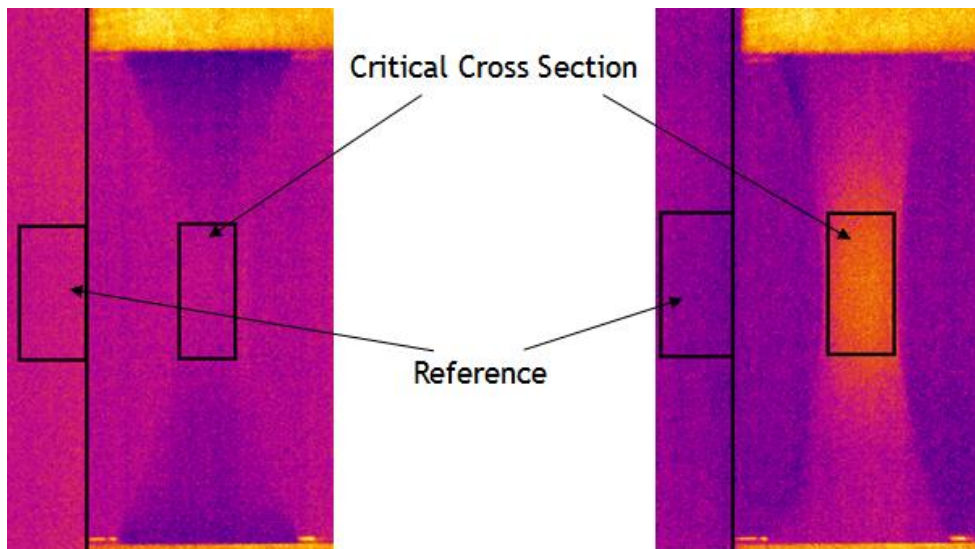


Figure 5.18: Thermographic image at the 7th load level.

Table 5.2 shows the summarized results for each stress level, as well as the Goodman's equivalent alternating stress (σ_a eq). Then, plotting the stabilization temperature as a function of the alternating stress, Figure 5.19 shows that above a certain stress the temperature rises considerably faster.

Load level	P_a (N)	P_m (N)	σ_m (MPa)	σ_a (MPa)	σ_a eq Goodman (MPa)	Stabilization T(n) (°C)
1	194	356	7.5	4.1	4.6	0.088
2	232.	473	9.9	4.9	5.8	0.115
3	270.	601	12.6	5.7	7.1	0.179
4	332	851	17.9	7.0	9.6	0.244
5	372	1039	21.8	7.8	11.8	0.339
6	410.	1239.	26.0	8.6	14.4	0.461
7	433.	1364.	28.7	9.1	16.3	0.591
8	444	1426	30.0	9.3	17.3	0.718
9	460.	1535.	32.3	9.7	19.2	0.877

Table 5.2: Summarized results for the fatigue limit test.

The Risitano method, or thermographic method, then extrapolates the data using two lines, and determine the fatigue limit at the point where they cross each other.

The literature indicates a high range for possible polycarbonate fatigue limits, Plastifab Inc. [70] reports 6.89MPa, [71] reports a range from 6.89MPa to 13.78MPa for non-reinforced polycarbonate and [72] reports a range from about 6MPa to around 13MPa.

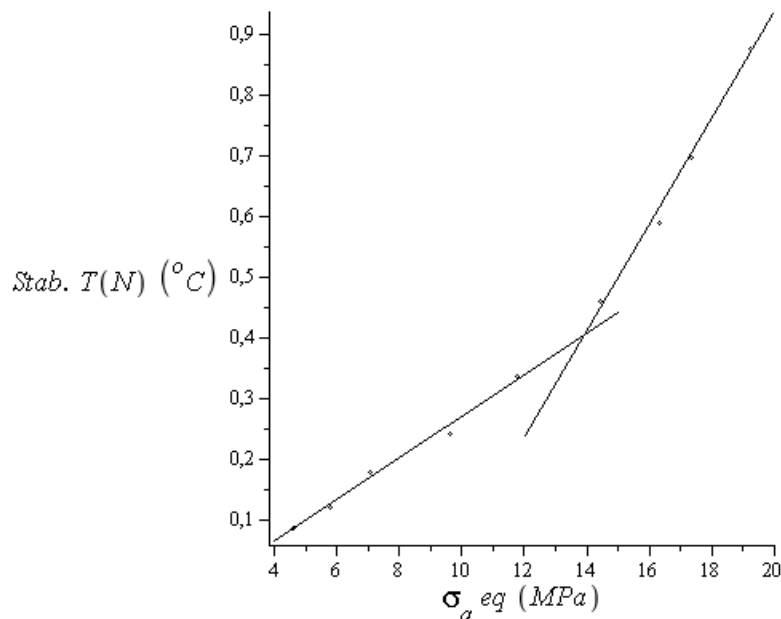


Figure 5.19: $T(N)$ vs σ_a eq for polycarbonate.

The resulting fatigue limit is $\sigma_0 = 13.8$ MPa. Although this result agrees with what was found in the literature, it is in the high-end of the possible spectrum, and the author believes that it should not be the case⁷. Errors of about $\pm 15\%$ have been reported in the application of the thermographic method [68], which would give a possible range of fatigue limit for polycarbonate from 11.7 MPa to 15.9 MPa :

$$\sigma_0 = 13.8 \pm 15\% \quad (5.10)$$

5.4

Determination of the Fatigue Curve Using Thermography

Risitano *et al.* [69] proposed a method, based on the methodology to measure the fatigue limit, to determine the whole fatigue curve of a material using thermography. This method, once again, is much faster than the traditional method to bring up this data, and needs theoretically only one specimen. In practice, three specimens is the recommended minimum.

The main idea behind this method is an energy approach to damage

$$E_c = \int_0^{N_f} E_p dN \quad (5.11)$$

⁷ If instead of using Goodman's model, the Gerber's model for equivalent stress was used, the resulting fatigue limit would be 9.6 MPa. Nonetheless, the Goodman's equation is used throughout this work since it is more oftenly used in the polycarbonate literature.

where, E_c is the amount of micro-plastic deformation energy to failure per unit volume, a material property, N_f is the number of cycles to failure and E_p is the energy due to yielding per unit volume per cycle.

The argument of energy equilibrium is then used,

$$E_w = E_i + Q \quad (5.12)$$

balancing the work done over the system by the loading (E_w), the stored internal energy (E_i) and the energy converted into heat (Q). Assuming E_i to be small compared to Q , and using Risitano's results, which have shown E_w to be proportional to E_p , the authors of [69] proposed

$$E_c = \int_0^{T_f} dQ \quad (5.13)$$

For small temperature variations (under 100K, implies small loading frequencies), the heat transferred from the specimen to the environment can be considered proportional to the temperature difference $T(n)$. Because of that, Q can be evaluated through a parameter Φ , which is the integral of the T vs N curve of Figure 5.15.

$$Q \propto \Phi \propto E_c \quad (5.14)$$

with

$$\Phi = \int_0^{N_f} T(n) dN \quad (5.15)$$

or, approximately, the sum of the areas below the curve, neglecting phase 3, which is normally very fast.

$$\Phi = \frac{T_2 N_s}{2} + T_2 (N_f - N_s) = \text{constant} \quad (5.16)$$

where T_2 is the stabilization temperature, N_s is the number of cycles until the temperature stabilizes and N_f is the number of cycles to failure.

In practice, Φ is used as a (material property) critical value that would take a specimen to fatigue failure, and measurements of T_2 and N_s at various stress levels for a single specimen could yield the whole fatigue curve.

Figure 5.20 illustrates how the measurements process takes place, and makes the method easy to grasp.

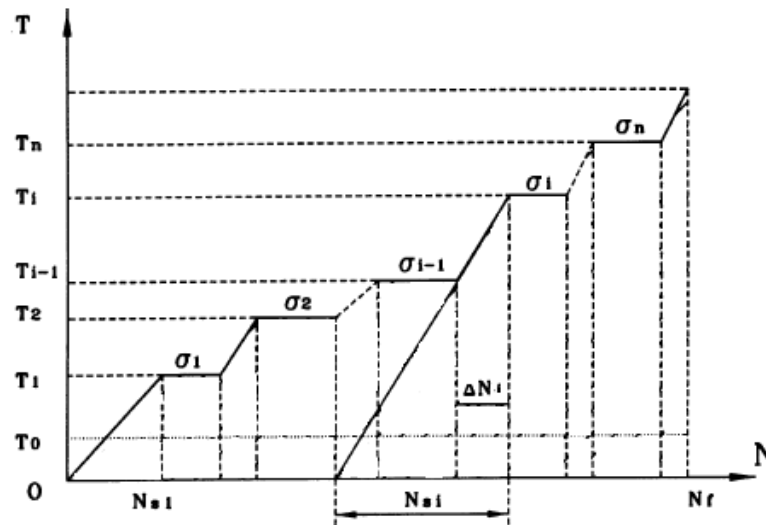


Figure 5.20: Illustration of the testing procedure for Risitano method, adapted from [69].

The specimen is loaded in a stair case mode, with various stress levels (σ_i), for each one of those a $N_{s,i}$ is measured as indicated in Figure 5.20

$$N_{s,i} = \frac{\Delta N_i T_i}{T_i - T_{i-1}} \quad (5.17)$$

where ΔN_i and T_i are the number of cycles from the start of a stress level until stabilization and the stabilization temperature for each level, respectively.

For each σ_i , with the respective T_i and $N_{s,i}$, assuming Φ has been previously measured, equation 5.16 can be used to determine $N_{f,i}$ (doing $T_2=T_i$ and $N_s=N_{s,i}$), and each pair $(N_{f,i}, \sigma_i)$ is a point in the fatigue SN curve of the material.

Theoretically, Φ could be measured within the same specimen, if it was taken to failure it would only require integrating the curve shown in Figure 5.20. In this work, the value of Φ was measured with a CR tensile specimen loaded with a constant cyclic stress level until failure, and two subsequent specimens were used to gather data points for the fatigue curve.

5.4.1

Φ Determination

In order to determine Φ , a fatigue test with constant loading range was conducted. The thermographic image obtained in the test is similar to that of Figure 5.18. The procedure follows the one described for fatigue limit calculation, the only difference being that the load was kept constant at $P_m=1637\text{N}$ and $P_a=477\text{N}$, which

results in a Goodman equivalent stress of 21.25MPa, and a measured total life (N_f) of 24250 cycles.

Figure 5.21 shows the $T(n)$ vs cycles graph obtained from the test, and the three phases described before are clearly seen.

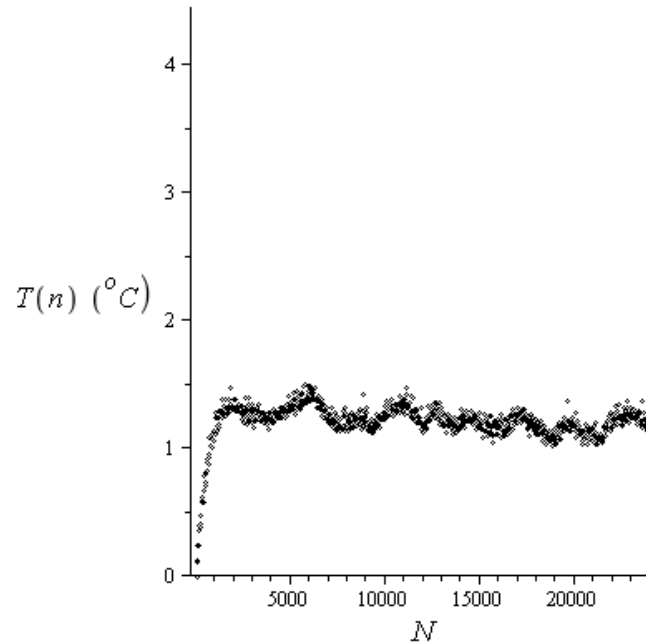


Figure 5.21: $T(n)$ vs cycles graph for Φ measurement (~ 25000 cycles = approximately 1.5h test).

The stabilization time (N_s) was determined visually as 1500 cycles, the stabilization temperature (T_2) was taken as the mean value of $T(n)$ after the first 1500 cycles which resulted in 1.23°C. Then, using equation 5.16, the value of Φ is 28905 °C cycles.

5.4.2

SN curve determination

Having determined the value of Φ , the determination of the SN curve through equations 5.16 and 5.17 requires a specimen to be cyclic loaded in a staircase mode.

Table 5.3 shows the loading conditions, the visually determined T_i 's and ΔN_i 's, as well as the resulting Goodman's equivalent stress, N_{s_i} 's and N_{f_i} 's for the first specimen, which was loaded until failure in one go.

Figure 5.22 shows the $T(n)$ vs cycles graph, the horizontal lines define the value of T_i for each stress level. The integration of all points gives a Φ value of 26560, close to the calculated before, demonstrating that the procedure could be done with a single specimen.

P_a (N)	P_m (N)	σ_a (MPa)	σ_m (MPa)	σ_{aeq} Goodman (MPa)	T_i (°C)	ΔN_i (cycles)	N_{s_i} (cycles)	N_{f_i} (cycles)
405	1161	8.51	24.39	13.62	0.59	1125	1125	49637
430.5	1310.5	9.04	27.53	15.69	0.69	975	6550	45045
451.5	1447.5	9.49	30.41	17.83	0.99	1725	5799	32245
473.5	1591.5	9.95	33.44	20.49	1.02	1125	29538	42997
498	1758	10.46	36.93	24.23	1.34	1375	5873	24556
508	1832	10.67	38.49	26.17	1.39	950	25376	33498
512	1875	10.76	39.39	27.30	1.44	1000	27207	33649
532.5	2021.5	11.19	42.47	32.28	1.76	750	4205	18573
550	2174	11.56	45.67	38.87	2.18	575	2949	14734
560.5	2276.5	11.78	47.83	44.57	2.49	500	4004	13606
567.5	2367.5	11.92	49.74	50.79	2.90	250	1787	10875

Table 5.3: Results of first specimen for SN curve determination.

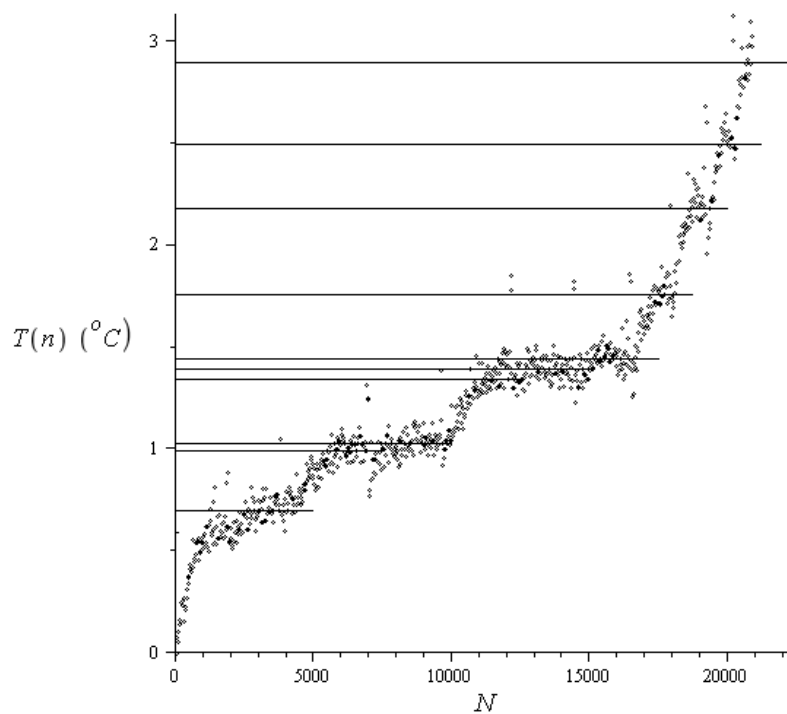


Figure 5.22: $T(n)$ vs cycles graph of first specimen for SN curve determination.

With the second specimen a different approach was used. Instead of loading the specimen until failure in one go, two loading procedures were used in two different tests, in order to study the effect of pre-existing damage on the specimen.

Table 5.4 and Figure 5.23 show the results for both tests.

The integration of all points results in a Φ value of 25430, again close to the originally calculated.

Test 1								
P_a (N)	P_m (N)	σ_a (MPa)	σ_m (MPa)	$\sigma_{a\text{ eq}}$ Goodman (MPa)	T_i (°C)	ΔN_i (cycles)	N_{S_i} (cycles)	N_{f_i} (cycles)
439.5	1364.5	9.23	28.67	16.52	0.71	1100	1100	42233
468	1547	9.83	32.50	19.67	0.95	750	2938	32512
496.5	1760.5	10.43	36.99	24.20	1.25	700	2936	25111
518.5	1922.5	10.89	40.39	28.77	1.60	750	3406	20139
534.5	2046.5	11.23	43.00	33.17	1.90	625	3965	17512
543.5	2138.5	11.42	44.93	36.98	2.08	300	3619	16052
556.5	2260.5	11.69	47.49	43.41	2.44	300	2024	13144
Test 2								
P_a (N)	P_m (N)	σ_a (MPa)	σ_m (MPa)	$\sigma_{a\text{ eq}}$ Goodman (MPa)	T_i (°C)	ΔN_i (cycles)	N_{S_i} (cycles)	N_{f_i} (cycles)
428.5	1311.5	9.00	27.55	15.63	0.73	1375	1375	41282
472.5	1594.5	9.93	33.50	20.48	1.05	625	2029	29107
503.5	1803.5	10.58	37.89	25.36	1.41	575	2246	22023
527	1987	11.07	41.75	30.95	1.74	400	2124	18027
535	2064	11.24	43.36	33.77	1.97	225	1959	15996
550	2193	11.56	46.07	39.69	2.28	150	1099	13517

Table 5.4: Results of second specimen for SN curve determination.

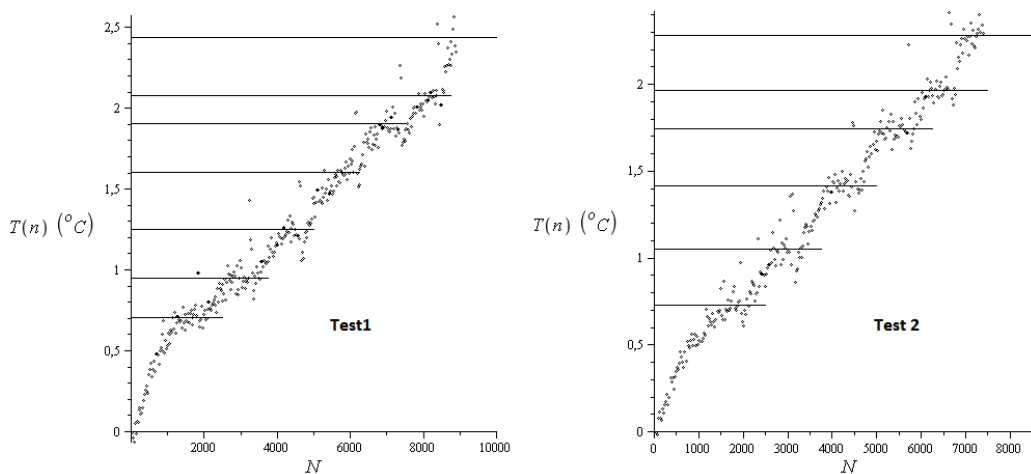


Figure 5.23: $T(n)$ vs cycles graphs of second specimen for SN curve determination.

By taking all the $(N_{f_i}, \sigma_{a\text{ eq}})$ pairs, the resulting SN graph is shown in Figure 5.24 below. The points are plotted in a log-log scale and are fitted by a parabolic relationship like equation 3.1. The resulting equation is:

$$NS^{1.316} = 1.75 * 10^6 \quad (5.18)$$

where N is the number of cycles and S is the Goodman equivalent stress.

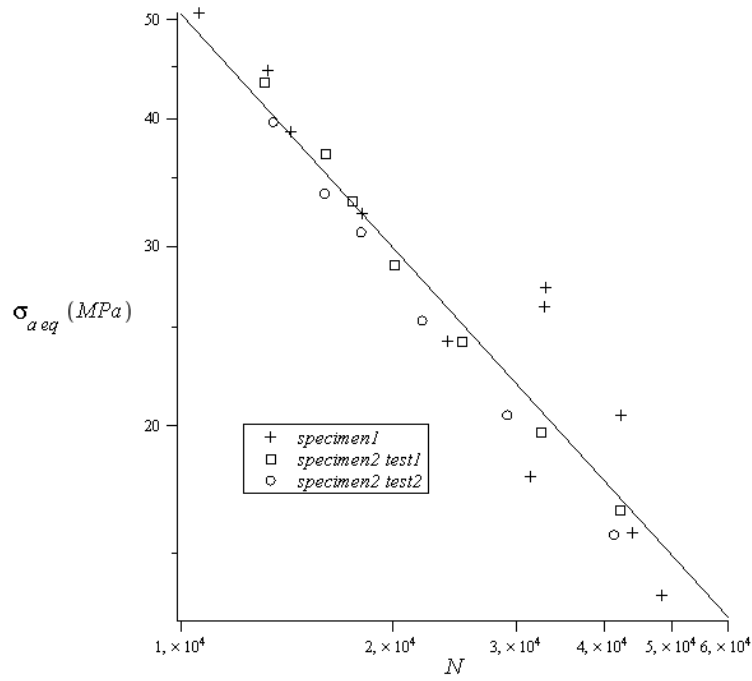


Figure 5.24: SN curve measured via thermography.

5.4.3

SN curve verification

In order to verify the validity of the obtained SN curve, traditional method points are added to the graph, as well as literature results described in Chapter 2. Figure 5.25 shows the resulting plot with all the data.

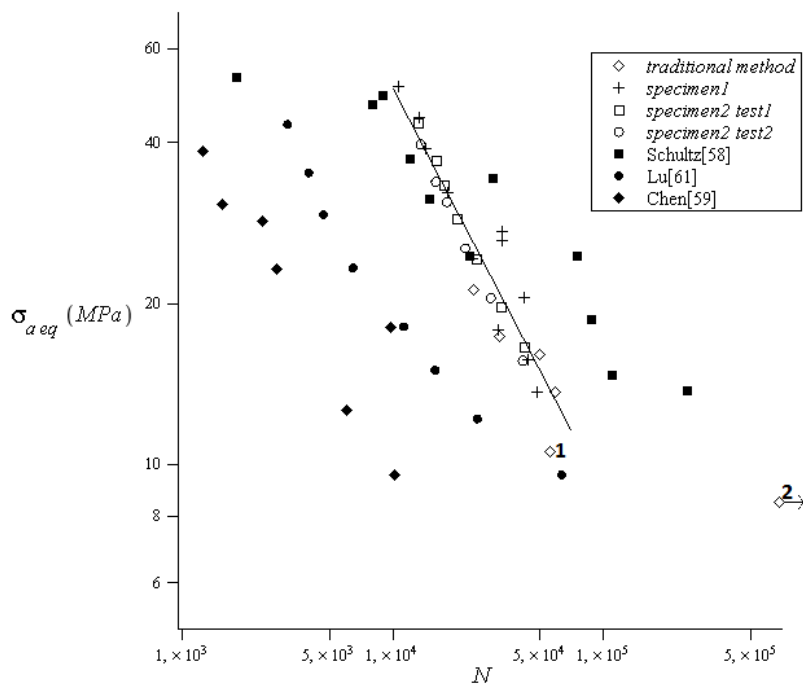


Figure 5.25: SN curve with all data points.

The traditional method points consist of 3 CR tensile specimens (21.25MPa, 10.54MPa and 9.21MPa) and 3 keyhole specimens (13.64MPa, 16.09MPa and 17.31MPa) that had cracks initiated with constant load parameters. Using Goodman's relationship to calculate the equivalent alternating stress and counting the cycles to failure (for the CR tensile specimens) or until a visible crack was detected (for the keyhole specimens), each specimen represents a single point in the graph.

The points signaled as 1 and 2 call for special explanations. Point 1 was loaded with an equivalent stress (10.54MPa) lower than what was measured as the fatigue limit, but it still broke at about 55700 cycles. Point 2 was loaded with a slightly lower equivalent stress (9.21MPa) and did not fail up to 680000 cycles. The fact that the test frequency was kept at 5Hz made going any longer than this a counter-productive choice.

The reference results, taken from literature, are shown as solid symbols on the plot. The results show decent similarity. The differences can be explained by test parameters such as load ratio, thickness, frequency and the material properties. It is very hard to compare the results effectively, since yield strength values were not reported, Chen did not report the loading frequency, Schultz had varying frequencies and the thicknesses are not equal. Nonetheless, the counterintuitive result reported by [54] and [55], about the stress ratio effect seems to be in effect here as well (See page 39).

6

Thermography Applied to Fatigue Crack Growth

This chapter is divided into two main parts concerning fatigue crack growth. The measurement of stress intensity factors (SIF's) using TSA is addressed first. Two similar algorithms, one with a linear and the other with a non-linear approach, are presented as an automatic K_I measuring technique. Then, using the non-linear algorithm, the da/dN curve is single handedly determined through TSA.

Before measuring a crack's SIF, it is necessary to find the crack and locate its tip. Appendix 2 shows a brief experiment on that, and highlights how easy it is to follow the propagating crack tip, by looking for the points with higher stresses.

6.1

Measuring Stress Intensity Factors Using TSA

Many authors have used TSA to measure SIF's, and used varied numerical and experimental approaches. Stanley and Chan [73] used the first two terms of the Westergaard's stress function to fit the thermoelastic data around cracks in mode I and II. Stanley and Dulieu-Smith [74] based their approach on the cardioid format of the isopachic fringes around a crack tip. Lesniak et al. [75] used Williams' stress field equations to fit the data using the least squares method (LSM). Lin et al. [37] approached the problem using the J-integral formulation in the data fitting process. Tomlinson et al. [35] developed a technique based on Muskhelishvili's stress field equations and a multipoint-over-deterministic method (MPODM). Díaz et al. [76] and [77] proposed a methodology for finding the crack tip position by looking at thermoelastic data, and then fitting the data using a non-linear approach in order to measure SIF's of propagating cracks. Marsavina et al. [40] used TSA to investigate crack closure during fatigue. Tomlinson and Olden [34] presented a broad review on the use of TSA in fracture mechanics and fatigue cracks.

The present work falls in line with these previous authors and attempts to develop an automated technique that can be used with a non-expensive infrared camera in combination with DeltaTherm2 software, as described in chapter 2.

6.1.1

The SIF Calculation Algorithm

Figure 6.1 shows a flowchart of the SIF calculation algorithm. The following sections describe each step.

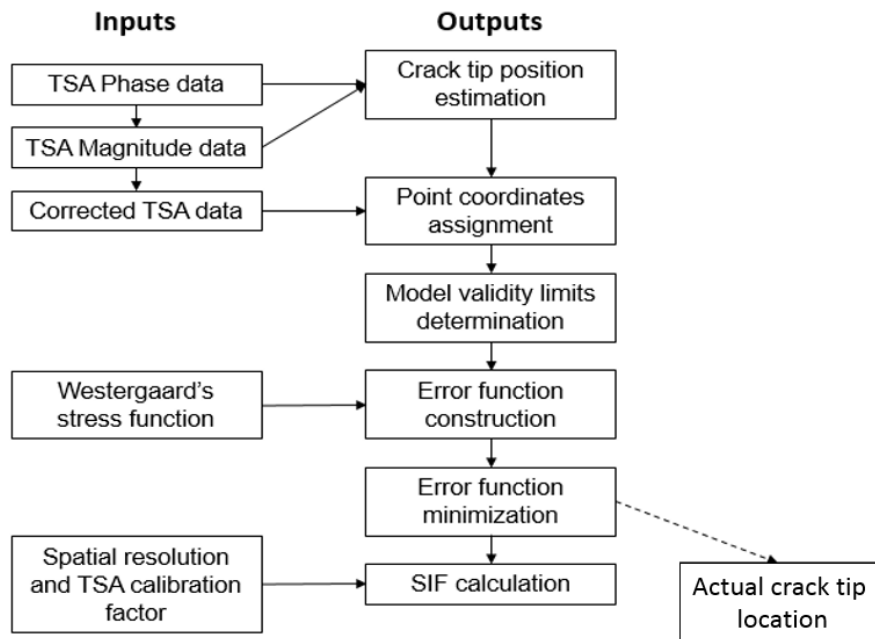


Figure 6.1: Flowchart of the SIF calculation algorithm.

6.1.2

Algorithm Inputs

The algorithm inputs are the outputs of the TSA analysis. The TSA data is usually expressed as a complex variable that has a magnitude and a phase angle. The magnitude is proportional to the temperature variation and thus, through equation 2.23, proportional to the variation of the first stress invariant. The phase angle carries the signal information, that is, if a stress is compressive or tensile.

In order to generate the phase data the TSA software uses a reference signal and determines its phase difference from the temperature measurements, that is called the lock-in process. The most usual way to do that is to use an input from the cyclic loading machine as the reference, but as stated before, the software used in the present work does it differently. DeltaTherm2 uses the temperature of a selected area of the specimen's surface as the reference.

Then, with the TSA magnitude and phase data, it is possible to generate a corrected TSA data⁸,

$$S = \begin{cases} Mag & \text{if } |phase| < 45^\circ \\ -Mag & \text{if } |phase| > 45^\circ \end{cases} \quad (6.1)$$

where S is the corrected TSA data, Mag is the magnitude data value in "camera units", $|phase|$ is the absolute value of the phase angle, in degrees.

⁸ This function makes the phase data a binary variable, a point is either in phase or out of phase with the reference.

Other input needed is the mathematical model used. In this case, a Westergaard's stress function (We) was used to describe the stress field around the crack tip [67],

$$We(x, y) = \sigma_1 + \sigma_2 = 2[Re(Z) + Re(Y)] \quad (6.2)$$

with,

$$Z = \sum_{n=0}^N [A_n z^{n-0.5}] \quad (6.3)$$

$$Y = \sum_{m=0}^M [B_m z^m]$$

where N and M determine the number of coefficients to be used, A_n and B_m are the data fitting coefficients and z is the complex variable of the point coordinates

$$z = (x - x_o) + i(y - y_o) \quad (6.4)$$

being x and y the horizontal and vertical coordinates of a point (placing the origin at the estimated crack tip location and the x axis along the crack propagation direction). $i = \sqrt{-1}$, and x_o and y_o the horizontal and vertical errors of the estimated crack tip location, which are solved for only when applying the non-linear method; for the linear method they are set to 0.

The last inputs needed are the spatial resolution (SR) and the TSA calibration factor (A). The spatial resolution is simply determined via a known dimension in the specimen,

$$SR = W/p \quad (6.5)$$

where SR is the spatial resolution in mm/pixel, W is a known dimension of the specimen in mm (e.g. width) and p is the number of pixels the dimension measures on the thermographic image. The TSA calibration process is discussed in chapter 2 and the experiment presented in chapter 5.

6.1.3

Crack Tip Position Estimation and Point Coordinates Assignment

This work uses an specially improved and automated version of the methodology proposed in [76] to estimate the position of the crack tip.

Firstly, the image needs to be positioned so that the crack is horizontal. Then, using the TSA magnitude map, the vertical position of the crack tip (Y_o') is

estimated by plotting y vs $1/S^2$ curves for each vertical line in the image (perpendicular to the crack). The resulting graphs, for the lines ahead of the crack tip, have a clear minimum value. The mean value of y where this minimum value occurs for all the vertical lines is equal to Y_o' . Figure 6.2a shows the magnitude map around a crack, while Figure 6.2b shows a typical y vs $1/S^2$ plot.

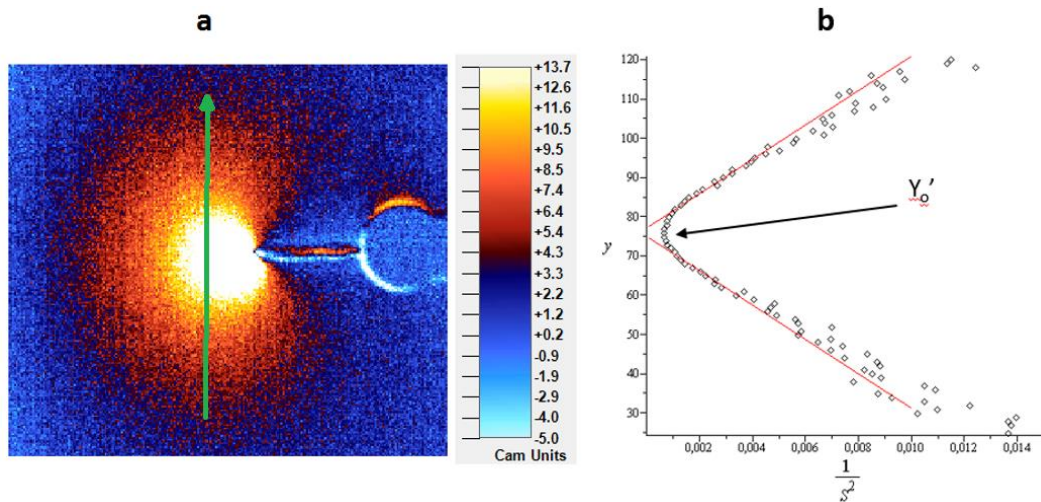


Figure 6.2: a) The magnitude map around a crack and b) Typical y vs $1/S^2$ plot.

The horizontal position of the crack tip (X_o') is estimated through what is called the phase shift. Due to the plasticity near the crack tip, the adiabatic conditions required by TSA are lost. This can be seen as an abrupt change in phase angle right in front of the crack tip. In the horizontal phase vs x curve at Y_o' , the position where this abrupt change occurs is equal to X_o' . Figure 6.3a shows the phase map around a crack and Figure 6.3b shows a typical phase vs x plot.

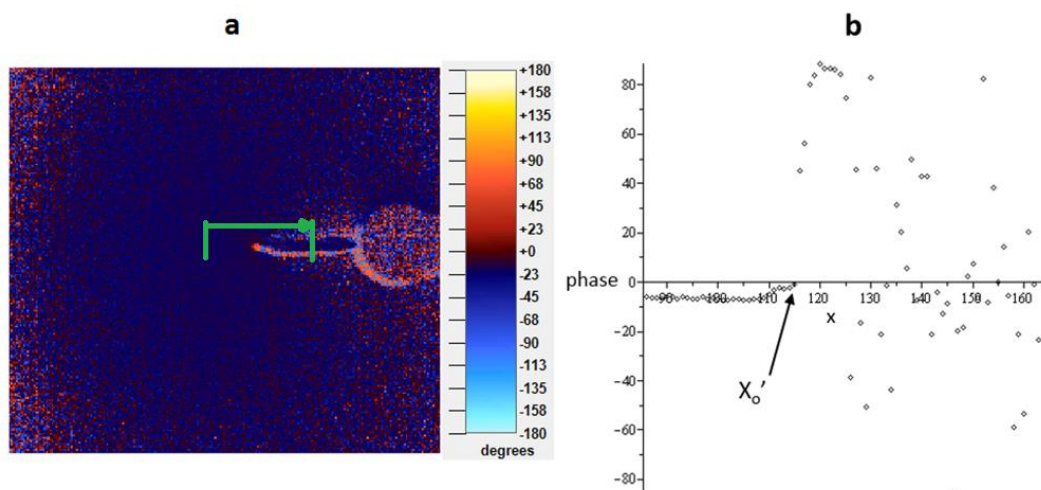


Figure 6.3: a) The phase map around a crack and b) Typical phase vs x plot.

Having the values of X_o' and Y_o' , the coordinates assignment step is simple, each point of the image gets assigned to an x and a y value, which are the horizontal and vertical distances from the estimated crack tip, respectively.

6.1.4

Model Validity Limits Verification

The points used for the data fitting process must be in accordance with the mathematical model. In [77], the authors concluded that the model predicts a linear behavior of $1/S^2$ with respect to the distance from the crack tip. They proposed that only the points of Figure 6.2b that presented a linear behavior should be used in the data fitting process.

The methodology used in the present work uses the same argument, but instead of using the vertical line plots, it uses plots of $1/S^2$ vs r , where r is the radial distance from the estimated crack tip. With r and θ , the polar coordinates centered at X_o' and Y_o' , and $\theta=0$ for the horizontal line ahead of the crack, $1/S^2$ vs r curves are plotted for each 1 degree increment of θ between -120° and $+120^\circ$. Figure 6.4a shows the radial direction from where the curves are plotted and Figure 6.4b shows an example of one of these plots.

The loss of linearity near the crack tip is explained by non-adiabatic conditions that interfere with the TSA results. For the region far away from the crack tip, two possible explanations exist, or a combination of both. The higher noise in TSA data due to smaller stresses and consequent smaller temperature variation, and the complexity of the actual stress field far from the crack that requires not only the SIF term, but also more terms of the stress function to be accurately predicted. Reasonable values of N and M are from 0 to about 6 (2-14 terms).

For each of the $1/S^2$ vs r plots, r_{min} , r_{max} values are determined using two margins of tolerance of non-linearity that are manually adjusted to fit the data. The author supposes that the r_{min} margin should be related to the loading level and that the r_{max} margin could be related to the overall noise levels of the data. No attempts were made to automate the optimization process of these margins.

The values R_{min} (and R_{max}), below (and above) which no data points are collected, are defined as the mean value of all the r_{min} (and r_{max}).

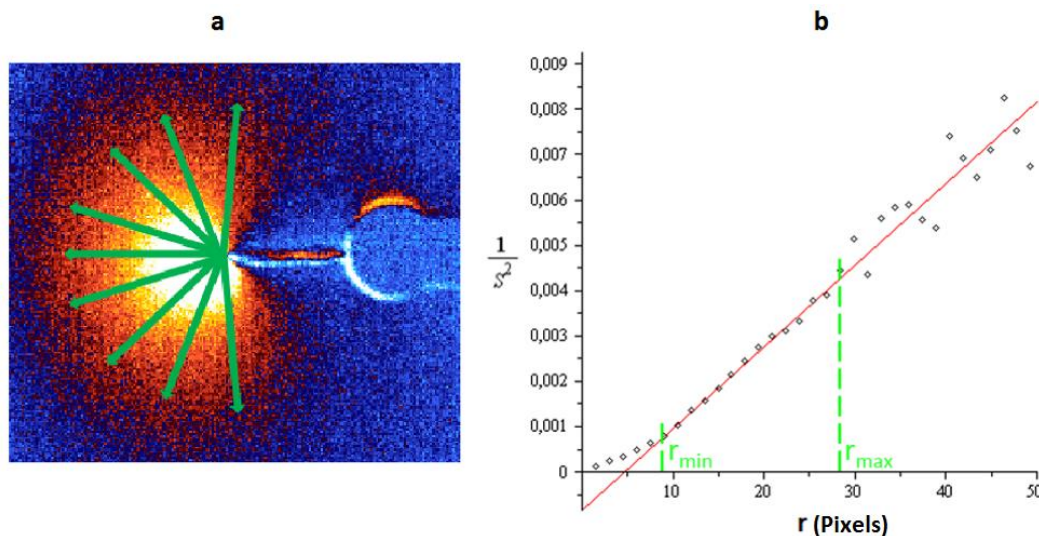


Figure 6.4: a) The radial direction where the curves are plotted and b) Typical $1/S^2$ vs r plot

6.1.5

Error Function Construction and Minimization

After determining which data points can be fitted by the model, an error function (e) is constructed:

$$e = \sum_{\text{Data points}} [S - We(x, y)]^2 \quad (6.6)$$

where e is the error function to be minimized, S is the TSA signal of the point and $We(x, y)$ is defined by equation 6.2.

The minimization process uses, for the linear approach, a LSM algorithm (identical to the one described in chapter 5, during K_i calculation) and, for the non-linear approach, a Downhill Simplex method (Nelder-Mead) [78].

The Nelder-Mead method can be understood geometrically and following Figure 6.5a (for $x \in \mathbb{R}^2$) and the procedure below, Figure 6.5b shows a detailed step-by-step explanation of the first panel in Figure 6.5a.

- 1- In order to minimize the function $f(x)$ where $x \in \mathbb{R}^n$ are the current test points x_1, x_2, \dots, x_{n+1} , and should be ordered so that $f(x_1) \leq f(x_2) \leq \dots \leq f(x_{n+1})$, being x_1 the best point so far and $f(x_{n+1})$ the worst.
- 2- Calculate the centroid x_o of all points except x_{n+1} .
- 3- Compute the reflected point as $x_r = x_o + (x_o - x_{n+1})$
If $f(x_1) \leq f(x_r) \leq f(x_n)$ then replace x_{n+1} with x_r and return to step 1.
Else go to step 4.
- 4- If $f(x_r) < f(x_1)$ then compute the expanded point as $x_e = x_r + (x_r - x_o)$
If $f(x_e) < f(x_r)$ then replace x_{n+1} with x_e and return to step 1.
Else replace x_{n+1} with x_r and return to step 1.

Else go to step 5.

- 5- Compute the two contracted points $x_{c1,c2} = x_0 \pm 0.5(x_{n+1} - x_0)$
 Choose the smallest between x_{c1} and x_{c2} as x_c
 If $f(x_c) < f(x_{n+1})$ then replace x_{n+1} with x_c and return to step 1.
 Else go to step 6.
- 6- Replace all points except x_1 with $x_i = x_1 + 0.5(x_i - x_1)$ and go to step 1.

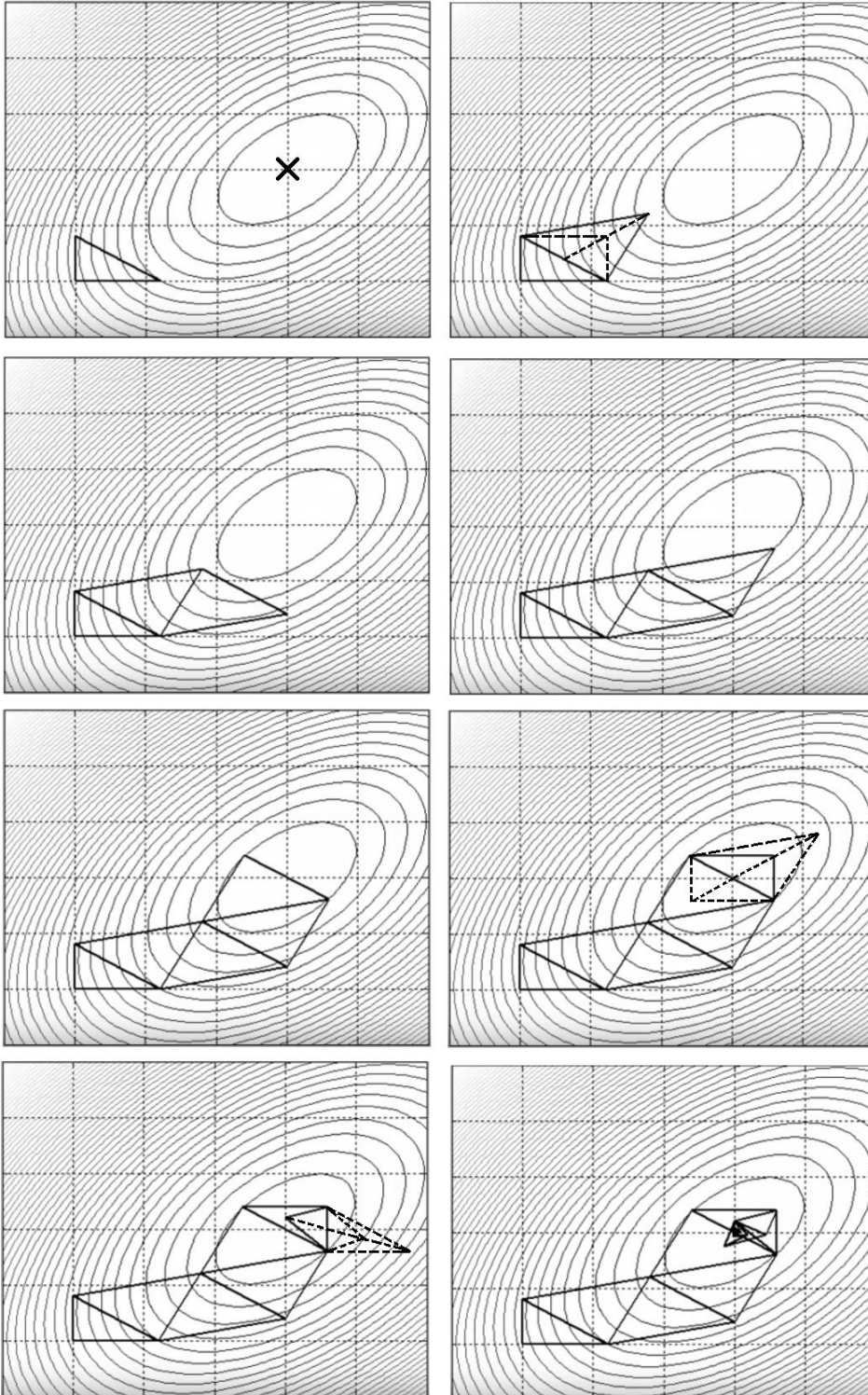
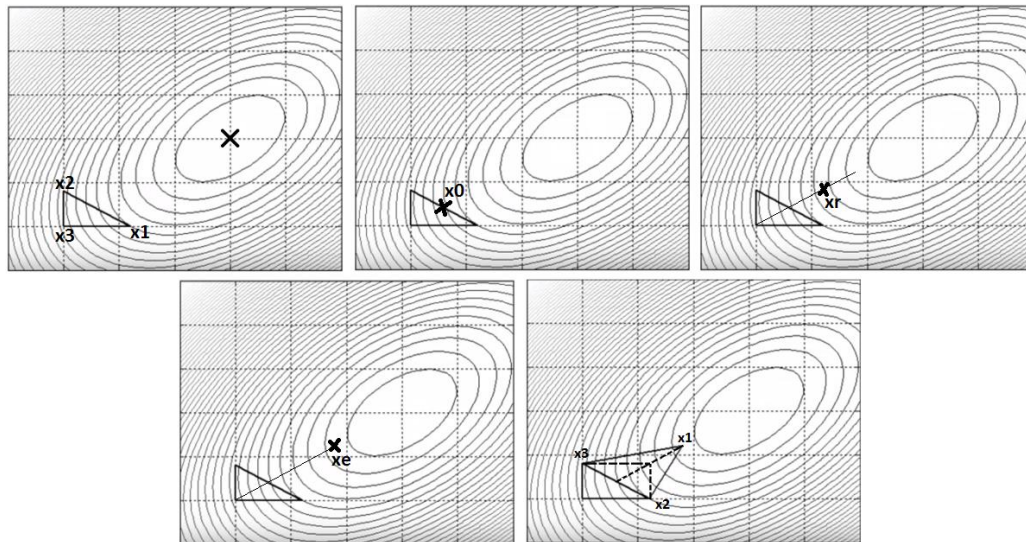


Figure 6.5: a) Illustration of Nelder-mead method for $x \in \mathbb{R}^2$.



b) step-by-step explanation of first panel.

In Figure 6.5a, the first panel shows the target minimum at the big X and the three initial points. The second panel originates after a reflection + expansion operation. The third panel after a reflection. The fourth after another reflection. The fifth after a third reflection. The sixth panel originates from a reflection + contraction operation, where $f(x_{c1}) < f(x_{c2})$. The seventh panel shows a reflection + contraction operation where $f(x_{c2}) < f(x_{c1})$. Finally, the eighth panel shows the result after a series of many operations, all three points tend to minimum.

In Figure 6.5b, the first panel shows the target minimum at the big X and the three initial points numbered from best to worst. The second panel shows the centroid x_o of the best 2 points. The third panel shows the reflected point x_r calculated using the line between the worst point and x_o . Since x_r is better than the 3 initial points, the expanded point x_e is calculated in the fourth panel, again, using the line between the worst initial point and x_o . Since x_e is better than x_r , it is now chosen as the new point, show in the fifth panel, numbered.

This algorithm is quite powerful and robust, since it does not require derivation of the error function. Nonetheless, it searches for local minimums, so the initial points will have a unneglectable influence on the result for the minimization of more complicated functions.

6.1.6

SIF Calculation and Actual Crack Tip Location

After having all the coefficients calculated, the SIF can be calculated as

$$\Delta K_I = A_0 A \sqrt{2\pi SR} \quad (6.7)$$

where ΔK_I is the mode I SIF range in $\text{MPa}\sqrt{\text{m}}$, A_0 is the first coefficient as described in equation 6.2, A is the TSA calibration factor and SR is the spatial resolution.

In the non-linear approach, the values of x_0 and y_0 , as seen in equation 6.4, are determined as well and the real location of the crack tip can be determined

$$\begin{aligned} X_0 &= X'_0 - x_0 \\ Y_0 &= Y'_0 - y_0 \end{aligned} \quad (6.8)$$

where X_0 and Y_0 give the calculated actual position of the crack tip.

6.2

Algorithm verification and Use

6.2.1

Numerically Generated TSA Data

Firstly, the algorithm is tested using an emulation of TSA data. Figure 6.6a shows the numerically generated data and Figure 6.6b shows the fitted model for the crack tip estimation at $(-3,0)$ relatively to the actual position.

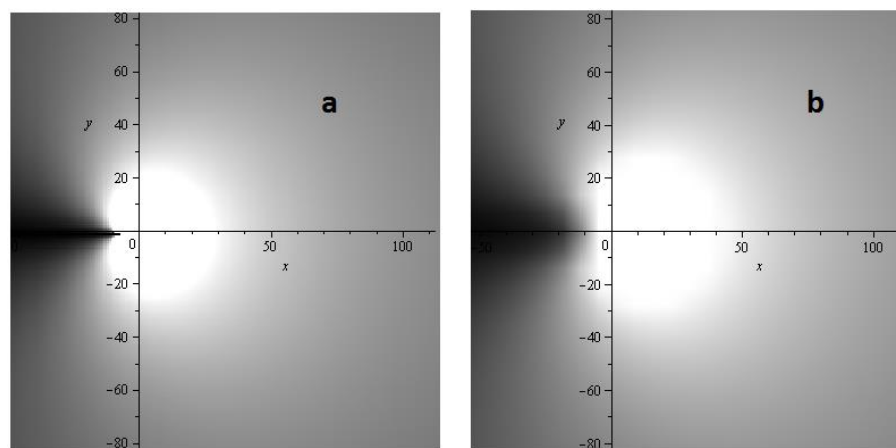


Figure 6.6: a) Numerically generated TSA data for crack tip at $(-3,-1)$ and b) Calculated model for estimated crack tip at $(-3,0)$.

For the linear approach, where the crack tip location is not determined, the final result of ΔK_I was heavily dependent on the crack tip horizontal position estimation (X'_0), presenting errors of 10% for just 1 pixel inaccuracy in the estimation. For the vertical direction, the dependence was much smaller, a 1 pixel inaccuracy in Y'_0 resulted in an error of 0.4% for ΔK_I .

The non-linear approach, on the other hand gave on-point results for ΔK_I even for crack-tip initial estimation coordinate (X'_0 and Y'_0) errors of 20+ pixels in the horizontal and vertical directions.

6.2.2

SIF Measurements

After this validation of the methodology, the algorithm was put to test on several crack lengths (a) for the specimen shown in Figure 6.2a, Figure 6.3a and Figure 6.4a.

The analyses were made using $N=M=3$, as described in equation 6.3, and 800 data points uniformly spaced between the R_{\min} and R_{\max} limiting circles. Figure 6.7 shows the selected data points for the specimen with a 14.1mm crack.

Table 6.1 shows the results for both the linear and non-linear approaches, as well as for results determined with Digital Image Correlation (DIC) technique, as developed by [79], and finite elements method (FEM) for the ΔK_I as shown in Appendix 5. Figure 6.8 shows the $\Delta K_I/\Delta P$ vs a plot. Caution was taken in order to guarantee that the crack was completely opened, using high enough loads.

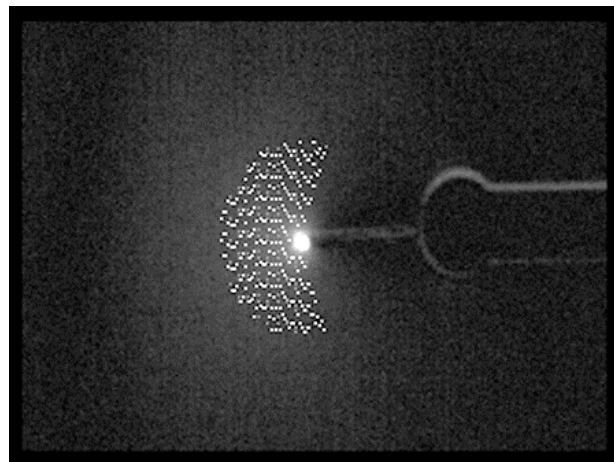


Figure 6.7: Selected data points for SIF calculation of a 14.1mm crack.

a (mm)	ΔP (N)	$\Delta K_I/\Delta P$	$\Delta K_I/\Delta P$	$\Delta K_I/\Delta P$	$\Delta K_I/\Delta P$
		TSA Linear (10^{-3} MPa/N \sqrt{m})	TSA Non-linear (10^{-3} MPa/N \sqrt{m})	DIC (10^{-3} MPa/N \sqrt{m})	FEM (10^{-3} MPa/N \sqrt{m})
4.7	194	5.98	5.46	5.93	4.99
7.4	196	6.63	6.22	6.71	5.55
10	175	7.02	6.51	7.30	6.10
11.9	161	7.76	7.14	7.57	6.66
14.1	153	9.15	8.04	8.81	7.59
15.9	150	9.80	8.80	9.25	8.64
18.4	145	11.72	10.76	10.96	10.67
20.7	137	14.38	13.43	13.40	13.28

Table 6.1: Results for the SIF measurement using TSA, DIC and FEM.

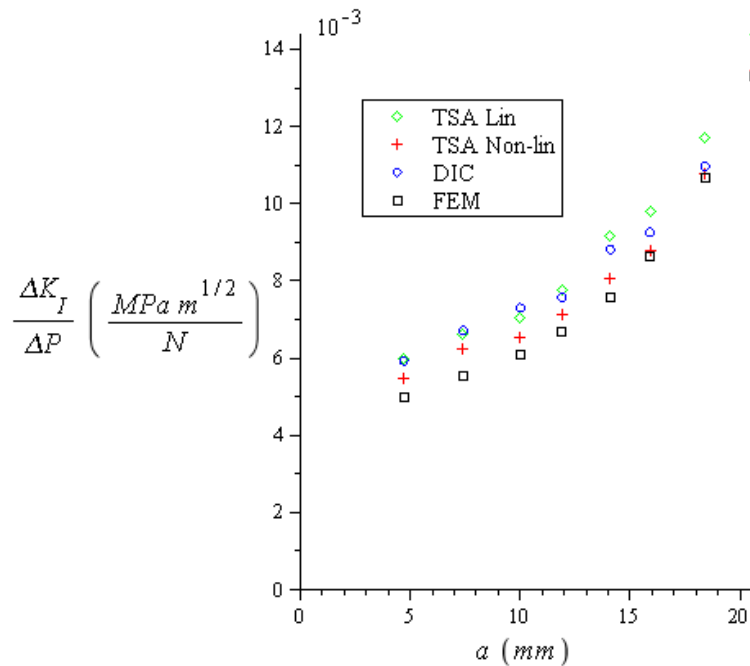


Figure 6.8: $\Delta K_I / \Delta P$ vs a plot for all experimental techniques and FEM

It is clear that for bigger cracks, where the stresses around the crack tip are higher and the experimental data is less noisy, both TSA Non-linear and DIC techniques result in values of ΔK_I closer to the expected value, calculated by FEM. The TSA Linear approach tends to give higher results and errors, since the crack-tip position estimation error is not accounted for.

6.3

Measuring the Crack Growth Rate

The SIF range (ΔK_I), as explained in chapter 3, controls the crack growth rate (da/dN). In order to measure the crack growth rate two approaches are presented. One using the non-linear TSA SIF range measurement algorithm shown in the last sections, and the other through straight temperature measurement.

6.3.1

Crack Tip Accuracy of the Algorithm

A crack was propagated through a keyhole specimen and 5 photos were taken with a regular camera, in order to locate the crack tip and measure the crack length, while, simultaneously, collecting TSA data.

The crack tip position was visually determined in the pictures, then converted to length (mm) using the spatial resolution of the camera, that was determined using the known dimension of the section ahead of the crack (60.5mm)

and its size in pixels in each picture. The non-linear algorithm was used to locate the position in pixels, that was converted to length (mm) using the spatial resolution of the infrared camera, determined in the same way.

The results are shown in Table 6.2 while Figure 6.9 shows the determined (red) and measured (green) positions of the crack tip. The pixel values are measured relative to the opposite border.

Measured Crack Length (mm)	Measured Crack Tip position (infrared Pixel)	Algorithm Crack Tip Position (infrared Pixel)	Algorithm Crack Length (mm)	Error (mm)
4.5	261	265	3.7	0.7
8.3	268	273	7.3	1.0
11.1	278	281	10.5	0.6
13.0	292	293	12.8	0.2
14.4	311	313	14.0	0.4

Table 6.2: Results for crack tip position and crack length.

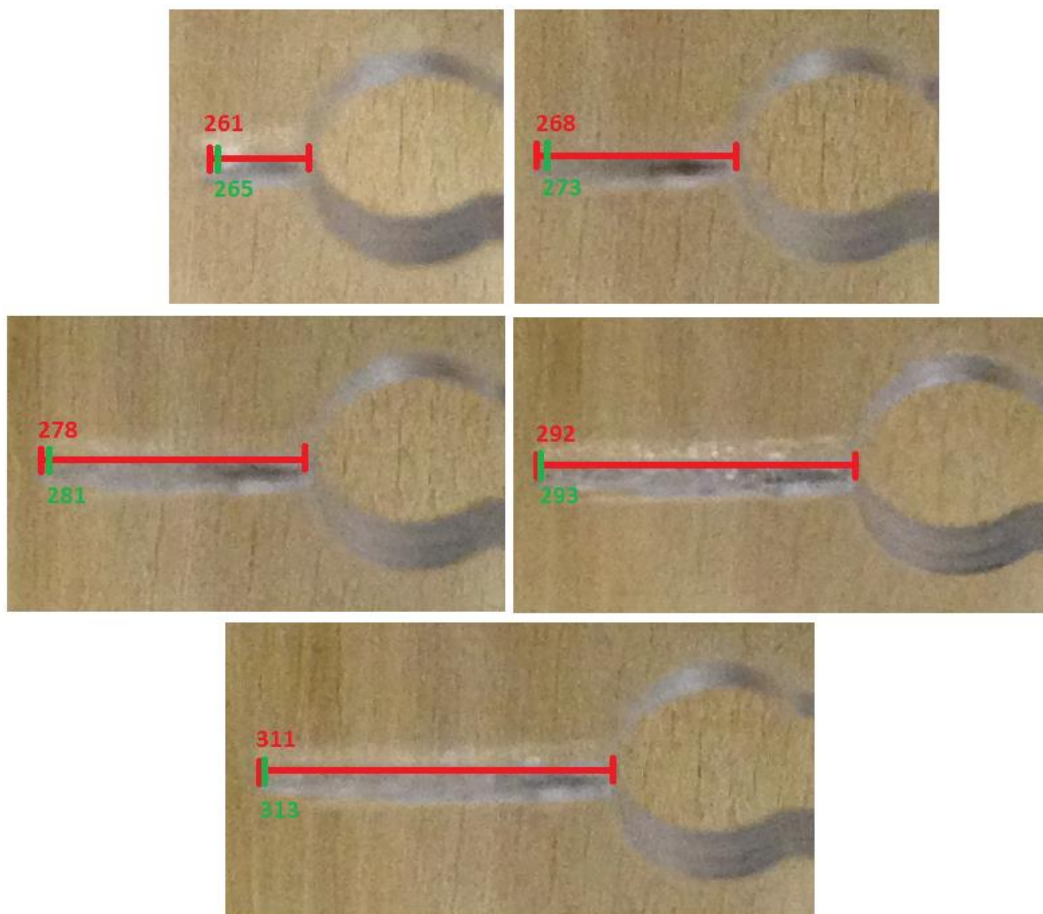


Figure 6.9: Determined by TSA (red) and measured with photos (green) cracks.

The results show that the algorithm can find the crack tip location with an accuracy of about 1mm for smaller cracks, and that this error tends to diminish for longer cracks⁹. Such decent measurements and knowledge of the number of cycles between each crack length result makes da/dN values determination possible, which could be plotted and fitted by Paris' law.

6.3.2

da/dN Straight from Temperature Rise

The other approach to determine the crack growth rate involves measuring the temperature in a way similar to what was done in chapter 5. That is, measuring the temperature around the propagating crack and of a reference specimen, simultaneously, and computing the difference between them (ΔT).

This method was discovered during an experiment that meant to investigate crack propagation through a damage parameter like Φ (the Risitano's material property) as described in chapter 5.

During the propagation of another crack, the infrared camera made a video by capturing 1 frame for each 4 seconds period. The resulting video shows the crack propagating and the maximum ΔT rising, as expected. Since the load range was kept constant, the stresses got higher with the increase in crack length, which then causes a rise in temperature.

After the video was recorded, 11 points where the crack tip eventually passed through were selected, Figure 6.10 shows these points before and after the crack propagation.

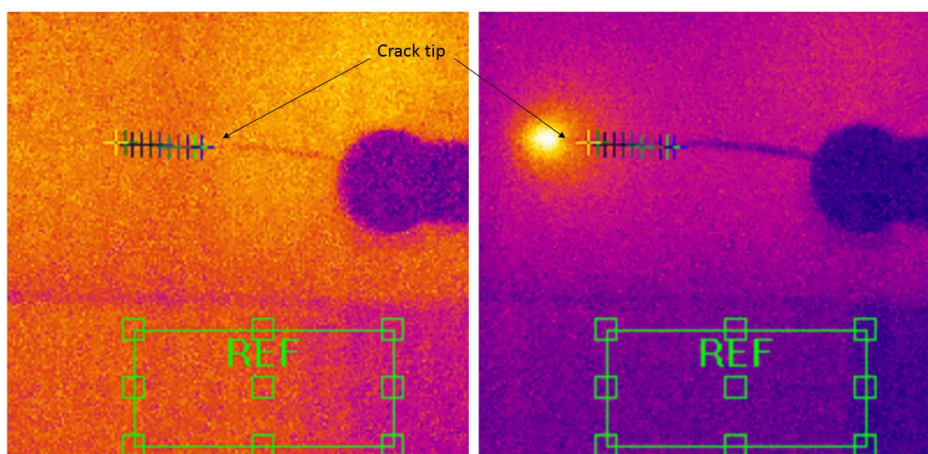


Figure 6.10: Position of 11 points along the crack path.

⁹ The crack propagation front is not a straight line, it usually assumes a parabolic format. Photos of the cracks and fractures are show in Appendix 6.

The ΔT vs N (cycles) plot for each one of these points is shown in one graph in Figure 6.11a. Points 3, 6 and 10 are plotted separately in Figure 6.11b showing the integration area.

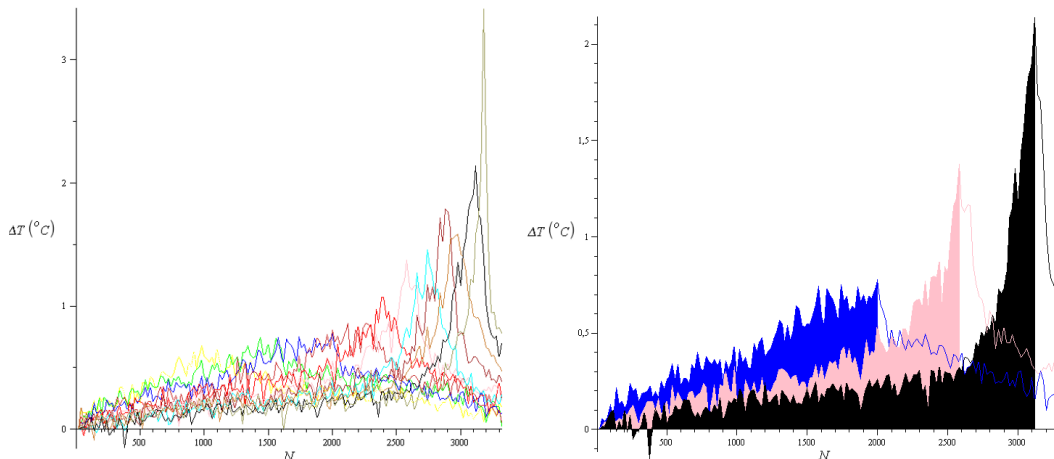


Figure 6.11: ΔT vs N plot for 11 points along crack path (left) and integration areas for curves 3, 6 and 10 (right).

By integrating each one of these curves, from the start until they reach their maximum values, the resulting Φ value obtained for each point is given in Table 6.3. as show in Figure 6.11b.

Point	1	2	3	4	5	6	7	8	9	10	11
Φ	322.9	533.3	794.8	738.9	837.9	808.4	747.0	933.2	888.9	862.0	843.6

Table 6.3: Damage parameter result for 11 points along crack path.

Excluding the first 2 points, which were already pretty close to the crack tip when the recording started, all the others show a Φ value close to 800. This would imply that when a point reaches this value the crack has reached it thus representing the failure of that point.

This finding rose the question about a possible relationship between ΔT and the crack growth rate. Since both had the same recursive argument, i.e. the bigger the crack gets the higher the stresses which makes the ΔT and the SIF get higher, in return the crack propagates faster, which makes the whole process have the same snowball effect.

Figure 6.12 shows the comparison between measured da/dN vs N graph (using the same camera used in last section to visually locate the crack tip) and the $\Delta T_{\max}/\Delta P$ vs N curve, where ΔT_{\max} is taken at the point of highest temperature at each instant and ΔP is the constant load range during propagation (170N).

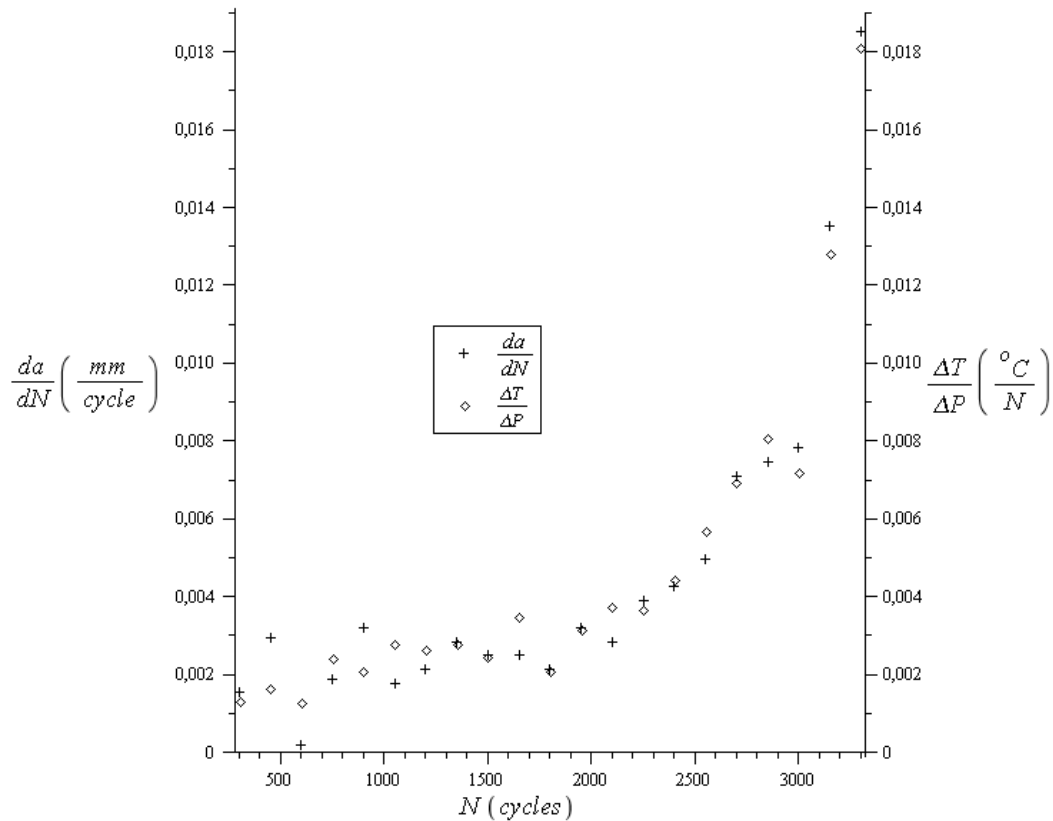


Figure 6.12: Comparison between $\Delta T/\Delta P$ and da/dN .

The conclusion is that da/dN measurements can be made through straight temperature measurements, as well as through the use of the TSA ΔK_I algorithm, but unfortunately, because a different software is used for each approach (FLIR camera software and DeltaTherm2 respectively) they cannot be tested simultaneously.

The next section uses these da/dN measurements, combined with ΔK_I evaluations (experimental and predicted) to create da/dN vs ΔK_I plots fittable by the Paris law.

6.4

Measuring da/dN vs ΔK_I Curves

Two experiments were conducted using the TSA ΔK_I algorithm and one experiment using the temperature measurement (in conjunction with the ΔK_I calculation from the formulas obtained in Appendix 5).

Table 6.4 shows the data from the first test:

N (cycles)	P _{max} (N)	P _{min} (N)	a camera (mm)	da/dN camera (mm/cycle)	a TSA algorithm (mm)	da/dN TSA algorithm (mm/cycle)	ΔK _I TSA (MPa√m)
0	326	100	4.17		4.15		1.120
150	326	100	4.33	0.001053	4.29	0.000933	1.071
300	326	100	4.50	0.001163	4.44	0.001000	1.080
450	326	100	4.66	0.001056	4.68	0.001600	1.074
600	326	100	4.88	0.001485	4.88	0.001333	1.112
750	326	100	5.12	0.001608	5.12	0.001600	1.133
900	326	100	5.34	0.001427	5.28	0.001067	1.181
1200	321	100	5.59	0.001192	5.69	0.001957	1.167
1350	321	100	5.84	0.001692	6.00	0.002067	1.203
1500	321	100	6.17	0.002152	6.25	0.001667	1.243
1650	321	100	6.44	0.001865	6.41	0.001067	1.280
1800	321	100	6.78	0.002231	6.73	0.002133	1.308
1950	321	100	7.10	0.002110	7.05	0.002133	1.312
2250	321	103	7.55	0.002656	7.46	0.002417	1.379
2400	321	103	7.99	0.002963	7.79	0.002200	1.424
2550	321	103	8.43	0.002891	8.12	0.002200	1.455
2700	321	103	8.92	0.003262	8.62	0.003333	1.553
2850	321	103	9.41	0.003329	9.12	0.003333	1.565
3000	321	103	9.95	0.003571	9.82	0.004667	1.622
3150	321	103	10.67	0.004784	10.5	0.004533	1.748

Table 6.4: Results for the first crack propagation da/dN test.

The resulting da/dN graphs are plotted using a log-log scale in Figure 6.13, the resulting fitted Paris' equations are also show.

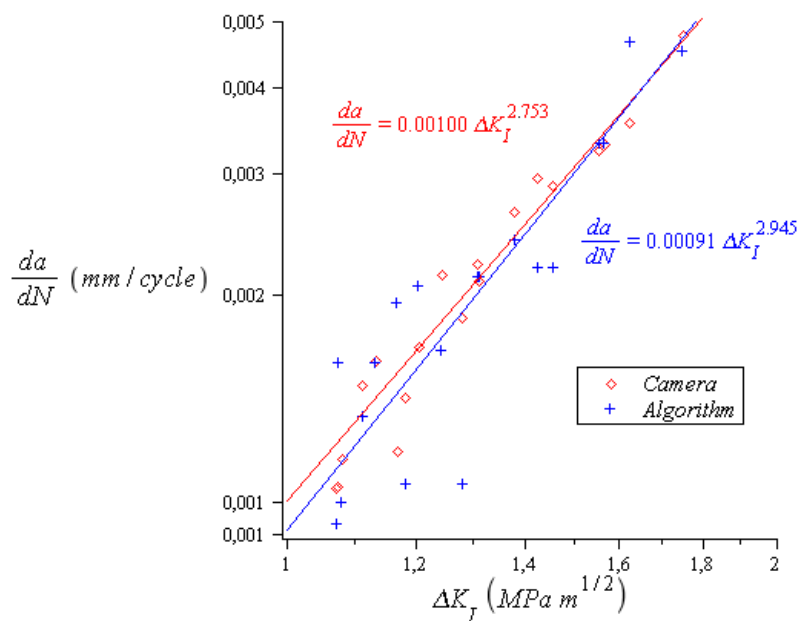


Figure 6.13: da/dN (photos and TSA algorithm) vs ΔK_I (TSA algorithm) plot for first experiment.

They show good agreement, showing that TSA can single-handedly measure a da/dN curve.

The second experiment compared the results obtained by the TSA algorithm and FEM for the ΔK_I while the da/dN was measured using the camera method. Again, the data is listed in Table 6.5.

The objective this time was to investigate if crack closure was affecting the measurement. In order to do that, the minimum load (and the maximum load, for reasons described in chapter 4) was lowered. Doing this permits the crack to close, and should make the effective ΔK different from the one predicted by FEM.

Figure 6.14 shows the da/dN vs ΔK_I plots for the TSA algorithm and FEM results. If left untouched (ΔK_I TSA 1), the algorithm finds values of ΔK_I systematically lower than the ones predicted by FEM. On the other hand, if special care is taken so that the algorithm uses only data far enough (twice the value of R_{min}) from the crack tip (ΔK_I TSA 2), the results are almost identical.

N (cycles)	P_{max} (N)	P_{min} (N)	a (mm)	da/dN (mm/cycle)	ΔK_I TSA1 (MPa \sqrt{m})	ΔK_I FEM (MPa \sqrt{m})	ΔK_I TSA2 (MPa \sqrt{m})
15051	223	61	10.4	0.000302	0.940	1.004	1.05
20211	221	62	12.5	0.000407	1.030	1.093	1.165
24930	222	65	14.5	0.000424	1.110	1.224	1.268
28798	222	63	16.6	0.000603	1.260	1.416	1.421
30695	223	58	18.6	0.001054	1.364	1.652	1.679
31907	222	58	20.6	0.00165	1.678	1.959	1.958
32464	223	63	22.6	0.003591	1.881	2.353	2.384
32830	218	65	24.6	0.005464	2.068	2.813	2.783
32980	216	60	26.6	0.013333	2.790	3.435	3.522

Table 6.5: Results for the second crack propagation da/dN test.

These results suggest that the TSA algorithm is actually measuring the effective SIF. Since the values found were lower than the predicted ones, part of the applied load is supposedly being used to open the crack. Nonetheless, taking data points far from the crack tip seem to nullify this effect.

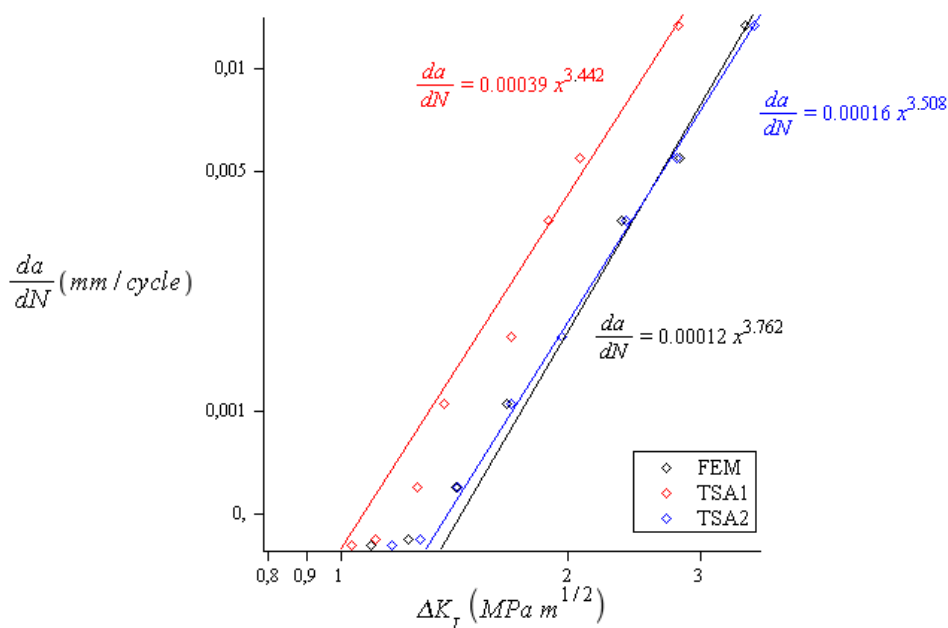


Figure 6.14: da/dN (TSA algorithm) vs ΔK_I (TSA algorithm and FEA) plot for second experiment.

The third, and last, experiment used the temperature measurement method to determine the crack growth rate. The crack size was calculated from the da/dN and the ΔK_I values obtained using the FEM formula obtained in Appendix 5.

Table 6.6 shows the data for the experiment while Figure 6.15 shows the resulting da/dN plots.

N (cycles)	a camera (mm)	da/dN camera (mm/cycle)	ΔK_I FEM (MPa \sqrt{m})	da/dN Temperature (mm/cycle)
0	12.54		1.172	
300	12.77	0.00077	1.188	0.00130
450	13.22	0.00295	1.219	0.00165
600	13.24	0.00020	1.222	0.00128
750	13.53	0.00189	1.243	0.00240
900	14.01	0.00319	1.282	0.00209
1050	14.27	0.00177	1.305	0.00278
1200	14.59	0.00213	1.334	0.00264
1350	15.02	0.00283	1.375	0.00277
1500	15.39	0.00248	1.413	0.00244
1650	15.76	0.00248	1.454	0.00347
1800	16.08	0.00213	1.490	0.00208
1950	16.56	0.00319	1.548	0.00312
2100	16.98	0.00284	1.604	0.00374
2250	17.57	0.00390	1.686	0.00366
2400	18.21	0.00426	1.784	0.00443
2550	18.96	0.00497	1.909	0.00568
2700	20.02	0.00711	2.112	0.00692

Table 6.6: Results for the third crack propagation da/dN test.

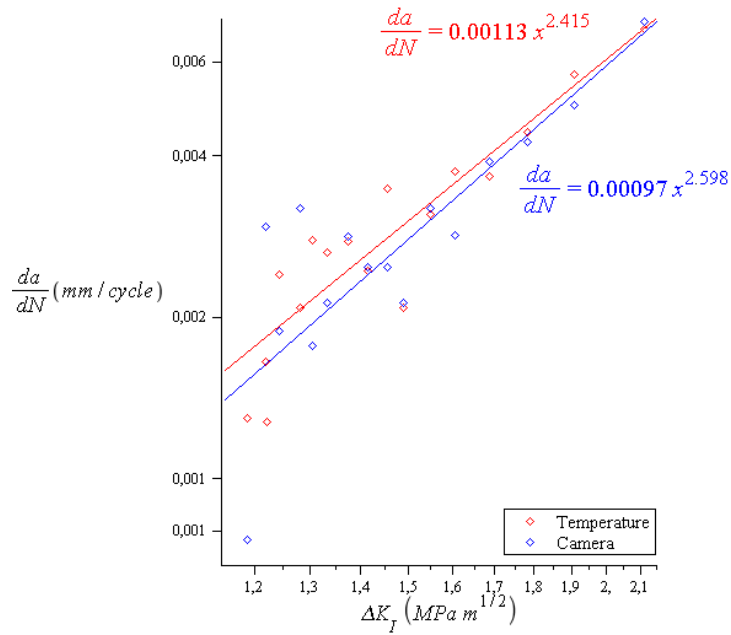


Figure 6.15: da/dN (temperature and photos) vs ΔK_I (FEA) plot for third experiment.

Again, the results show good agreement, proving the validity of both methods for measuring the crack growth rate.

Finally, all results are plotted, together with reference results described in chapter 3, in one single graph in Figure 6.16.

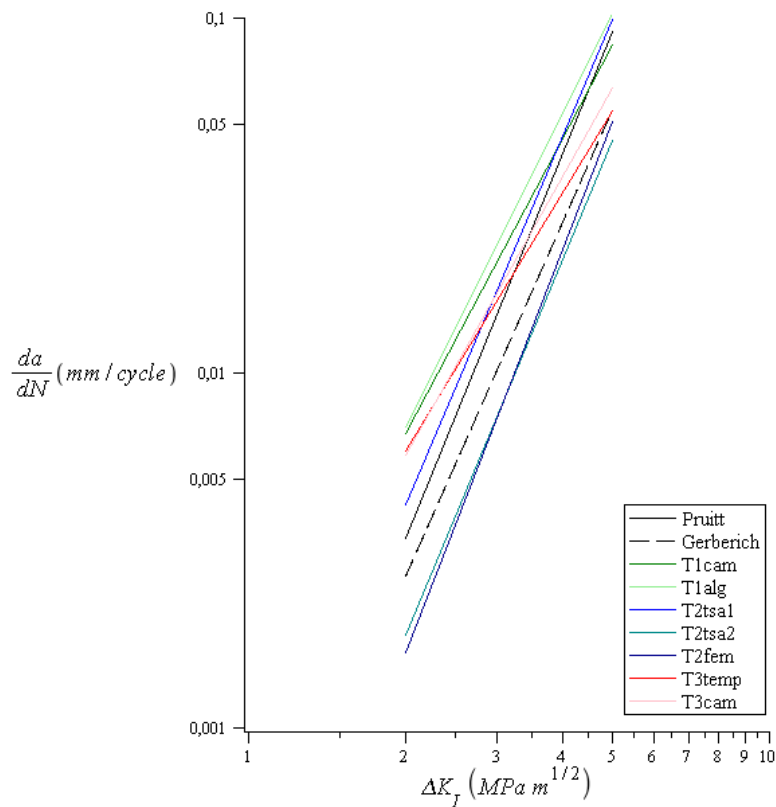


Figure 6.16: Plot of all da/dN results and references.

Reasonable agreement is seen throughout all results and between them and the references. Nonetheless, the observed differences are attributed to the lack of mean load control, for reasons explained in chapter 4, and to variations in the test temperature between 20°C and almost 40°C, since, during summer in Rio the temperature can get really high. As shown by many authors and discussed in chapter 3, these variations can cause changes in both the slope and intercept of the Paris curve.

7

Final Considerations and Conclusions

7.1

Final Considerations

This thesis has presented a general study of the use of thermography in the study of fatigue in polycarbonate. The results obtained show that thermographic experimental techniques are, overall, quite good to study, measure and predict the fatigue behavior of polycarbonate. Nothing in particular indicates that other materials could not be studied using the same methodologies, although not many tests are presented here.

On top of that, the experiments shown clearly indicate that the low cost non-cooled, micro-bolometric infrared camera is very well suited to perform not only regular temperature measurements, but to collect TSA data when used in conjunction with DeltaTherm2.

After a basic review of theoretical concepts, the actual fatigue study was divided in two main fields, crack initiation and crack growth. Each one of these fields were discussed by a whole chapter, and the main results and conclusions are listed here.

Crack Initiation

Within the field of crack initiation, the first use of thermography presented was the search and monitoring of critical points.

- Temperature measurement, through active thermography, is a very powerful tool to detect defects inside the component, that is, that are not on the observable surface.
- Finding critical points with TSA is, most of the times, a trivial task, since the highest stresses usually happen at the border of a component. If that is the case, the boundary condition can be used to equate the TSA signal with the maximum principal stress.
- In complex components, where the stress field has a maximum away from a border, stress separation techniques must be used.
- Experimental stress separation can be done using TSA and photoelasticity simultaneously. Polycarbonate is particularly useful

in this approach, since it can be used as a coating for both techniques.

- Analytical stress functions are often used as a way to numerically separate the stresses in what is called a hybrid TSA technique.

Then, the stress concentration problem is attacked using TSA.

- The stress concentration factor of a SAE keyhole specimen is experimentally determined using TSA. Two approaches were used, a simpler one, that utilize the boundary condition argument, and a more complex one that used the stress function approach.
- The simpler method used a simple equation to extrapolate the experimental data, and achieved acceptable results for K_t by doing so.
- The second method separated the principal stresses using a Airy's stress function approach. The whole stress field was determined for all components. Again, the results obtained were good.
- The TSA results were compared to DIC, photoelasticity and FEM results. All of them shown good agreement with the literature predicted value.

After the stresses acting on the specimen have been fully determined, the actual fatigue properties are determined with the use of thermography.

- The fatigue limit of polycarbonate is measured through the thermographic method (Risitano's method), which is based on an energy approach to fatigue damage.
- The material presents different thermal behavior when cyclically loaded below and above a certain stress level. This stress level is supposed to be the fatigue limit.
- The results obtained using this method are similar to those found on the literature for polycarbonate, although they fell on the high end of the range, which was not expected.
- More test could be done to make a better estimation of the fatigue limit.
- Later, an experiment had a specimen failing by fatigue under loading range lower than what was measured as the fatigue limit.

The next, and final, step of the crack initiation study is to determine the SN curve of the material.

- The thermographic method is once again used to accomplish this task. Based on the same energy approach to fatigue damage.
- This time, a parameter Φ is used as a material property, which indicates that a critical damage level has been reached and failure is eminent.
- With this approach, the fatigue curve is, theoretically, measured using a single specimen, in a very short time.
- The results found show good agreement with the literature curves for polycarbonate, although some variables could not be controlled or compared.
- Parameters such as the mean stress, frequency and thickness effect were all constant throughout the study.

Crack Growth

After a crack has initiated in a component, the study of its propagation under cyclic loading is presented. Thermography once again is used, and the first step is to apply TSA to fracture mechanics.

- An algorithm was developed to measure mode I stress intensity factors using TSA and Westergaard's stress function for the stress field near the tip of a fatigue crack. Two approaches were used, a linear and a non-linear one.
- The algorithm has a routine to make an initial crack tip position estimation. This estimation is needed in both approaches.
- The linear approach is very sensitive to initial crack tip location estimation while the non-linear approach uses the crack tip position as an adjustable variable, resulting in a powerful tool for finding the actual tip of the crack.
- The algorithm selects data points to be fitted using a linearity argument, which certifies that the points can be modelled by the Westergaard's equations.
- The results obtained for ΔK_I were verified using simulated TSA data, FEM analysis, as well as other experimental technique (DIC).
- The results shown very good agreement with the predicted and measured values.

The next step on the way to determining the crack growth behavior of polycarbonate was to measure crack growth rates. Once again, thermography was used to accomplish the task.

- Two approaches were used to measured crack growth rate. The first used the non-linear SIF measurement algorithm, while the second used temperature measurements.
- When using the algorithm to follow the crack tip throughout its propagation, the results were very good. The reference measurements were made using a regular digital camera, which took photos simultaneously to the TSA data collection, and posterior visual determination of the crack tip position.
- The second method was found during tests that explored a possible damage approach to fatigue crack propagation, based on the parameter proposed by Risitano.
- The findings show that the rise in temperature provoked by the fatigue damage is proportional to the crack growth rate.
- Both approaches had great results, and could locate the actual crack tip location with high accuracy.

Finally, the crack growth rate vs SIF curves could be measured.

- Three tests were conducted, two of them used the algorithm and the third used the temperature method combined with the FEM result.
- The results obtained for all tests showed good agreement between themselves and in comparison to literature results.
- The effect of crack closure was observed in the second test, which demonstrated that the algorithm measures the effective SIF range through TSA data.
- Eventual variations on the results are attributed to mean stress and temperature differences.

Overall, the results were good, highlighting the power of thermography as a tool for fatigue studies. On top of that, the inexpensive setup used in this work proved to be just as reliable for this type of studies as the more common, more expensive equipment.

7.2

Conclusions

For fatigue crack initiation, the thermographic method produced great results when it comes to fatigue limit and fatigue curve measurements. The greatest feature of the method is the capability to reduce the time needed for such tests to a fraction of the traditional methods.

In the study of fatigue crack growth, thermographic stress analysis, combined with numerical approaches, was proven to be particularly useful, both in measuring stress concentrations and stress intensity factors. With some tweaking, the algorithms presented could be used to make these measurements in real time.

Special attention is drawn to two points: the possibilities opened by the thermographic approach to fatigue damage, i.e. a point-by-point evaluation of the Φ integral during fatigue crack propagation, and to the relationship between the crack propagation rate and the temperature change ahead of the crack (See Figure 6.12 on page 86).

Overall, infrared thermography is a great tool for fatigue studies and, through temperature measurements, permits the observation of a somewhat unexplored aspect of the problem, from which new models as well as new testing routines can be devised.

8

Bibliography

- [1]W. Herschel, "**Experiments on the refrangibility of the visible rays of the sun**", Philosophical Transactions of the Royal Society of London, vol. 90, pp. 284–292, 1800.
- [2]Flir, "**The ultimate infrared handbook for R&D professionals**". FLIR AB, Boston. Available for free at www.flir.com.
- [3]M. Razeghi, "**Current status and future trends of infrared detectors**", Opto-Electronics Review, vol. 6, no. 3, pp. 155–194, 1998.
- [4]S. P. Langley, "**The bolometer**", in Valleggheny Observatory, The Society Gregory, New York, NY, USA, 1880.
- [5]Corsi, Carlo. "**Infrared A Key Technology for Security Systems**", Advances in Optical Technologies, 2012 (2012) 1-15.
- [6]Overstreet R., "**Notes on using Microbolometers at high frame rates**", FLIR systems, April 2013, Rev3.
- [7]Ibarra-Castanedo C. "**Quantitative Subsurface Defect Evaluation by Pulsed Phase Thermography: Depth Retrieval with the Phase**" PhD thesis, Universite Laval, 2005.
- [8]K. Chatterjee, S. Tuli, S. Pickering, and D. Almond. "**A comparison of the pulsed, lock-in and frequency modulated thermography nondestructive evaluation techniques**" NDT&E International, 44:655–667, 2011.
- [9]Y.Y. Hung, Y.S. Chen, S.P. Ng, L. Liu, Y.H. Huang, B.L. Luk, R.W.L. Ip, C.M.L. Wu and P.S. Chung. "**Review and comparison of sherography and active thermography for nondestructive evaluation**" Materials Science and Engineering R., 64:73–112, 2009.
- [10]Sun, J.G., "**Analysis of pulsed thermography methods for defect depth prediction**" Journal of Heat Transfer, 128, p. 329-338, 2006.
- [11]Avdelidis, N.P., Ibarra-Castanedo, C., Maldague, X., Marioli-Riga, N.P., and Almond, D.P., "**A thermographic comparison study for the assessment of composite patches**" Infrared Physics and Technology, 45: p. 291-299, 2004.
- [12]Maldague X. P. V., Jones T. S., Kaplan H., Marinetti S. and Prystay M. "**Chapter 2: Fundamentals of Infrared and Thermal Testing: Part 1. Principles of Infrared and Thermal Testing**" in Nondestructive Handbook, Infrared and Thermal Testing, Volume

3, X. Maldague technical ed., P. O. Moore ed., 3rd edition, Columbus, Ohio, ASNT Press, 2001.

[13]Thomson, W. (Lord Kelvin), "**On the Dynamical Theory of Heat**", Transaction of the Royal Society of Edinburgh, vol.20, pp. 261-283, 1853.

[14]Barber J. R., "**Elasticity**", Solid Mechanics and its Applications Vol. 172, Chapter 14, p. 219-225, 2010.

[15] Dulieu-Barton, J.M., "**Introduction to thermoelastic stress analysis**", Strain, pp. 35-39, May, 1999.

[16]Dulieu-Smith, S.M., "**Alternative calibration techniques for quantitative thermoelastic stress analysis**", Strain , pp. 9-16, February, 1995.

[17]Freire J.L.F., Waugh R.C., Fruehmann R., Dulieu-Barton J.M., "**Using Thermoelastic Stress Analysis to Detect Damaged and Hot Spot Areas in Structural Components**", In: Proc. Of the XXXII Congresso Nacional de Ensaaios Não Destrutivos e Inspeção (CONAEND), São Paulo, ABENDI, 2014.

[18]Stress Photonics Inc., "**DeltaTherm 2 Manual**", v6, January, 2016.

[19]Khaja A.A., Rowlands R.E., "**Experimentally determined stresses at geometric discontinuities using simple stress functions**", Journal of Engineering Mechanics, Vol. 141, 11, 2015.

[20]Kurunthottikkal Philip S., Rowlands R.E., "**Hybrid full-field stress analysis of loaded perforated asymmetrical plate**", Proceedings of the 2015 Annual Conference on Experimental and Applied Mechanics, Vol.9, pp. 235-241, 2016.

[21]Samad W.A., Rowlands R.E., "**On improving thermoelastic stress analysis data near edges of discontinuities**", Proceedings of the 2014 Annual Conference on Experimental and Applied Mechanics, Vol. 6, pp. 157-162, 2015.

[22]Lin S.J., Samad W.A., Khaja A.A., Rowlands R.E., "**Hybrid thermoelastic stress analysis**", Experimental Mechanics, 55, pp. 653-665, 2015.

[23]Barone, S., Patterson, E.A., "**Full-field separation of principal stresses by combined Thermo- and Photoelasticity**", Experimental Mechanics, Vol. 36 (4), pp. 318-324, 1996.

[24]Barone, S., Patterson, E. A., "**The development of simultaneous thermo- and photo-elasticity for principal stress analyses**", Strain, pp. 57-65, May 1999.

[25]Wang W., Fruehmann R.K., Dulieu-Barton J.M., "**Application of Digital Image Correlation to address complex motions in thermoelastic stress analysis**", Strain, Vol. 51 (5), pp. 405-418, October 2015.

- [26]Silva M.L., Ravichandran G., "**Combined thermoelastic stress analysis and digital image correlation with a single infrared camera**", The Journal of Strain Analysis for Engineering Design, Vol. 46 (8), pp. 783-793, November 2011.
- [27]Machin A.S., Sparrow J.G., Stimson M.G., "**Mean stress dependence of the thermoelastic constant**", Strain, pp. 27-30, February 1987.
- [28]Dunn, S., Lombardo, D., Sparrow, J.G., "**The mean stress effect in metallic alloys and composites**", Proceedings of the International Conference on Stress and Vibration (Including 3rd Int.Conf. on Stress Analysis by Thermoelastic techniques), London, SPIE vol. 1084, pp. 129-142, 1989.
- [29]Wong, A.K., Dunn, S.A., Sparrow, J.G., "**Residual stress measurement by means of the thermoelastic effect**", Nature, vol. 332, No. 6165, pp. 613-615, April 1988.
- [30]Quinn S., Dulieu-Barton J.M., Eaton-Evans J., Fruehmann R.K., Tatum P.J. "**Thermoelastic assessment of plastic deformation**", The Journal of Strain Analysis for Engineering Design, Vol. 43 (6), pp. 451-468, 2008.
- [31]Jones, R., Heller, M., Lombardo, D., Dunn, S, Paul, J., Saunders, D., "**Thermoelastic assessment of damage growth in composites**", Composite Structures, 12, pp. 291-314, 1989.
- [32]Zhang, D., Sandor, B.I., "**A thermoelastic theory for damage in anisotropic materials**", Fatigue and Fracture of Engineering Materials and Structures, 13, pp. 497-509, 1990.
- [33]Dulieu-Smith, J.M., Stanley, P., "**A review of damage studies in fiber reinforced composites using the thermoelastic technique**", XXV AIAS National Conference & Int. Conf. On Material Engineering, Lecce, pp. 891-898, 1996.
- [34]Tomlinson R.A., Olden E.J., "**Thermoelasticity for the analysis of crack tip stress fields – A review**", Strain, Vol. 35 (2), pp. 49-55, 1999.
- [35]Tomlinson R.A., Nurse A.D., Patterson E.A, "**On determining stress intensity factors for mixed-mode cracks from thermoelastic data**", Fatigue and Fracture of Engineering Materials and Structures, Vol. 20 (2), pp. 217-226, 1997.
- [36]Dulieu-Barton J.M., Fulton M.C., Stanley P., "**The analysis of thermoelastic isopachic data from crack tip stress fields**", Fatigue and Fracture of Engineering Materials and Structures, Vol. 23, pp. 301-313, 2000.
- [37]Lin S.T., Feng Z., Rowlands R.E., "**Thermoelastic determination of stress intensity factors in orthotropic composites using the J-integral**", Engineering Fracture Mechanics, Vol. 56 (4), pp. 579-592, 1997.
- [38]Diaz F.A., Patterson E.A., Tomlinson R.A., Yates J.R., "**Measuring stress intensity factors during fatigue crack growth using thermoelasticity**", Fatigue and Fracture of Engineering Materials and Structures, Vol. 27 (7), pp. 571-583, 2004.

- [39]Tomlinson R.A., Du Y., Patterson E.A., "**Understanding Crack Tip Plasticity – a Multi-Experimental Approach**", Applied Mechanics and Materials, Vol. 70, pp. 153-158, 2011.
- [40]Marsavina L., Tomlinson R.A., Patterson E.A., Yates J.R., "**Investigation of Crack Closure by Using Thermoelastic Stress Analysis**", Proceedings of the 16th European Conference of Fracture, Alexandroupolis, Greece, pp. 443-444, July 2006.
- [41]Patki A.S., Patterson E.A., "**Thermoelastic stress analysis of fatigue cracks subject to overloads**", Fatigue and Fracture of Engineering Materials and Structures, Vol. 33 (12), pp. 809-821, 2010.
- [42]Tomlinson R.A., Marsavina L., "**Thermoelastic investigations for fatigue life assessment**", Experimental Mechanics, Vol. 44 (5), pp. 487-494, 2004.
- [43]Yates J.R., Zanganeh M. Tomlinson R.A., Brown M.W. Diaz Garrido F.A., "**Crack paths under mixed mode loading**", Engineering Fracture Mechanics, Vol. 75 (3-4), pp. 319-330, 2008.
- [44]CASTRO, J. T. P. D.; MEGGIOLARO, M. A.: "**Fadiga – Técnicas e Práticas de Dimensionamento Estrutural sob Cargas Reais de Serviço. Volume I – Iniciação de Trincas.**" CreateSpace, 2009.
- [45]Vieira R.B., Philip S.K., Gonzáles G.L.G, Freire J.L.F., Yang B., Rowlands R.E. "**Determination of a U-notch aluminum plate stress concentration factor by thermoelasticity**", In: Proc. Of the 13th Conferência sobre Tecnologia de Equipamentos, Recife, ABENDI, 2015.
- [46]Vieira R.B., Freire J.L.F., "**Using Visual Techniques (TSA, DIC and Photoelasticity) to Determine Stress Concentration Factors**", In: Proc. Of the 17th International Conference on Experimental Mechanics, Rhodes, July 3-7, 2016.
- [47]Yang M., Pizhing Q., "**Generalized fatigue model for polymer matrix composites**", In: Proc. Of the International Conference on Computational & Experimental Engineering and Sciences, Vol. 6 (3), pp.157-168, 2008.
- [48]CASTRO, J. T. P. D.; MEGGIOLARO, M. A.: "**Fadiga – Técnicas e Práticas de Dimensionamento Estrutural sob Cargas Reais de Serviço. Volume II – Propagação de Trincas, Efeitos Térmicos e Estocásticos.**" CreateSpace, 2009.
- [49]"**Overview of materials for Polycarbonate, Extruded**", Available in: <http://www.matweb.com/search/DataSheet.aspx?MatGUID=501acbb63cbc4f748faa7490884cdbca>, accessed on: 02/09/2016.
- [50]Crawford R.J., "**Plastics Engineering**", 2nd edition, New York, Pergamon Press, 1990.
- [51]Hertzberg R.W., Nordberg H., Manson J.A., "**Fatigue Crack Propagation in Polymeric Materials**", Journal of Materials Science, Vol. 5, pp. 521-526, 1970.

- [52]Martin G.C., Gerberich W.W., “**Temperature effects on fatigue crack growth in polycarbonate**”, Journal of Materials Science, Vol. 11, pp. 231-238, 1976.
- [53]Hertzberg R.W., Manson J.A., “**Fatigue of Engineering Plastics**”, New York, Academic Press, 1980.
- [54]Pitman G., Ward I.M., “**The molecular weight dependence of fatigue crack propagation in polycarbonate**”, Journal of Materials Science, Vol. 15, pp. 635-645, 1980.
- [55]Pruitt L., Rondinone D., “**The effect of specimen thickness and stress ratio on the fatigue behavior of polycarbonate**”, Polymer Engineering and Science, Vol. 36 (9), pp.1300-1305, 1996.
- [56]Haddaoui N., Chudnovsky A., Moet A., “**Ductile fatigue crack propagation in polycarbonate**”, Polymer, Vol. 27, pp. 1377-1384, 1986.
- [57]James M.N., Christopher C.J., Lu Y., Patterson E.A., “**Fatigue crack growth and craze induced crack tip shielding in polycarbonate**”, Polymer, Vol. 53, pp.1558-1570, 2012.
- [58]Chen T.J., Bosnyak C.P., Kao C.I., Chudnovsky A., “**A fatigue crack initiation map for polycarbonate**”, Journal of Applied Pol. Science, Vol. 49 (11), pp1909-1919, 1993.
- [59]Chen T.J., Chudnovsky A., Bosnyak C.P., “**Observations of the micro-mechanisms of fatigue-crack initiation in polycarbonate**”, Journal of Materials Science, Vol. 29 (22), pp 5903-5910, 1994.
- [60]Mackay M.E., Teng T.G., Schultz J.M., “**Craze roles in the fatigue of polycarbonate**”, Journal of Materials Science, Vol. 14, pp. 221-227, 1979.
- [61]Wang B., Lu H., Tan G., Chen W., “**Strength of damaged polycarbonate after fatigue**”, Theoretical and Applied Fracture Mechanics, Vol. 39, pp. 163-168, 2003.
- [62]Jansen R.P.M., Kanter D., Govaert L.E., Meijer H.E.H., “**Fatigue Life Predictions for Glassy Polymers: A Constitutive Approach**”, Macromolecules, Vol. 41, pp.2520-2530, 2008.
- [63]Kim G.H., Lu H., “**Accelerated fatigue life testing of polycarbonate at low frequency under isothermal condition**”, Polymer Testing, Vol. 27, pp. 114-121, 2008.
- [64] “**SAE Keyhole Test Program**”, Available in: https://www.efatigue.com/benchmarks/SAE_keyhole/SAE_keyhole.html, accessed on: 10/09/2016.
- [65]Measurements Group Inc., “**Instructions for machining two-dimensional models from PSM-1**”, Instruction Bulletin IB-201, Raleigh, USA, 1974.
- [66]Alva J.G.C., “**Controle por aprendizado neuro-fuzzy aplicado a uma máquina de fadiga atuada por um músculo pneumático**”, PhD Thesis, Pontifícia Universidade Católica do Rio de Janeiro, Departamento de Engenharia Mecânica, 2013.

- [67]Shukla A., Dally J.W., “**Experimental Solid Mechanics**”, College Enterprises, 2010.
- [68]La Rosa G., Risitano A., “**Thermographic methodology for rapid determination of the fatigue limit of materials and mechanical components**”, International Journal of Fatigue, Vol. 22, pp. 65-73, 2000.
- [69]Fargione G., Geraci A., La Rosa G., Risitano A., “**Rapid determination of the fatigue curve by the thermographic method**”, International Journal of Fatigue, Vol. 24, pp. 11-19, 2002.
- [70]Plastifab Inc., “**Polycarbonate Tube Data Sheet**”, Available in: http://www.plastifab.ca/a-upload-pdfs/4_02.pdf, accessed on: 16/09/2016.
- [71]“**Typical properties of polycarbonates (PC)**”, Available in: [http://www.nationwideplastics.net/pdfs/Polycarbonate/\(New\)%20Polycarbonate%20Material%20Datasheet.pdf](http://www.nationwideplastics.net/pdfs/Polycarbonate/(New)%20Polycarbonate%20Material%20Datasheet.pdf), accessed on: 16/09/2016.
- [72]McKeen L.W., “**Fatigue & Tribological Properties of Plastics & Elastomers**”, 2nd edition, William Andrew, 2009.
- [73]Stanley P., Chan W. K., “**The determination of stress intensity factors and crack tip velocities from thermoelastic infra-red emissions**”, In: Proceedings of International Conference of Fatigue of Engineering Materials and Structures, c262, IMechE, Sheffield, UK, pp. 105–114, 1986.
- [74]Stanley P., Dulieu-Smith J. M., “**Progress in the thermoelastic evaluation of mixed mode stress intensity factors**”, In: Proceedings of the SEM Spring Conference on Experimental Mechanics, Dearborn, pp. 617–626, 1993.
- [75]Lesniak J. R., Bazile D. J., Boyce B. R., Zickel M. J., Cramer K. E., Welch, C. S., “**Stress intensity measurement via infrared focal plane array**”, Non-Traditional Methods of Sensing Stress, Strain, and Damage in Materials and Structures. ASTM STP 1318, Philadelphia, 1997.
- [76]Díaz F. A., Yates J. R., Tomlinson R. A., Patterson E. A., “**Some observation on the application of thermoelasticity to fatigue cracks**”, In: Proceedings of SEM Conference, Milwaukee, USA, 2002.
- [77]Díaz F. A., Patterson E. A., Tomlinson R. A., Yates J. R., “**Measuring stress intensity factors during fatigue crack growth using thermoelasticity**”, Fatigue and Fracture of Engineering Materials and Structures, Vol. 27, pp. 571-583, 2004.
- [78]Nelder J. A., Mead R., “**A simplex method for function minimization**”, The Computer Journal, Vol. 7, pp. 308–313, 1965.
- [79]González G. L. G., Díaz J. G., González J. A. O., Castro J. T. P., Freire J. L. F., “**Determining SIFs Using DIC Considering Crack Closure and Blunting**”, In: Proceedings of the SEM Annual Conference on Experimental Mechanics, Orlando, Jun. 6-9, 2016.

Appendix 1

Simple Test on Defect Location by Active Thermography

In order to demonstrate the power of active thermography in detecting defects, this appendix describes two simple experiments.

The specimens consisted of a rectangular bar of a glass-fiber composite with polymeric matrix and a rectangular bar of steel. Both had holes drilled into them as shown by Figure A1.1.

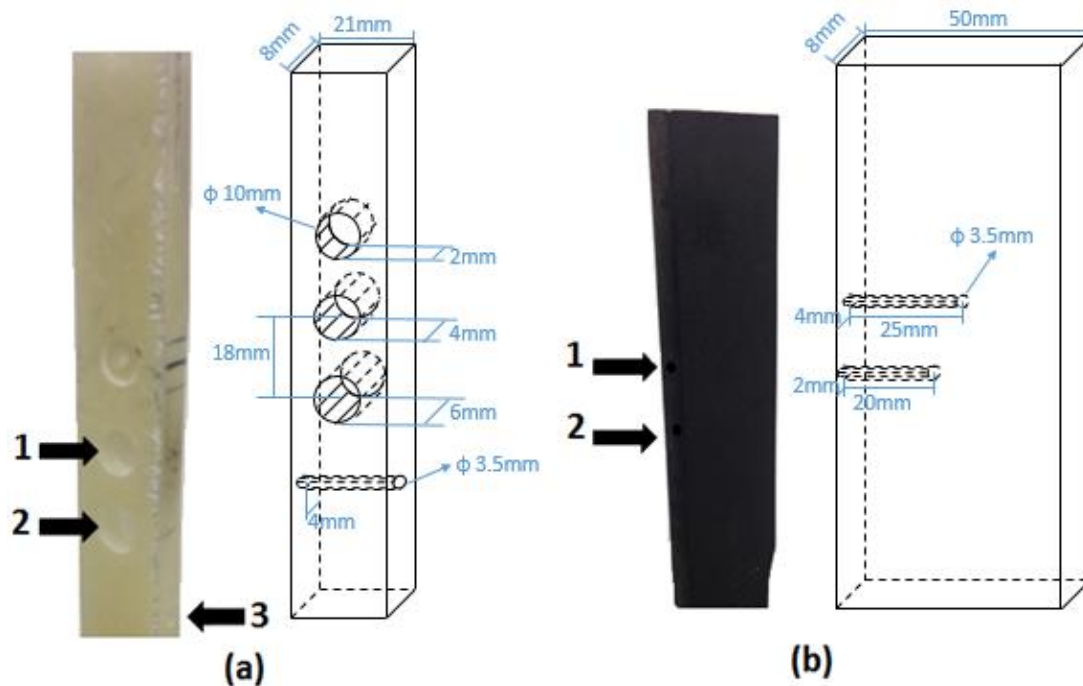


Figure A1.1: a) Composite and b) steel specimens for defect detection experiment.

The composite specimen had three holes drilled from its back up to $\frac{1}{4}$, $\frac{1}{2}$ (1) and $\frac{3}{4}$ (2) of its thickness. The $\frac{1}{4}$ hole could not be detected, hence why it is not identified neither with an arrow neither by a number. Another passing hole (3) was drilled through its width with the center at a $\frac{1}{2}$ thickness depth.

The steel specimen had two holes drilled through its width up to about half the way, one (1) with its center at a $\frac{1}{2}$ thickness depth and the other (2) with its center at $\frac{1}{4}$ thickness depth.

The experimental procedure consisted of pointing the infrared camera at the specimens and applying heat to the front surface using a commercial hair dryer (2000W), then, the difference in temperature decay can be seen.

For the composite specimen, because of its thermal properties (good insulator / bad conductor) the heat was applied for a relatively long period (15-20 seconds) and

then the temperature decay observed as time passed. Figure A1.2a shows the thermographic image obtained 5 seconds after the heat source was turned off while Figure A1.2b shows the temperature profile along the vertical centerline at the same instant.

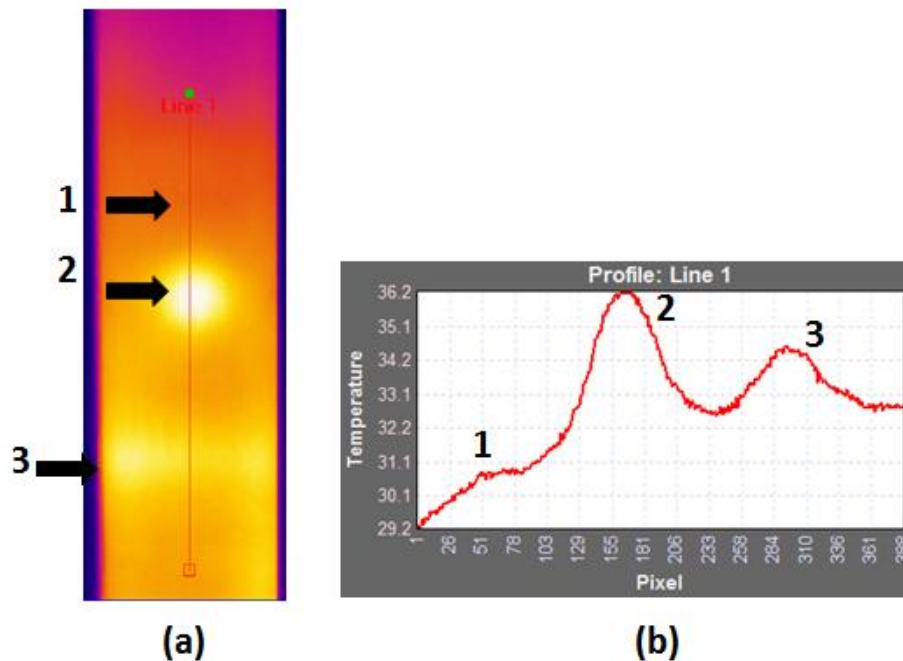


Figure A1.2: a) Thermographic image and b) Temperature profile for the composite specimen.

While only holes 2 and 3 are seen in the thermographic image, all three defects can be easily perceived with the help of the temperature profile.

For the steel specimen, the procedure is a little bit more complex. Since it is a much better heat conductor, the temperature becomes uniform much faster. In order to detect the holes, the heat source was cyclically turned on and off at approximately 0.1Hz. A High Sensitivity Mode filter was added to the image which is then seen using frame skipping ("fast forward" technique). Figure A1.3a shows the resulting thermographic image while Figure A1.3 b shows the temporal plot of the difference in temperature between cursor 1 and cursor 2 as seen in the image.

Again, the defects can be quite easily seen by investigation of the image, but much more clearly perceived by looking at the temporal plot as the difference in the peaks of the reference temperature (cursor 2 – blue) away from the defect and at the hole (cursor 1 – green).

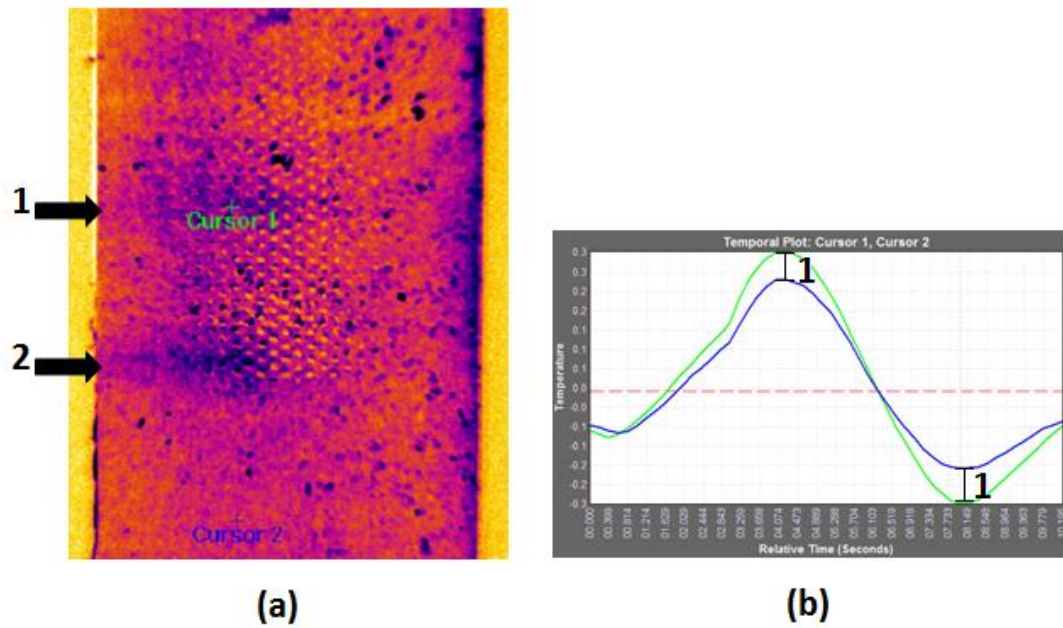


Figure A1.3: a) Thermographic image and b) temporal plot of the steel specimen.

This experiment, although rudimentary, showcases very well the power of thermography when it comes to detecting defects in structures. More refined experiments generally use more controlled heat sources, such as stroboscopic infrared lights, at specific frequency rates [6-10].

Appendix 2

Simple Test on Monitoring Cracks in Welded Joints

This appendix describes an experiment that followed the crack initiation and propagation process of a welded joint. The specimen shown Figure A2.1 consists of two steel plates welded with three weld beads, 2 on the front side (shown in the image) and 1 on the rear side.

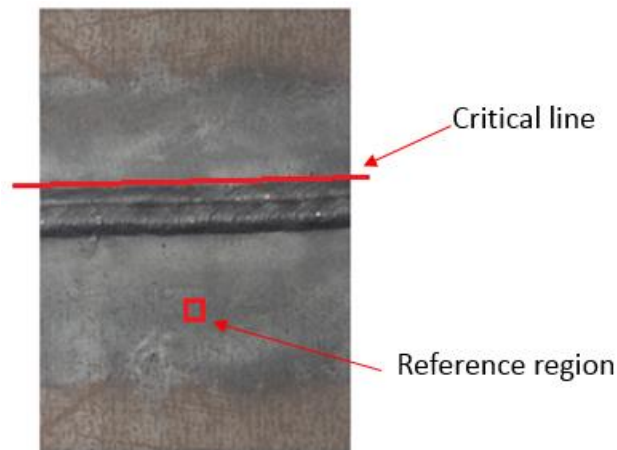


Figure A2.1: Welded Joint, steel specimen.

TSA was used to monitor the stress map and the critical points of the specimen's front surface while it was cyclically loaded with 105.5kN load range and a 0.1 load ratio at 15Hz. Figure A2.2 shows the development of the stress map (0, 85000, 115000, 190000 and 215000 cycles), with the green arrows pointing at the region of maximum stress.

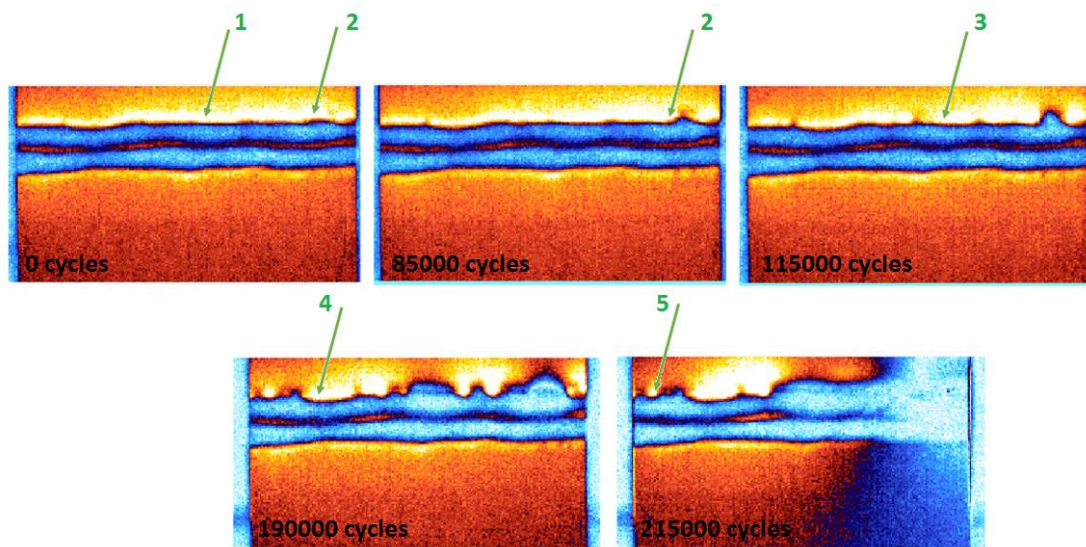


Figure A2.2: Development of stresses on welded specimen's surface.

Many cracks initiate simultaneously (unloaded, blue parts of the specimen in Figure A2.2), they slowly propagate until they merge into one big crack through the thickness of the specimen. Then, the crack propagates to the left, making the region of maximum stress (at the tip of the crack) go in the same direction.

Figure A2.3 shows the plot of the horizontal position of the maximum stress region (horizontal axis) versus the number of cycles (vertical axis). It is noticeable how the maximum stress region starts at the right side, varying its position, and then travels to the left

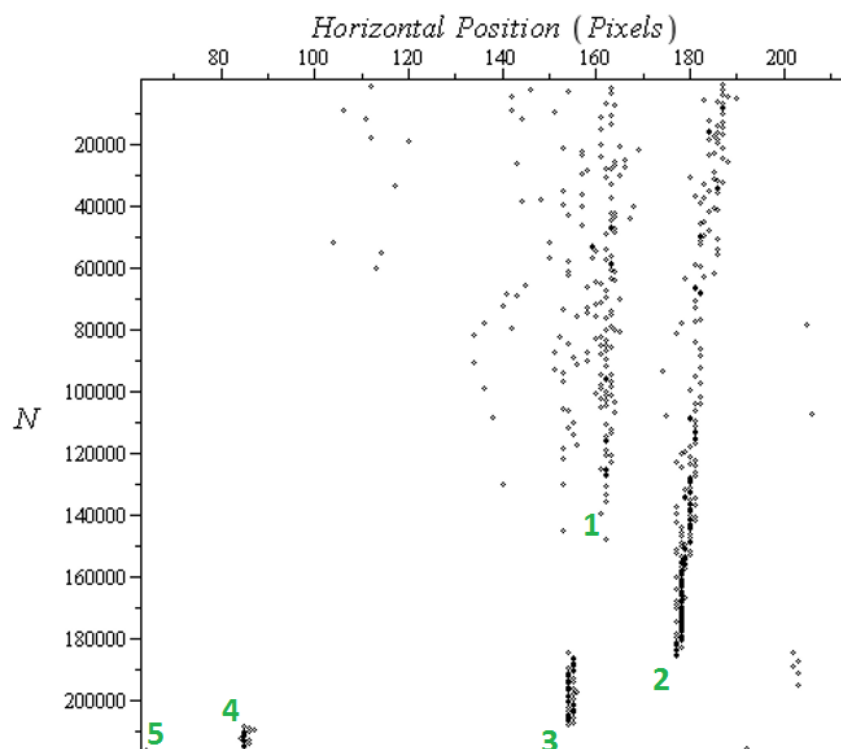


Figure A2.3: Horizontal position of maximum stress region throughout the cycles.

Taking the 5 points indicate in Figure A2.2 by green arrows and plotting their TSA data in Cam. Units (not calibrated) as a function of the number of cycles, Figure A2.4 shows the profile of maximum stress along time.

Taking the integral of each curve as a damage parameter of each point of the critical horizontal line, the resulting damage of each point, and of a reference point at a nominal region of the specimen (see Figure A2.1), are listed at the legend of the graph.

The points that failed, that is, where the crack has passed through, always have a higher damage parameter. The proposal is that, crack growth behavior could be modeled and predicted based on this point by point damage analysis.

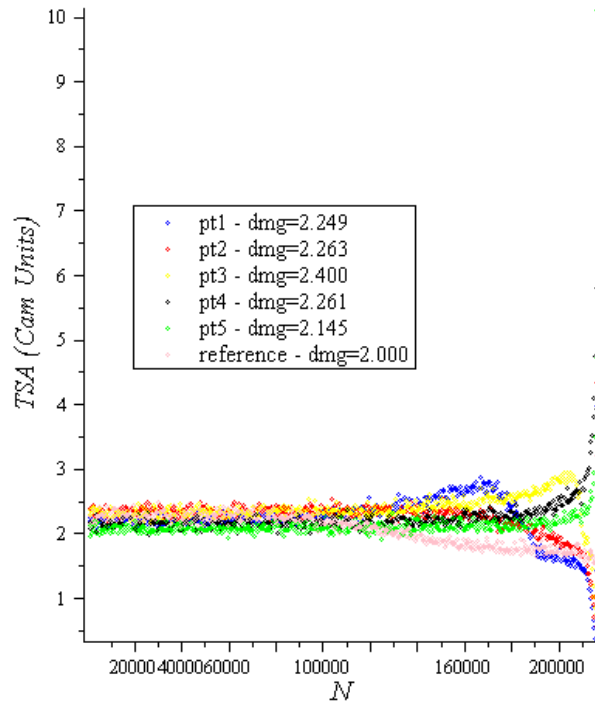


Figure A2.4: TSA vs cycles curves for the maximum stress points.

Repeating the integration process, for all points along the critical horizontal line, Figure A2.5 shows the plot of the damage parameter vs the horizontal position. It is possible to see a trend where the cracked points show a higher damage result. More tests are definitely required before any more speculation about the utility of this parameter.

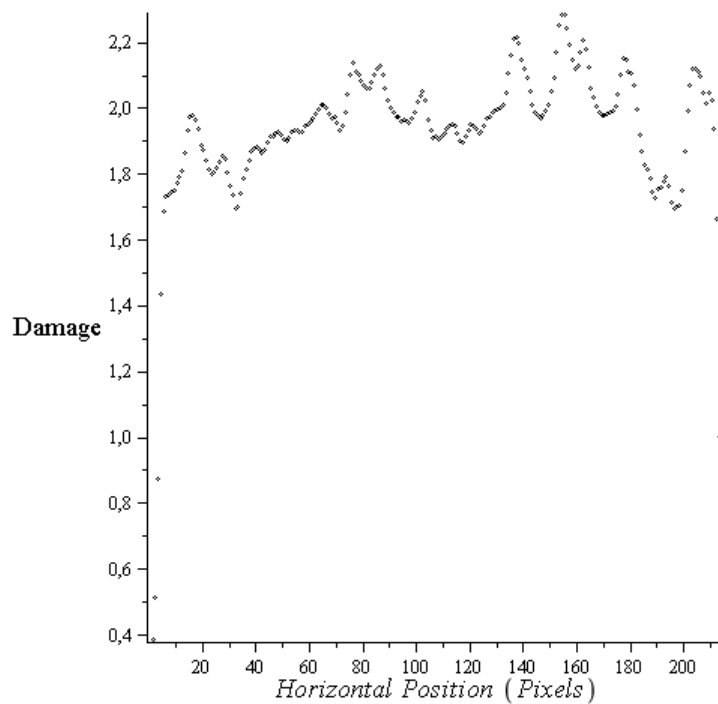


Figure A2.5: Damage for all points along the horizontal critical line.

Appendix 3

PALSUN™ Polycarbonate Datasheet and Tensile Tests

Data Sheet - PALSUN®

Flat Solid Polycarbonate Sheet



Product Definition

PALSUN® - Co-extruded UV protection on one side

Thickness Range

1 to 12 mm

Flammability

Standard	Classification
EN 13501	B, s1, d0
NSP 92501, 4	M2
UL Classified	File e221255

*All the above depends on thickness.

For additional information please contact PALRAM.

Typical Physical Properties

Property	Standard	Conditions	Unit	Value
Density	ASTM D792		g/cm ³	1.2
Heat Deflection Temperature	ASTM D648	1.82 MPa	°C	130
Service Temperature Range			°C	-40 to 120
Coefficient of Linear Thermal Expansion	ASTM D696		cm/cm °C	6.5 X 10 ⁻⁵
Thermal Conductivity	ASTM C177		W/mK	0.21
Tensile Strength at Yield	ASTM D638	10 mm/min	MPa	65
Tensile Strength at Break	ASTM D638	10 mm/min	MPa	60
Elongation at Yield	ASTM D638	10 mm/min	%	6
Elongation at Break	ASTM D638	10 mm/min	%	>90
Tensile Modulus of Elasticity	ASTM D638	1 mm/min	MPa	2300
Flexural Strength	ASTM D790	1.3 mm/min	MPa	100
Flexural Modulus	ASTM D790	1.3 mm/min	MPa	2600
Impact Falling Weight (E-50)	ISO 6603/1	3mm sheet	J	158
Rockwell Hardness	ASTM D785		R Scale	125R
Light Transmission	ASTM D1003	3mm sheet	%	89
Haze	ASTM D1003	3mm sheet	%	<0.5
Yellowness Index	ASTM D1925	3mm sheet		<1

Figure A3.1: PALSUN Datasheet.

Tensile Tests

Two simple tensile tests were conducted with specimens machined from the PALSUN polycarbonate plate. The first specimen was a CR tensile specimen with dimensions described in chapter 4. The second specimen with parallel sides, has its dimensions described by Figure A3.2 below,

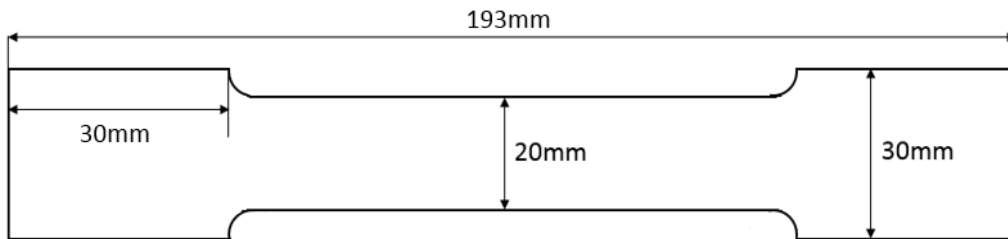


Figure A3.2: Tensile specimen dimensions.

The tests were made in a MTS universal testing machine, using a 2mm/min crosshead speed. The resulting Stress vs Displacement diagrams are shown in Figure A3.3a for the CR tensile specimen and Figure A3.3b for the parallel sides tensile specimen.

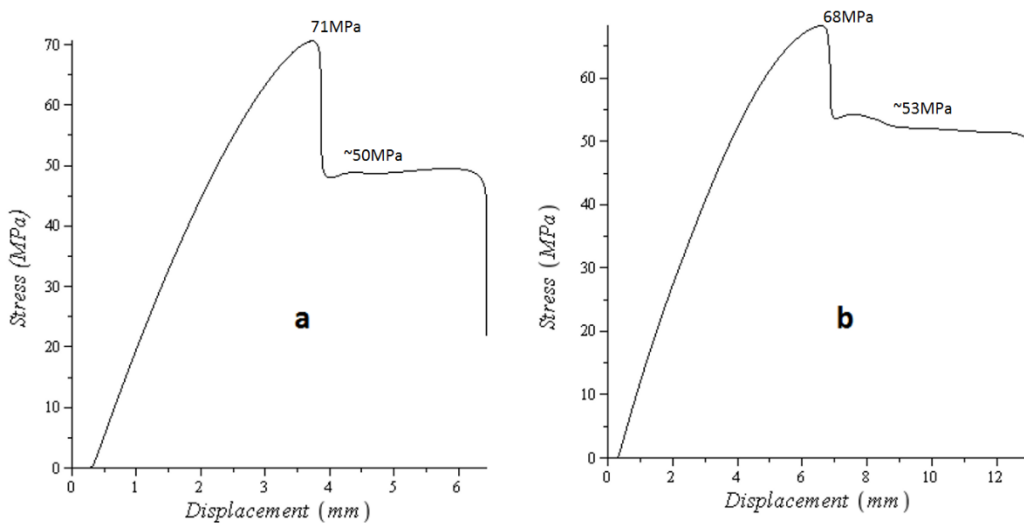


Figure A3.3: Stress vs displacement plots for a)CR and b)Parallel tensile specimens.

As expected, both presented similar yield and ultimate strengths, around the 65MPa value taken from the datasheet. The first specimen presented much less elongation, since the middle section concentrated all the yielding, while in the second specimen the whole gauge section had the same width.

Figure A3.4 shows the nominal stress vs strain (calculated as displacement/initial length) curve for the second specimen. From the initial, almost linear part, of the graph, the elastic modulus is estimated as 2088MPa.

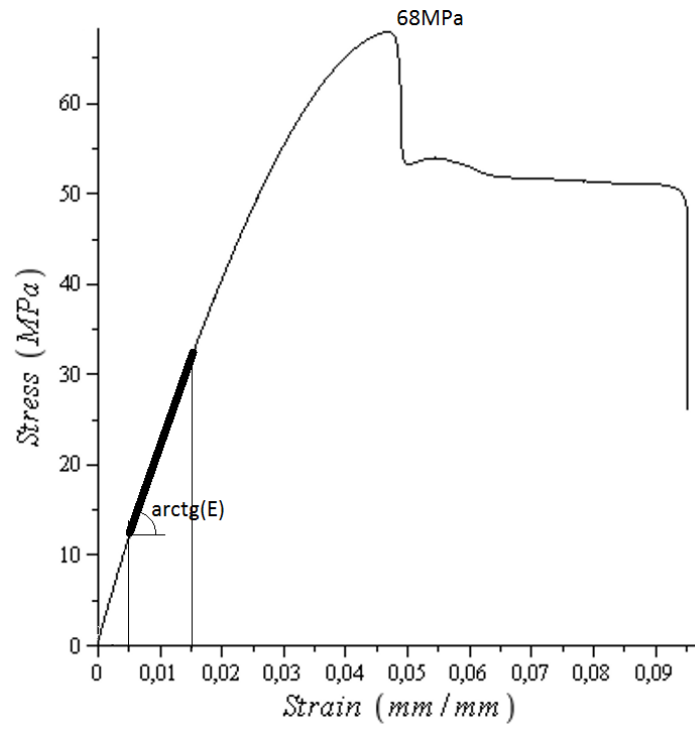


Figure A3.4: Stress vs Strain curve for the tensile specimen.

Appendix 4

Measuring the Keyhole K_t with DIC and Photoelasticity

In chapter 5, the stress concentration factor of the keyhole specimen was measured using TSA. For verification purposes, it has also been measured via DIC and Photoelasticity.

Photoelasticity

It is easy to use photoelasticity to analyze the stresses in a polycarbonate specimen, since it is birefringent and it shows the isochromatic fringes seen through a polariscope, that are the geometrical places of the points of constant $\sigma_1 - \sigma_2$ value. Measuring the K_t is once again facilitated because of the free surfaces boundary condition that $\sigma_2 = 0$. Figure A4.1 shows a series of photos taken of a statically loaded polycarbonate keyhole specimen in a transmission polariscope and through a monochromatic yellow filter. Table A4.1 shows the value of the load in each photo and the distance each fringe is from the notch root, measured in pixels.

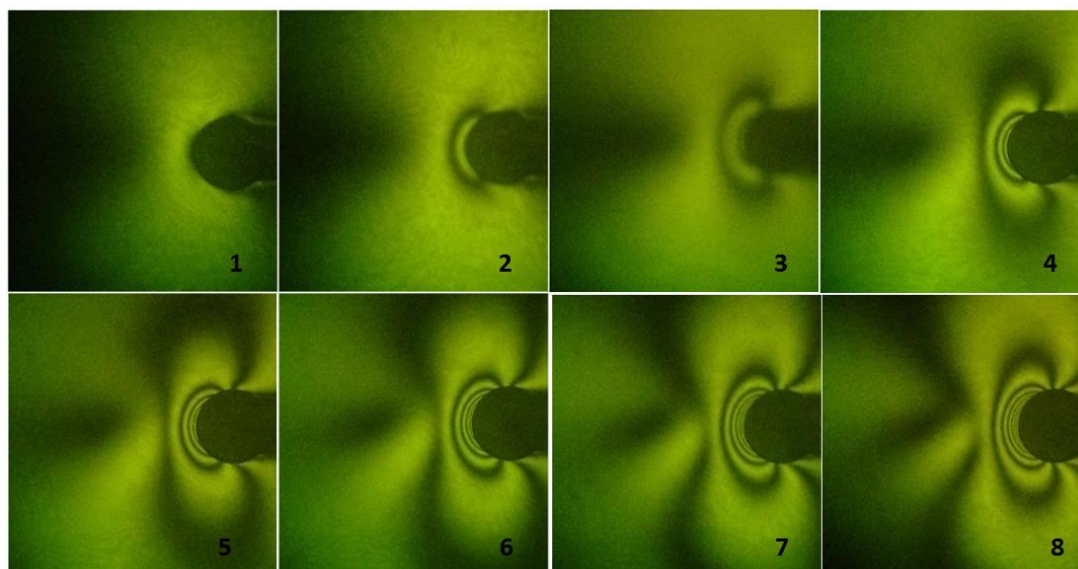


Figure A4.1: Series of Photoelastic photos.

Photo	Load (N)	Fr0	Fr1	Fr2	Fr3	Fr4	Fr5	Fr6	Fr7
1	20	260	-	-	-	-	-	-	-
2	40	275	36	-	-	-	-	-	-
3	60	250	64	16	-	-	-	-	-
4	80	277	77	31	12	-	-	-	-
5	100	270	85	42	22	8	-	-	-
6	120	281	101	54	31	17	8	-	-
7	140	281	109	65	40	25	15	7	-
8	160	279	120	71	46	30	20	12	6

Table A4.1: Fringe distance from notch tip.

Using the data from Table A4.1 in equation A4.1, it is possible to calculate the values for $\sigma_1 - \sigma_2$ along the line ahead of the notch.

$$\sigma_1 - \sigma_2 = \frac{N f_\sigma}{t} \quad (\text{A4.1})$$

where N is the fringe order number, $f_\sigma = 7.014$ is the photoelastic constant of the polycarbonate material and t is the thickness of the specimen. Figure A4.2 shows the resulting normalized plot of stress vs distance from notch. An equation similar to equation 5.2 was used to extrapolate the data and calculate the maximum stress.

$$\frac{\sigma_1 - \sigma_2}{P} = \frac{C0}{(1 + x/R)^h} + C1 + C2(1 + x/R) \quad (\text{A4.2})$$

where P is the load, x is the distance from the notch tip, R is the radius of the notch and C0, C1, C2 and h are adjustable parameters.

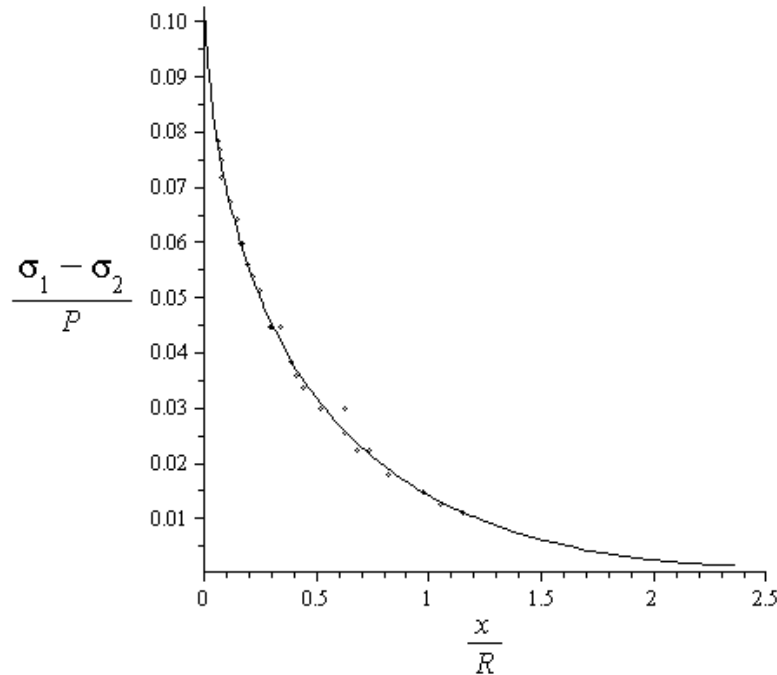


Figure A4.2: Normalized resulting photoelastic line data ahead of the notch.

The maximum stress is then determined $\sigma_{\max}/P = 0.094 \text{ MPa/N}$, and the stress concentration factor is calculated as in chapter 5. Since the geometries are the same, the nominal stress equation remains the same.

$$K_t = \left(\frac{\sigma}{P}\right)_{\max} / \left(\frac{\sigma}{P}\right)_{\text{nom}} = 3.25 \quad (\text{A4.3})$$

Digital Image Correlation

DIC is another optical experimental stress analysis technique, which has been one of the main research topics in recent days` experimental mechanics. It consists in an algorithm capable of identifying surfaces features before and after a load is applied to a specimen, and then, by correlating the positions of such features, the full field of displacements is determined. The displacements field can be differentiated to obtain the strains field. With the strain field in hands, using a stress-strain relationship (such as Hooke`s law for elastic regime) will yield the stress field acting on the surface.

The first step when using DIC is to paint the target surface with a specific pattern with many features that the software can recognize. Figure A4.3 shows the surface of the keyhole specimen painted with the pattern.



Figure A4.3: DIC pattern.

Then, by taking a photo of the unloaded specimen and another with the specimen loaded at $P= 255\text{N}$, and running the ViC3D™ software from Correlated Solutions Inc., the strain fields are calculated. Figure A4.4 shows the principal strain field (ϵ_1), and Figure A4.5 shows the normalized plot of stresses vs distance from notch, the stress-strain relationship used was the plane stress Hooke`s law described by equation A4.4.

$$\begin{bmatrix} \sigma_1 \\ \sigma_2 \\ \sigma_{12} \end{bmatrix} = \frac{E}{1 - \nu^2} \begin{bmatrix} 1 & \nu & 0 \\ \nu & 1 & 0 \\ 0 & 0 & \frac{1 - \nu}{2} \end{bmatrix} \begin{bmatrix} \epsilon_1 \\ \epsilon_2 \\ 2\epsilon_{12} \end{bmatrix} \quad (\text{A4.4})$$

where σ 's are the stress components, ϵ 's are the strain components, E is the material Young`s modulus ($E= 2300\text{MPa}$ for polycarbonate) and ν is the Poisson`s coefficient ($\nu= 0.39$ for polycarbonate).

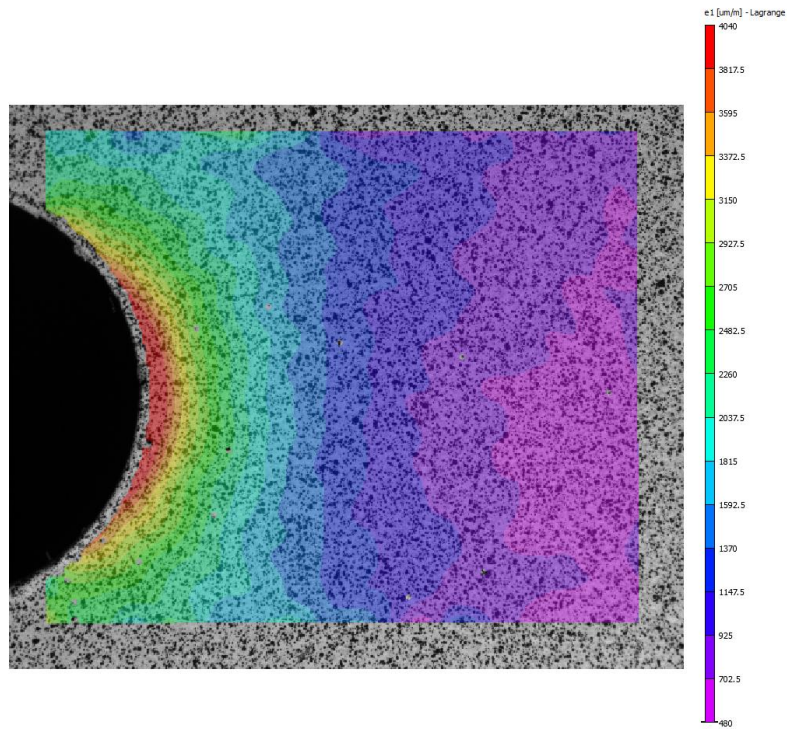


Figure A4.4: DIC principal strain field result.

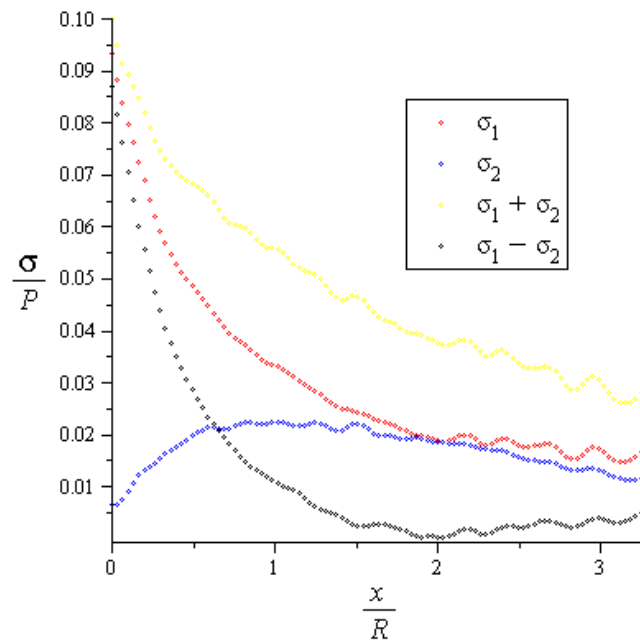


Figure A4.5: DIC stress results ahead of the notch.

Following the same procedure as before, equation A4.5 is used to fit the σ_1 data and to extrapolate the value of the maximum principal stress.

$$\frac{\sigma_1}{P} = \frac{C0}{(1 + x/R)^h} + C1 + C2(1 + x/R) \tag{ A4.5 }$$

The resulting graph is shown in Figure A4.6.

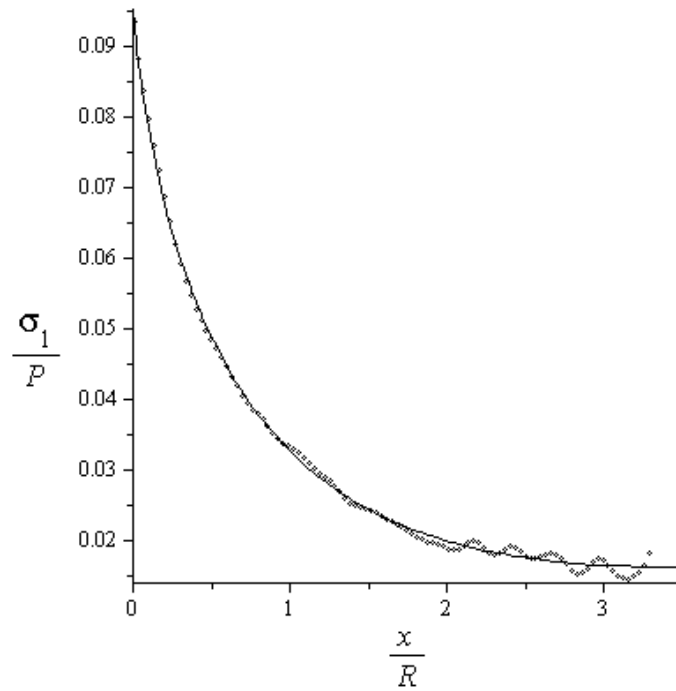


Figure A4.6: DIC fitted principal stress ahead of the notch.

The resulting maximum stress obtained was $\sigma_{\max}/P = 0.095 \text{ MPa/N}$, and the stress concentration factor is calculated as in chapter 5, since the geometries are the same, the nominal stress remains the same.

$$K_t = \left(\frac{\sigma}{P}\right)_{\max} / \left(\frac{\sigma}{P}\right)_{\text{nom}} = 3.27 \quad (\text{A4.6})$$

Appendix 5

Finite Elements Analysis of the Keyhole Specimen

A Finite Elements Analysis (FEA) was made on the keyhole specimen, in order to evaluate the stress concentration factor and the stress intensity factors. This appendix describes these analyses made using ANSYS Workbench 15.0.

Stress Concentration Factor

In order to evaluate the K_t of the keyhole, a symmetric finite elements model was made, with the dimensions show in chapter 4. The meshed model is shown in Figure A5.1

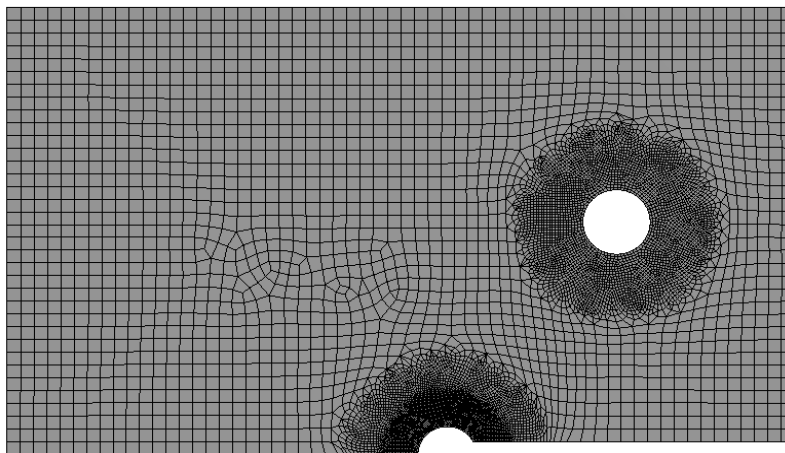


Figure A5.1: Meshed symmetric model for FEA of the keyhole specimen.

The load (100N) was applied as a bearing load at the pin-hole and the constraint was of no vertical displacement at the symmetry plane. The resulting σ_y map is shown by Figure A5.2.

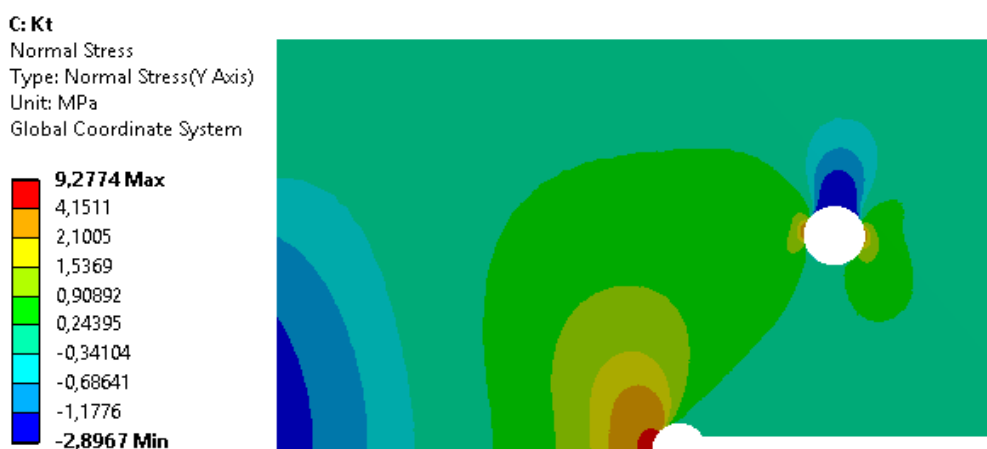


Figure A5.2: FEA resulting σ_y map for the keyhole specimen.

As expected, the stress varies along the thickness at the notch tip, Figure A5.3 shows the plot of stress concentration factor vs thickness, being the maximum value, at the middle point, $K_{t\max}=3.17$ and the minimum value, at the borders, $K_{t\min}=3.02$.

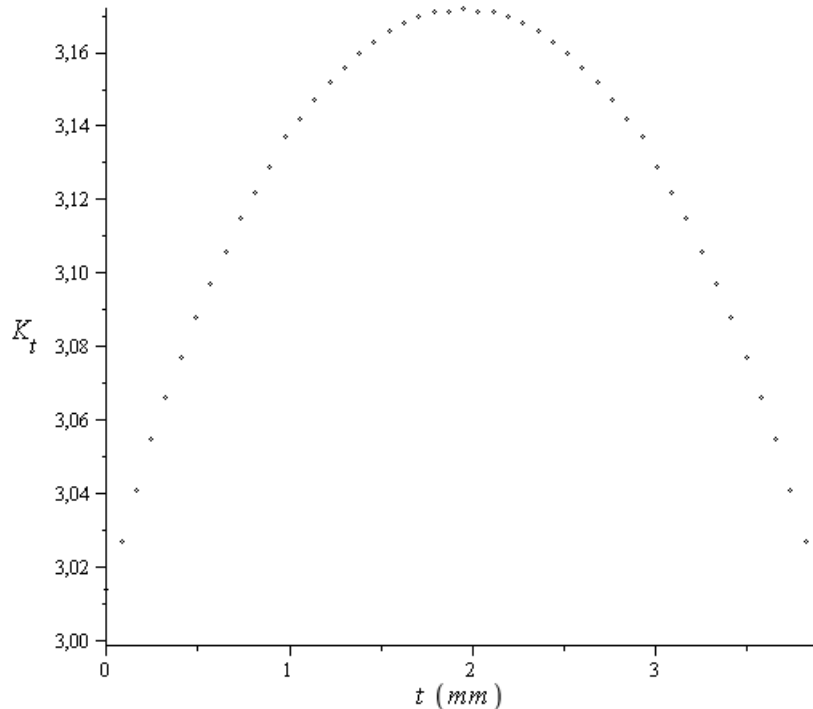


Figure A5.3: K_t vs thickness plot for the keyhole specimen.

Stress Intensity Factors

The evaluation of the SIF was done through the fracture tool of ANSYS Workbench. Using the pre-meshed crack option to model the crack, and refining the mesh around its tip, Figure A5.4 shows the resulting meshed model ($a=10\text{mm}$) and the refined region, symmetry was not used because the pre-meshed crack do not allow it.

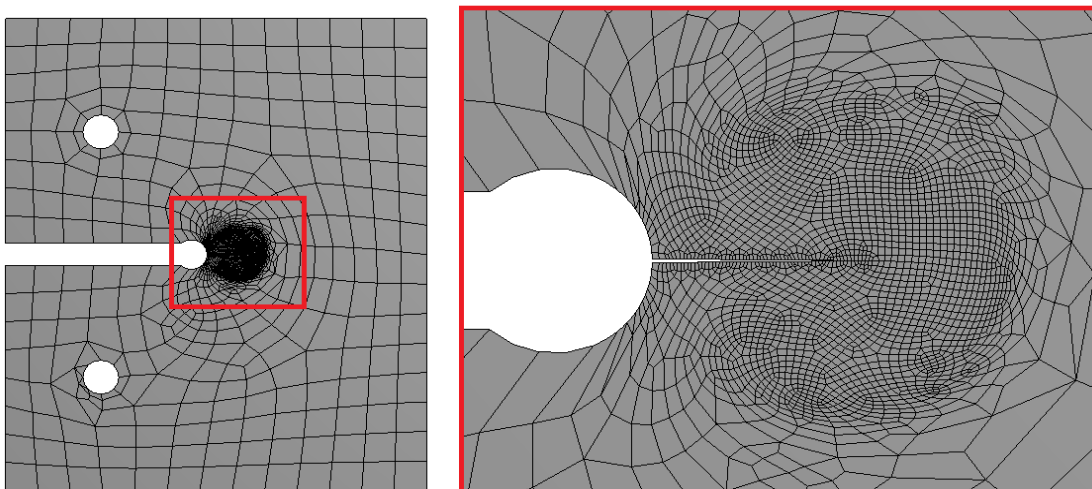


Figure A5.4: Meshed model for SIF evaluation of the keyhole specimen.

Again, the load (100N) was applied as a bearing load at the top pin-hole. The constraint, on the other hand, was added as a bearing support at the bottom pin-hole. The resulting σ_y map is shown in Figure A5.5.

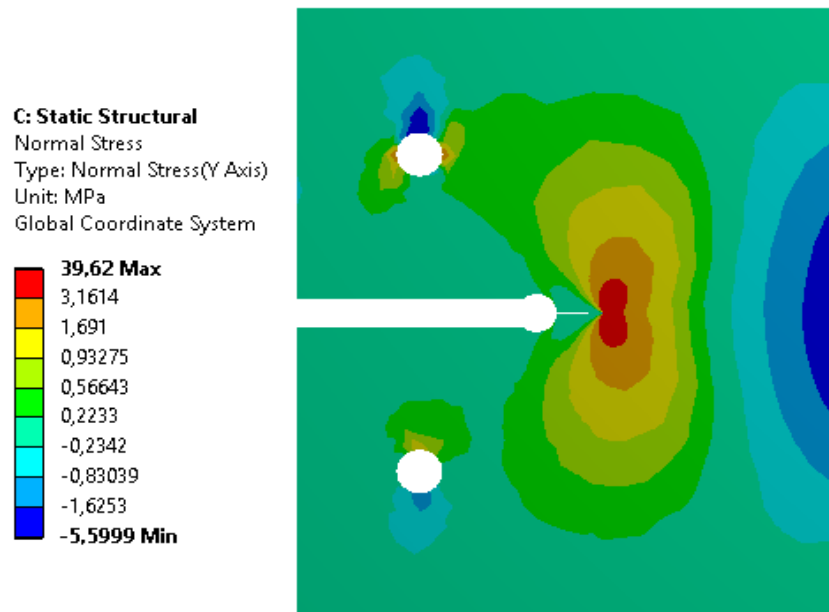


Figure A5.5: FEA resulting σ_y map for cracked ($a=10\text{mm}$) keyhole specimen.

The thickness effect makes the SIF vary along the thickness just as the K_I did. Figure A5.6 shows the plot of K_I/P vs thickness, as determined by the 6th contour in the fracture tool. The maximum and minimum values are 0.00705 and 0.00589 respectively.

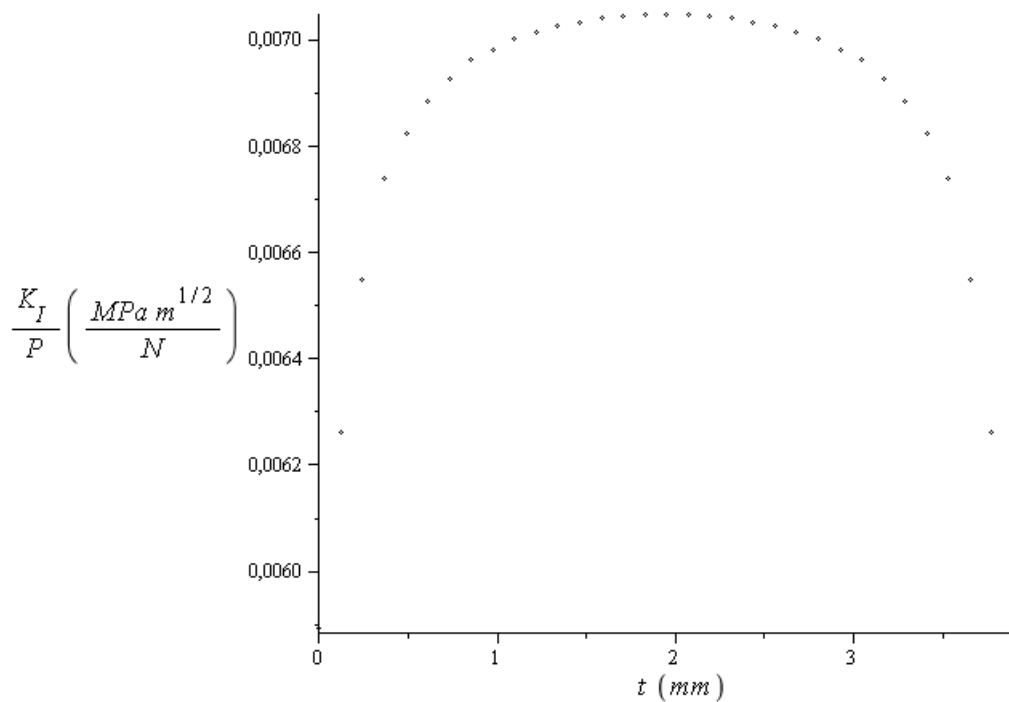


Figure A5.6: K_I/P vs thickness plot for the cracked ($a=10\text{mm}$) keyhole specimen.

The analysis was repeated for several crack sizes varying from 0.1mm to 30mm, Figure A5.7 shows the plot of K_I/P vs a for the middle point and for the border of the cracked keyhole specimen.

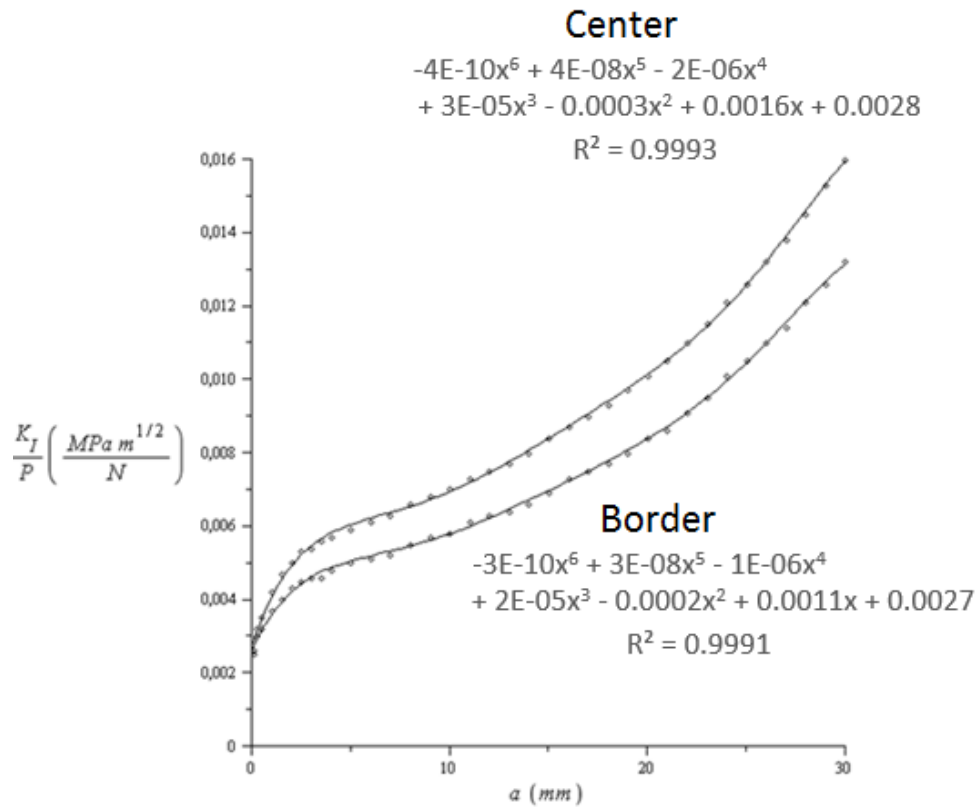


Figure A5.7: K_I/P vs a plot for the keyhole specimen.

Polynomials were used to fit the data resulting in two equations with correlation R^2 also shown in Figure A5.7.

Appendix 6

Photos of the Specimens

This appendix shows a series of photos taken from the fracture surfaces, fatigue cracks and fretting cracks of all specimens used throughout the entire study.

Each image has text boxes explaining key features, and are listed below in three categories:

Fracture surfaces

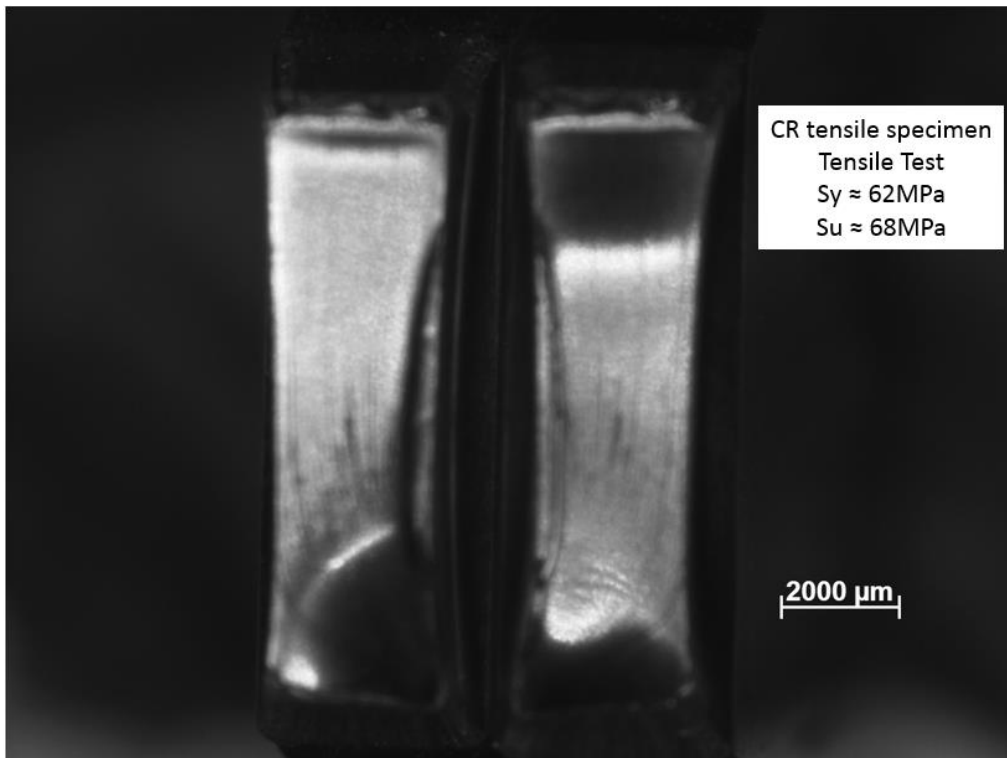


Figure A6.1: Fracture surface of CR tensile specimen after tensile test.

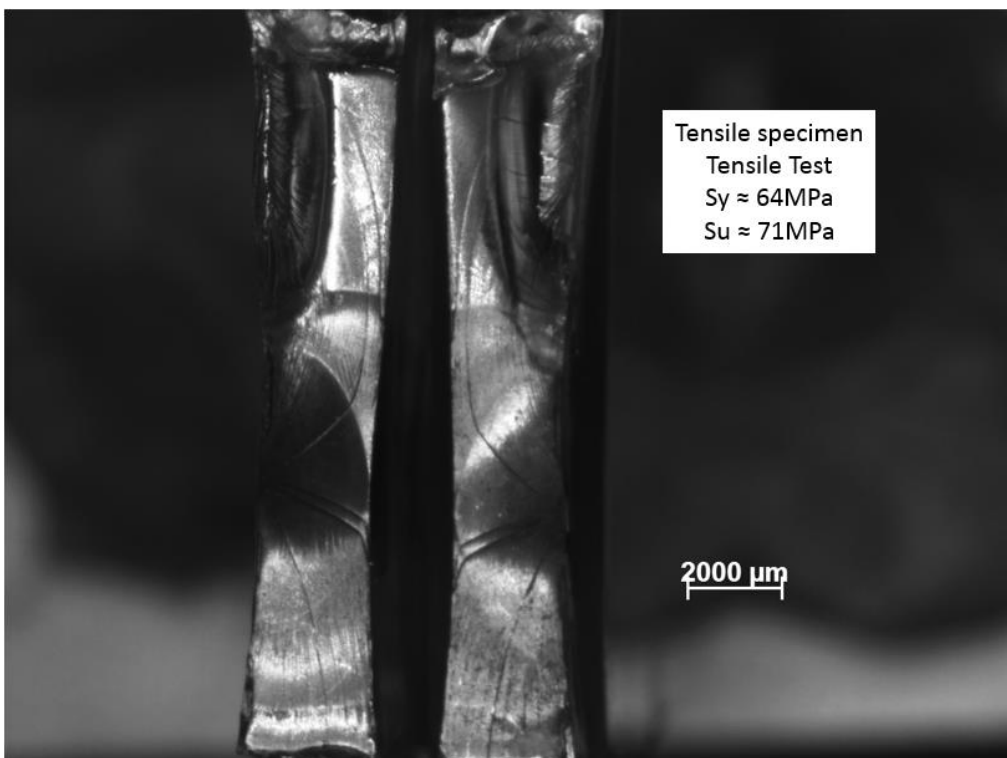


Figure A6.2: Fracture surface of tensile specimen after tensile test.

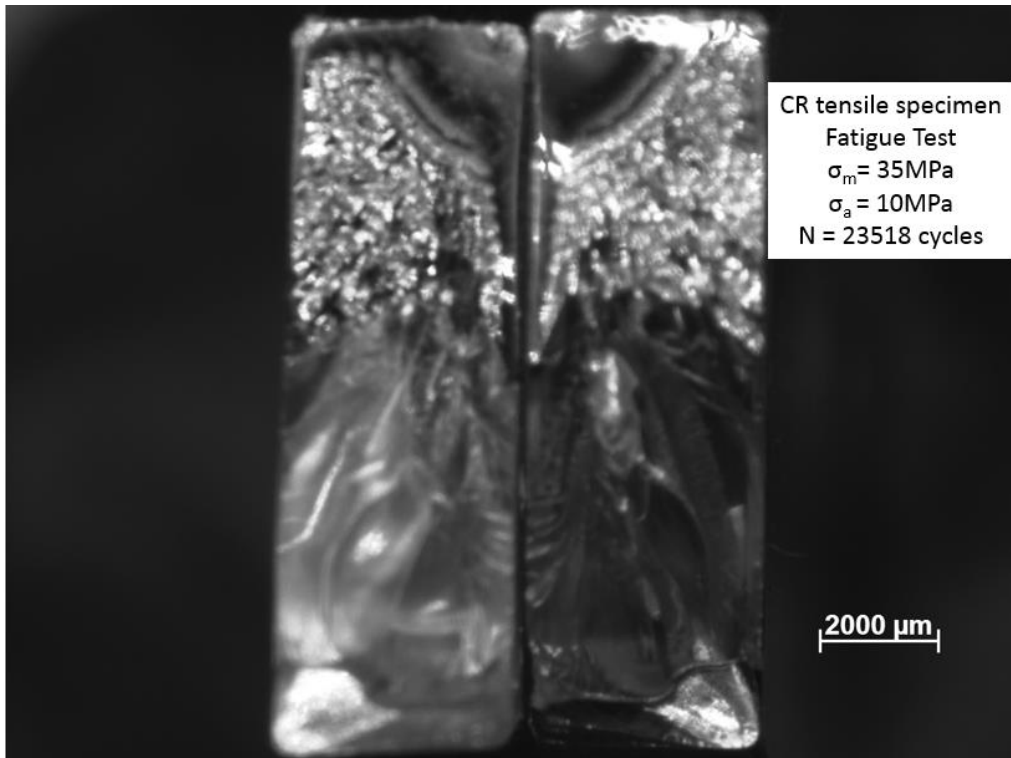


Figure A6.3: Fracture surface of CR tensile specimen after fatigue testing.

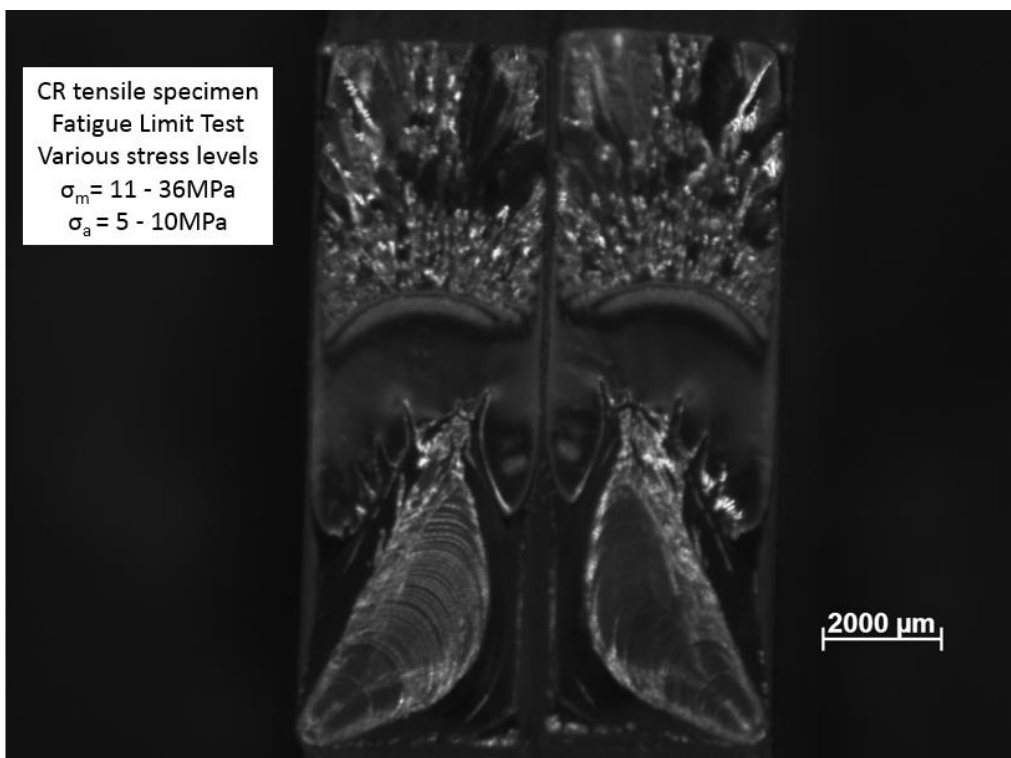


Figure A6.4: Fracture surface of CR tensile specimen after fatigue testing.

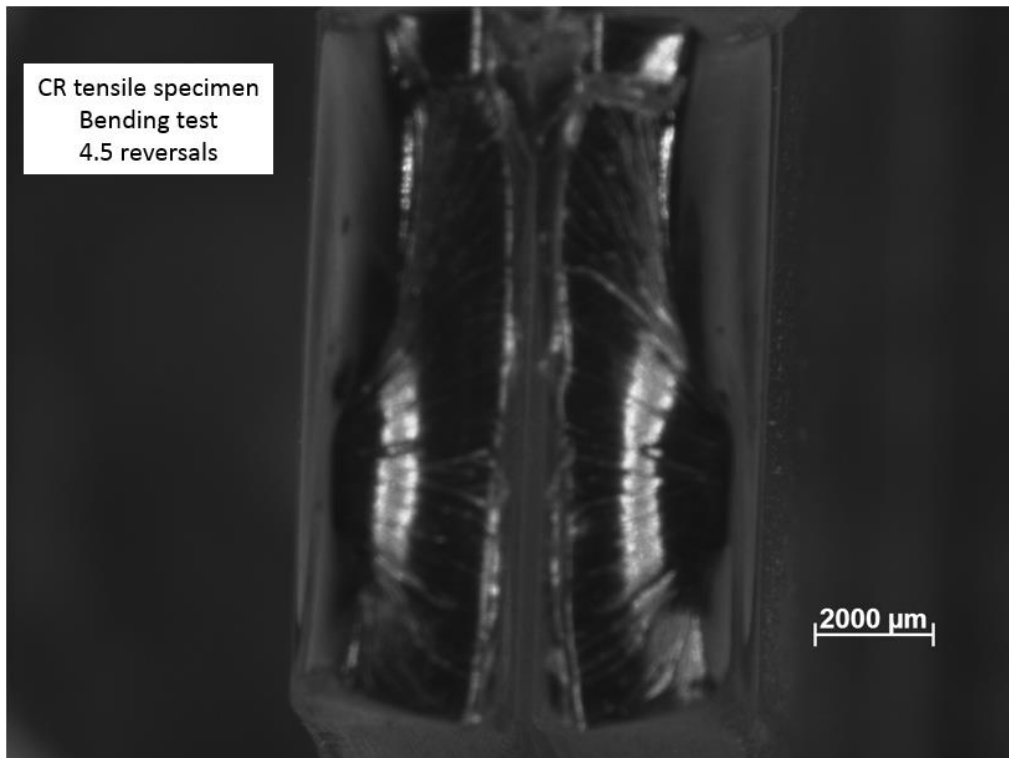


Figure A6.5: Fracture surface of CR tensile specimen after fatigue bending testing.

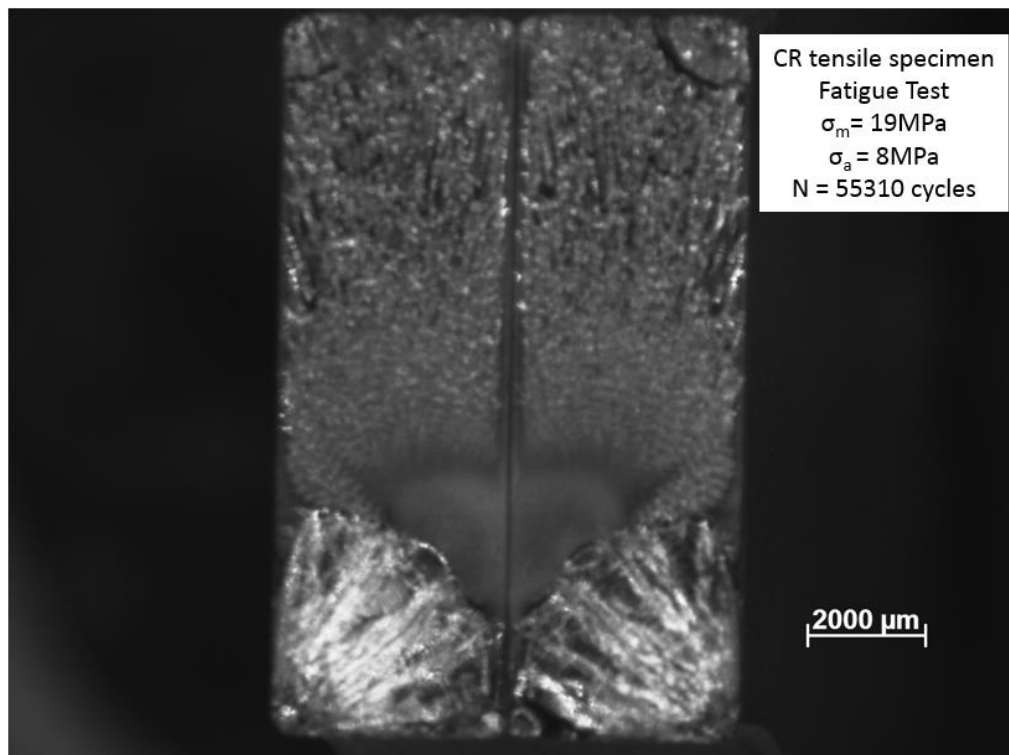


Figure A6.6: Fracture surface of CR tensile specimen after fatigue testing.

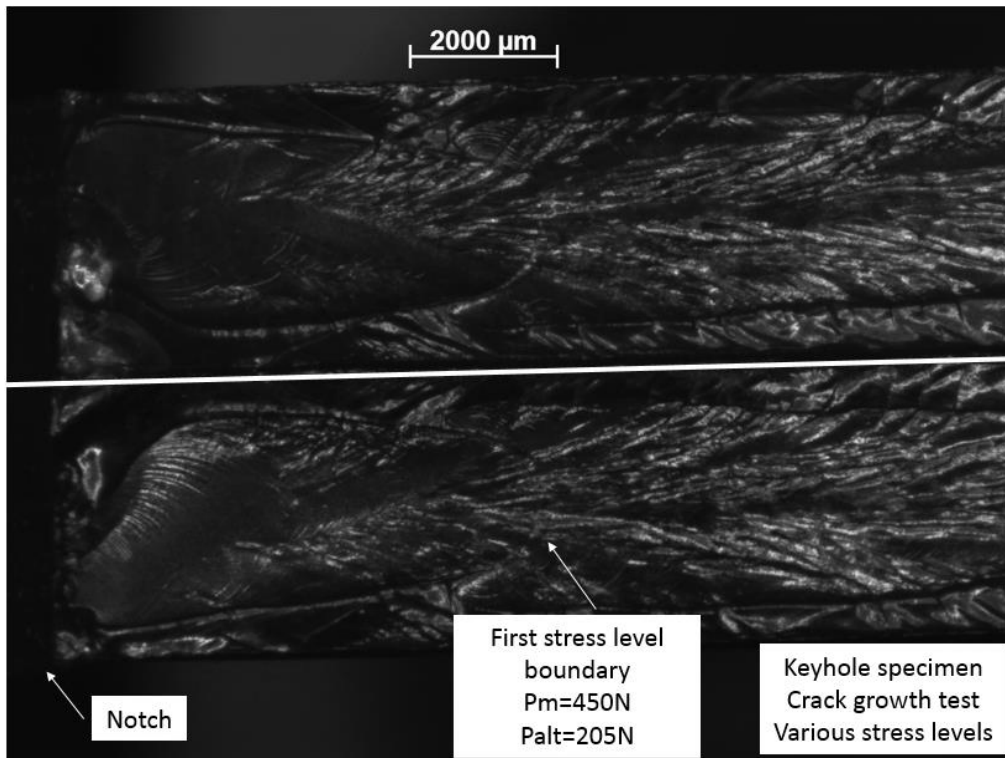


Figure A6.7: Fracture surface of Keyhole specimen after fatigue testing Part 1.

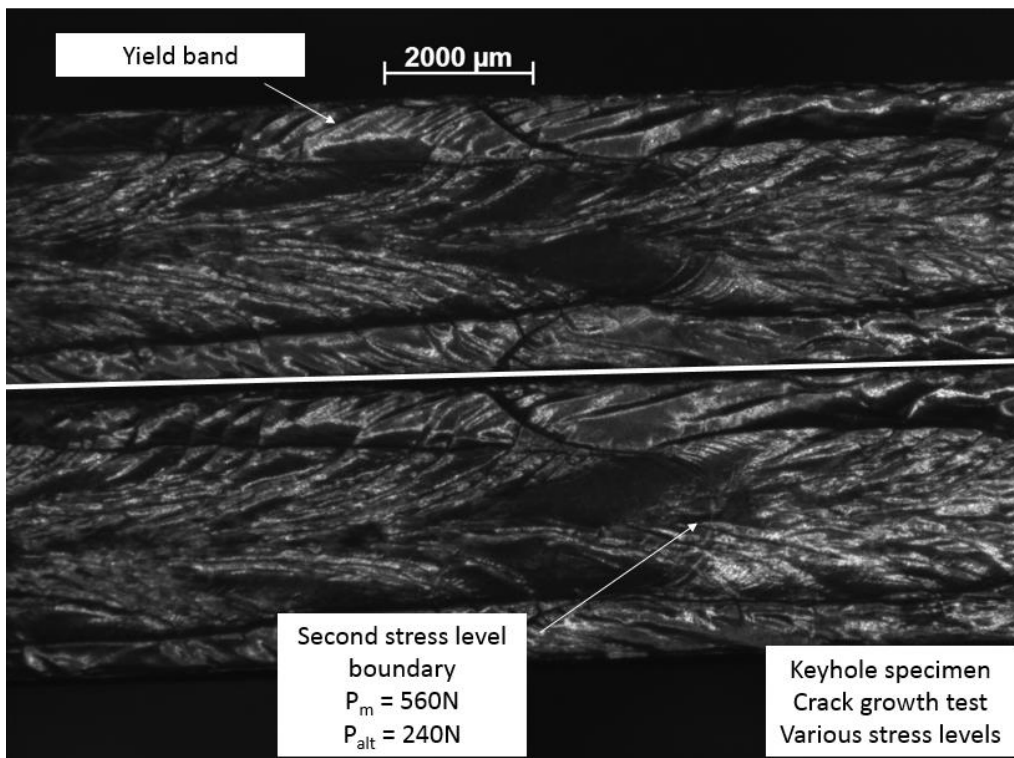


Figure A6.8: Fracture surface of Keyhole specimen after fatigue testing Part 2.

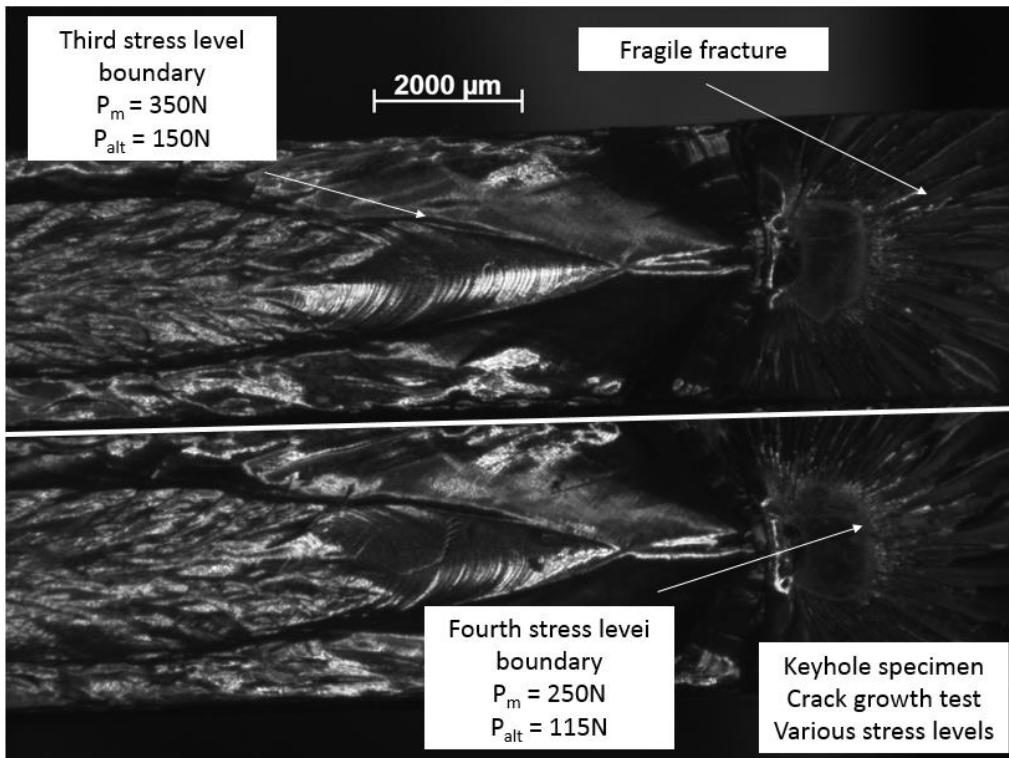


Figure A6.9: Fracture surface of Keyhole specimen after fatigue testing Part 3.

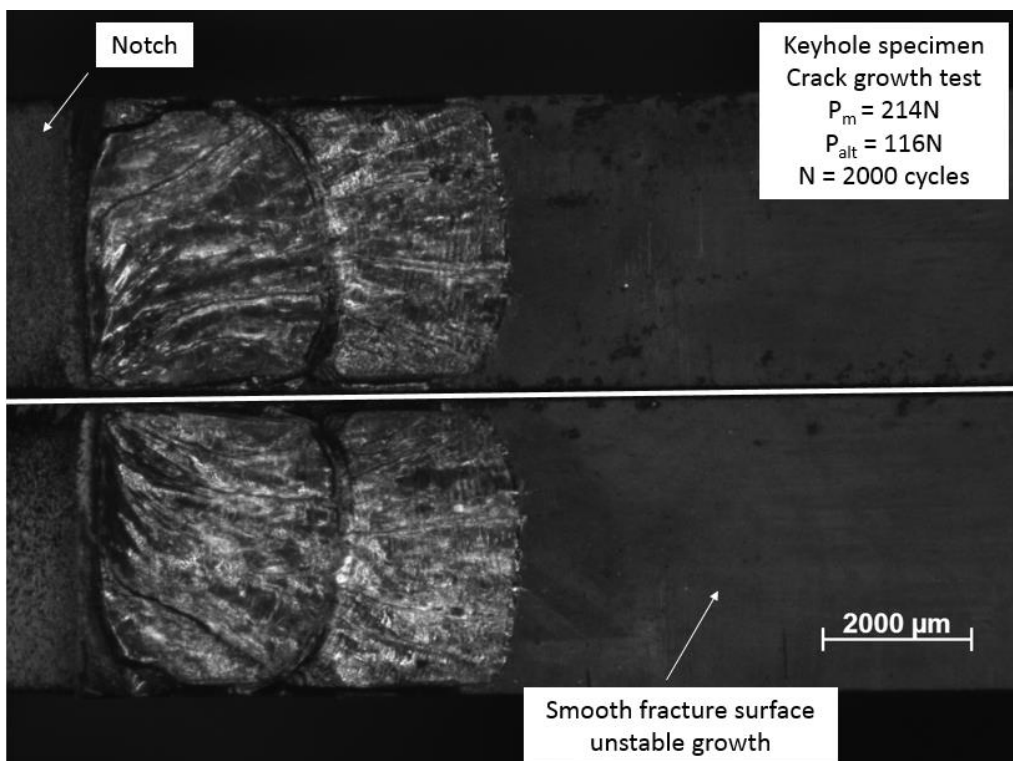


Figure A6.10: Fracture surface of Keyhole specimen after fatigue testing.

Fatigue cracks

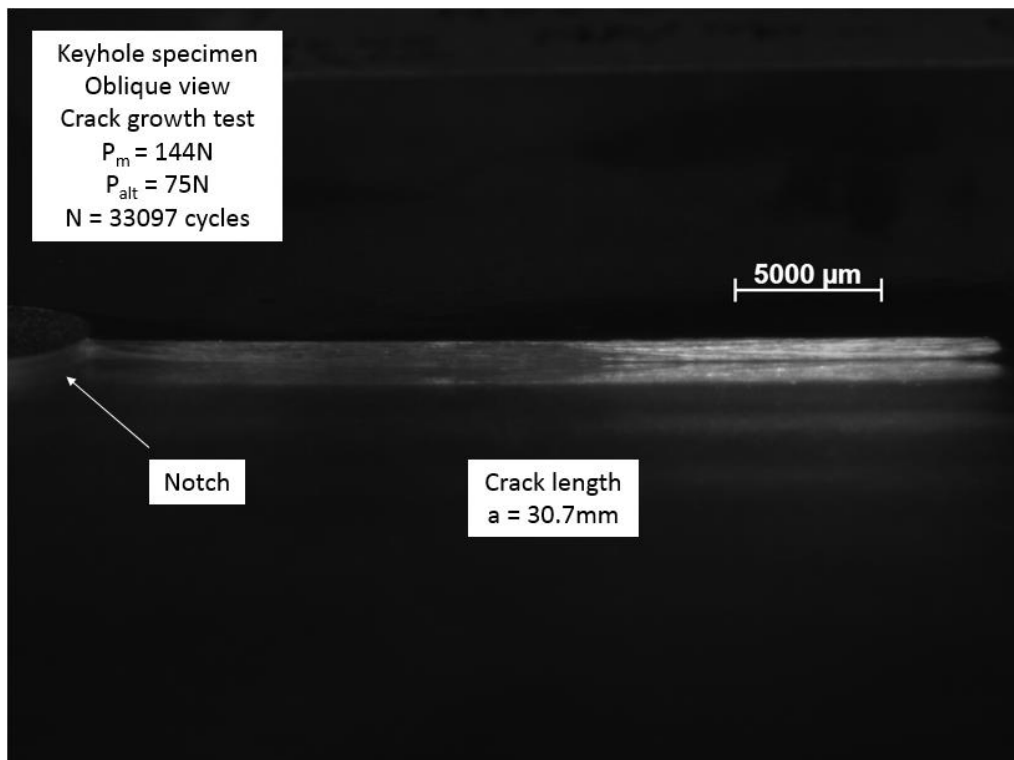


Figure A6.11: Fatigue crack propagated in a Keyhole specimen.

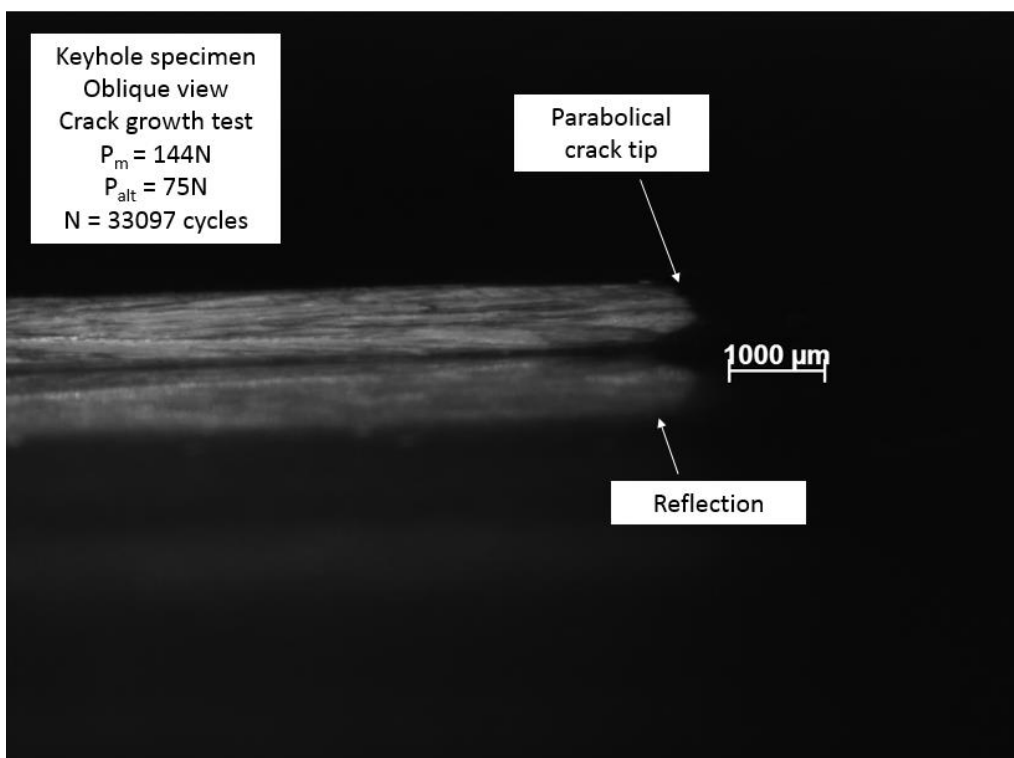


Figure A6.12: Fatigue crack propagated in a Keyhole specimen (Tip detail).

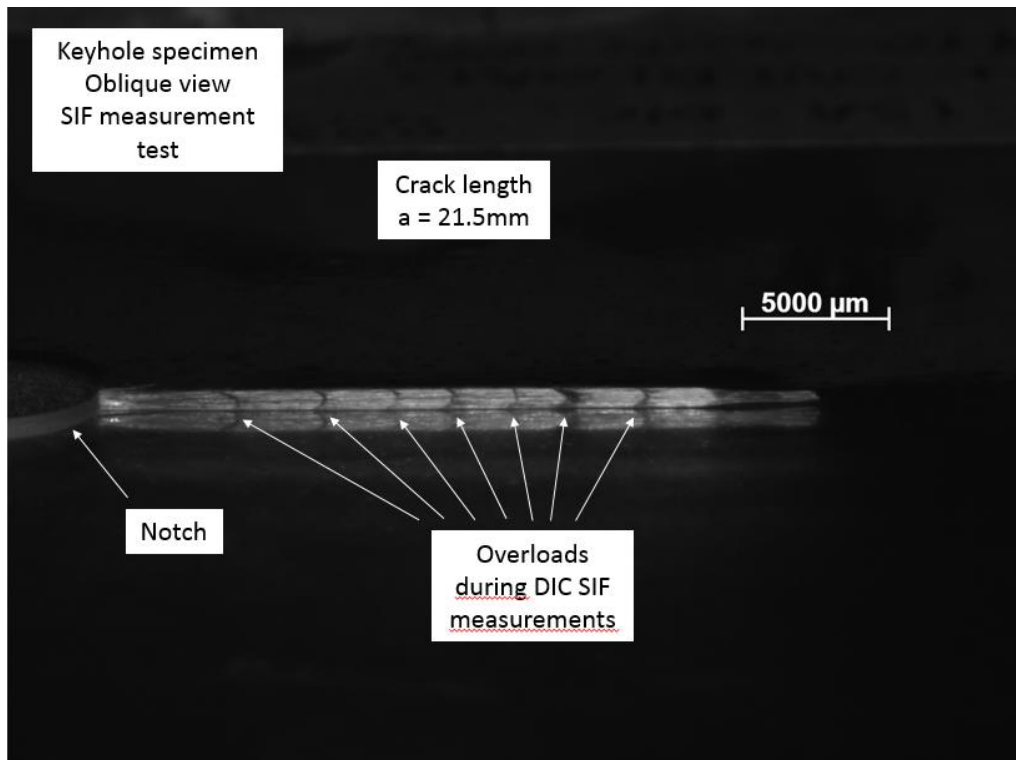


Figure A6.13: Fatigue crack propagated in a Keyhole specimen.

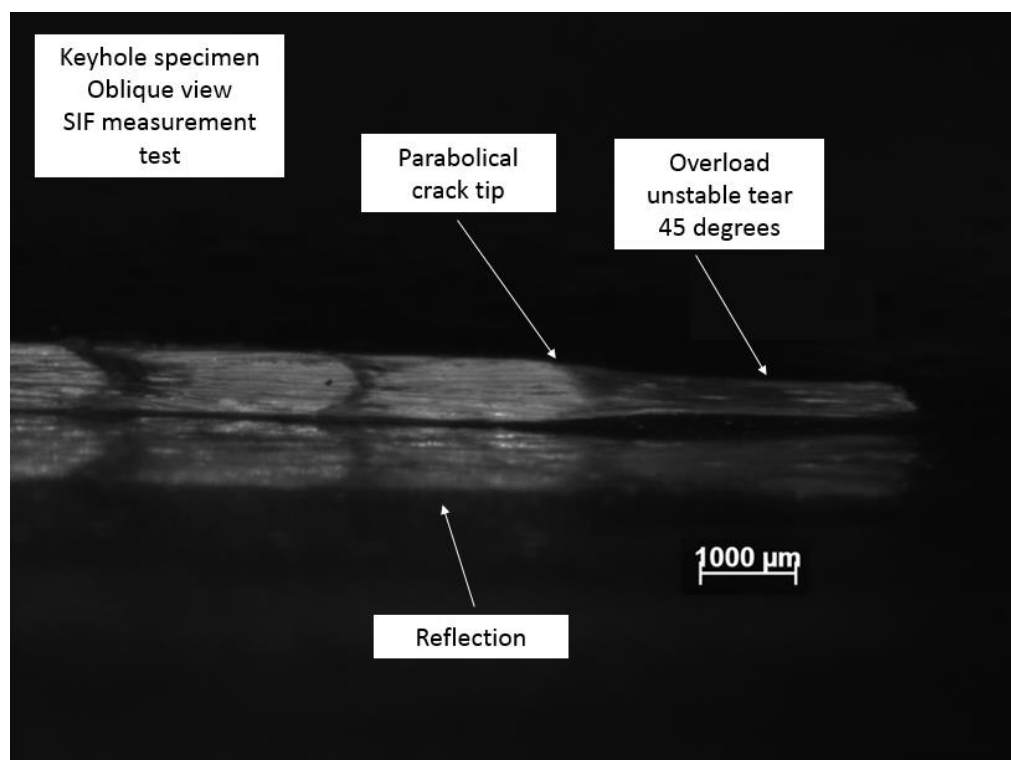


Figure A6.14: Fatigue crack propagated in a Keyhole specimen (Tip detail).

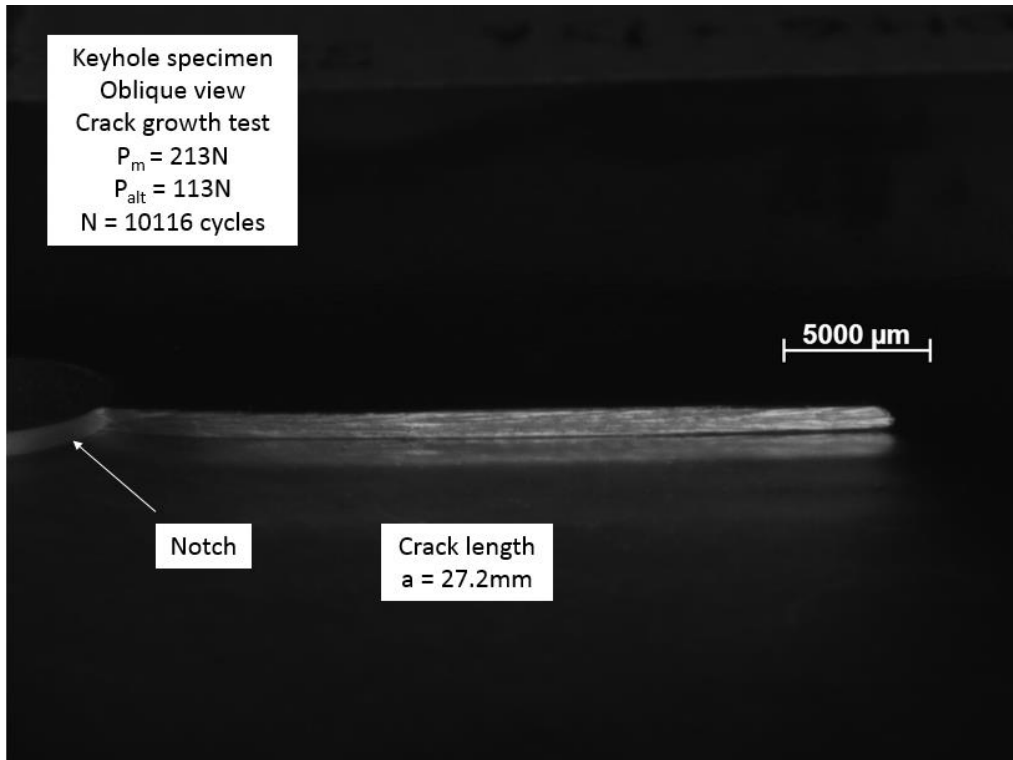


Figure A6.15: Fatigue crack propagated in a Keyhole specimen.

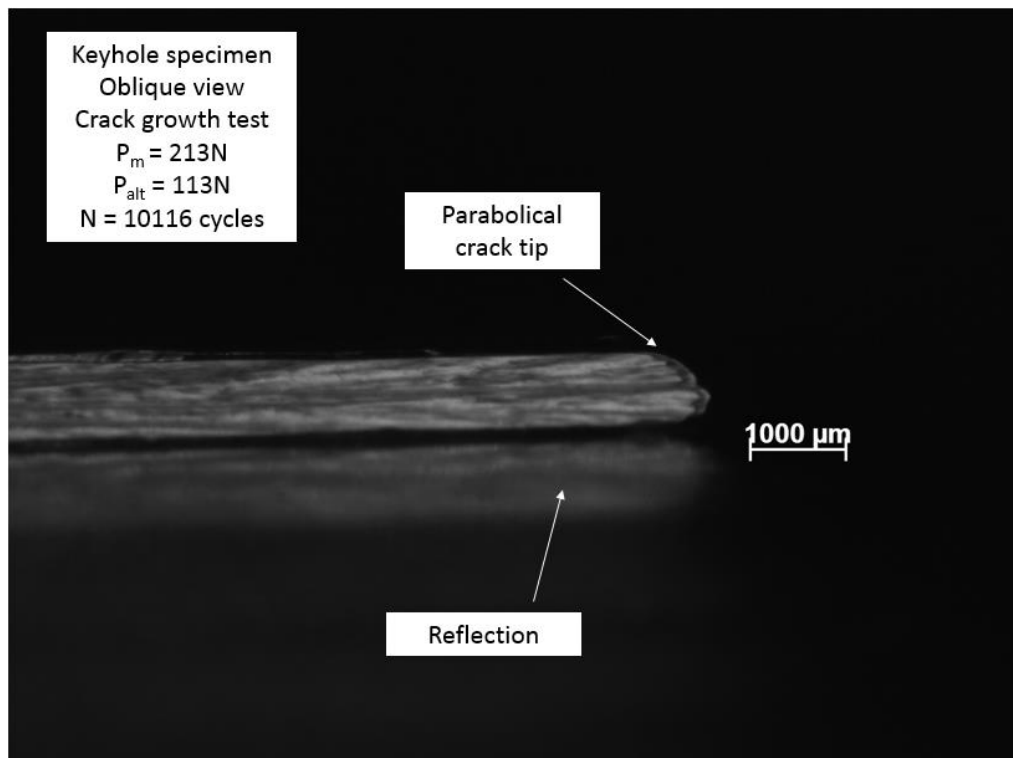


Figure A6.16: Fatigue crack propagated in a Keyhole specimen (Tip detail).

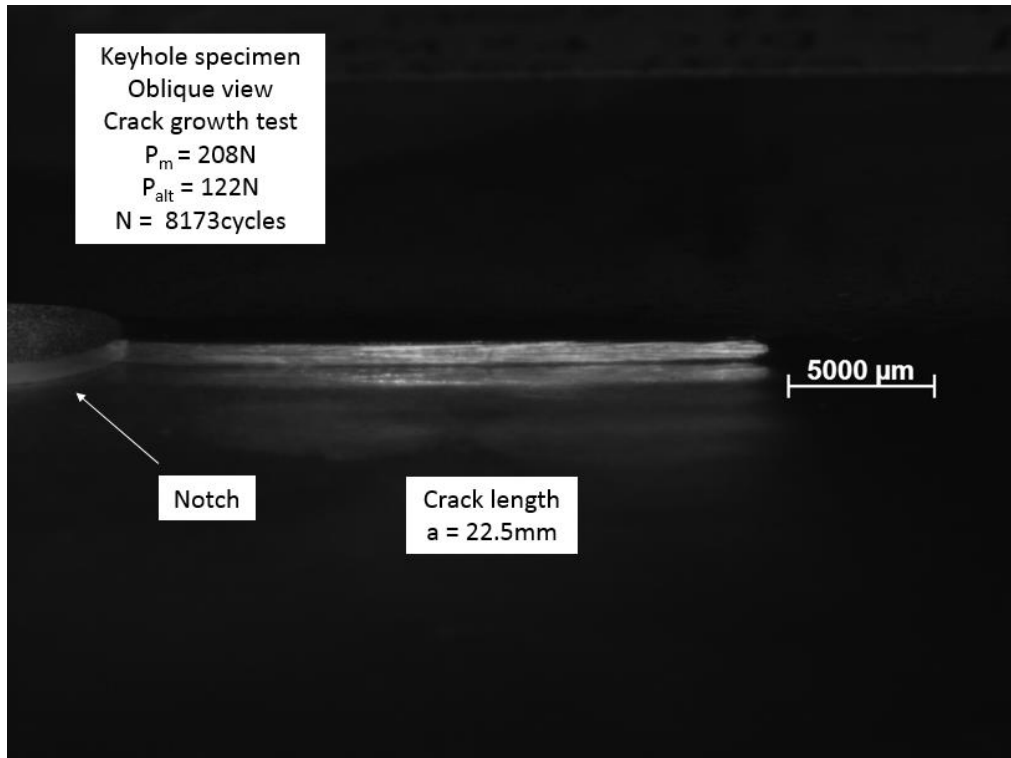


Figure A6.17: Fatigue crack propagated in a Keyhole specimen.

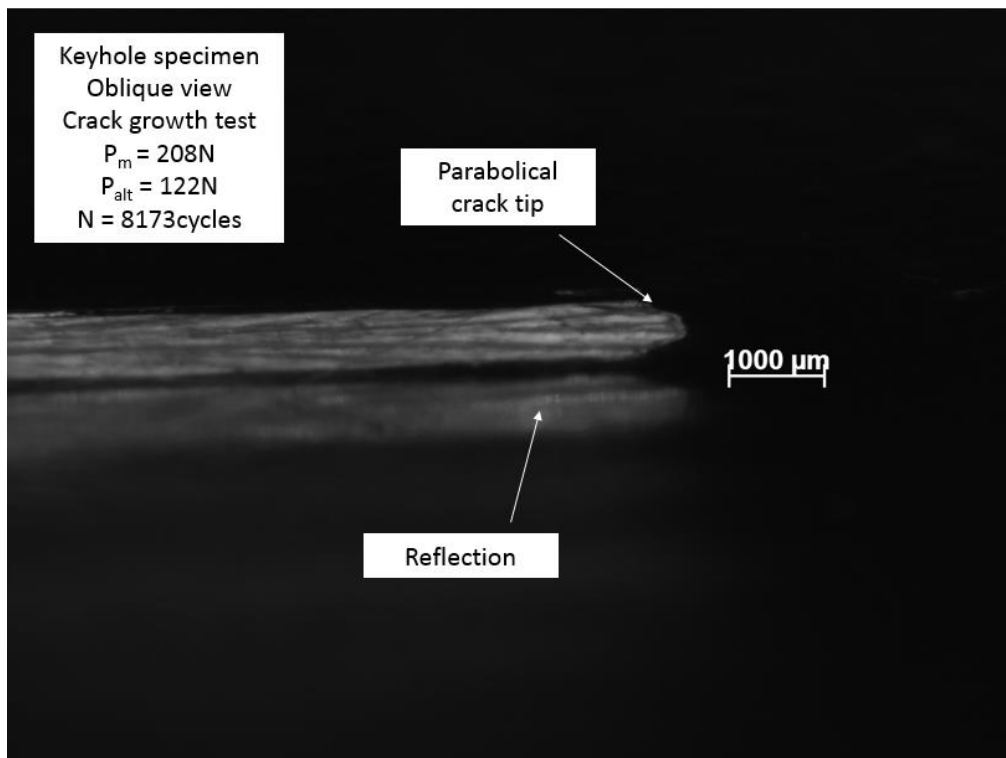


Figure A6.18: Fatigue crack propagated in a Keyhole specimen (Tip detail).

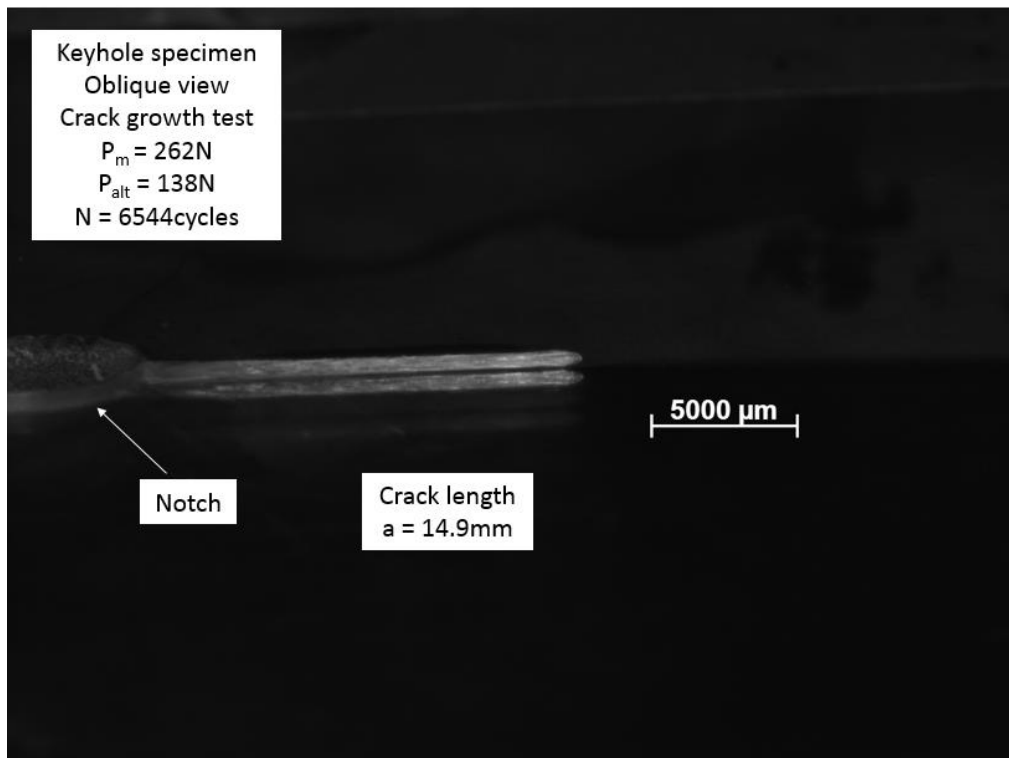


Figure A6.19: Fatigue crack propagated in a Keyhole specimen.

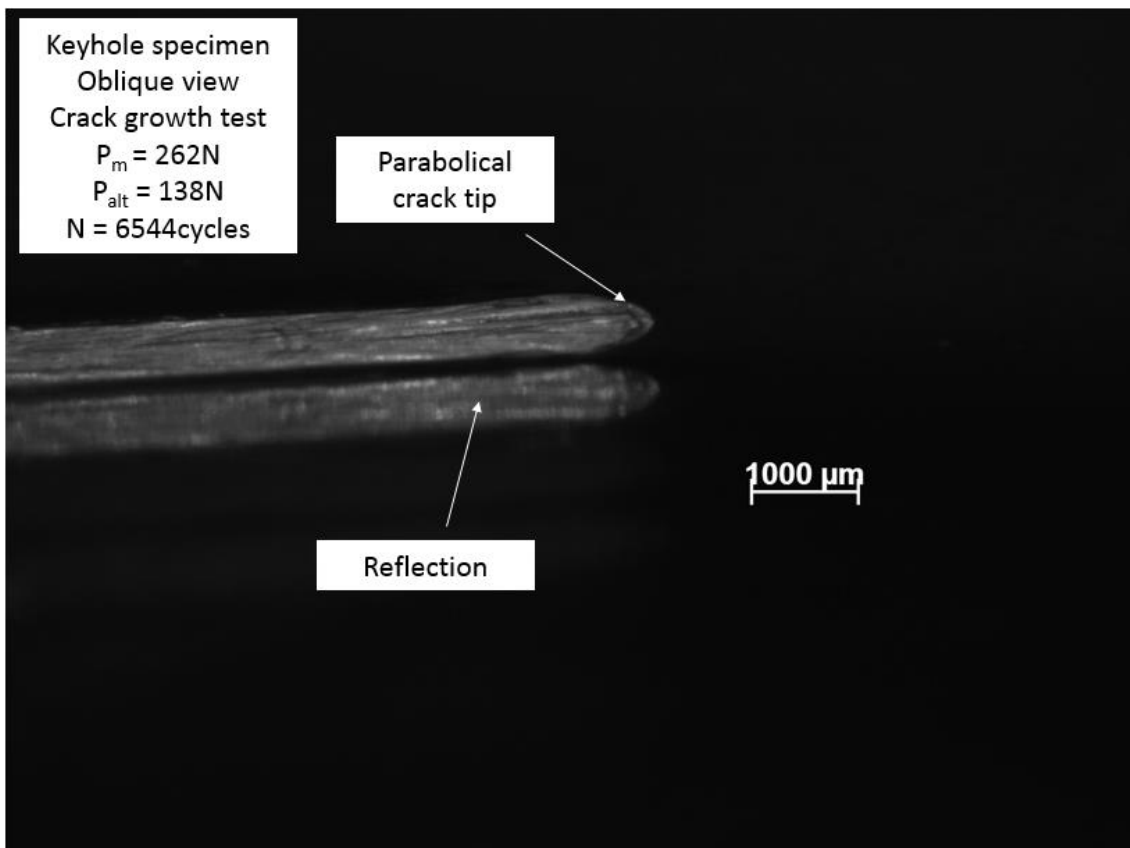


Figure A6.20: Fatigue crack propagated in a Keyhole specimen (Tip detail).

Fretting cracks

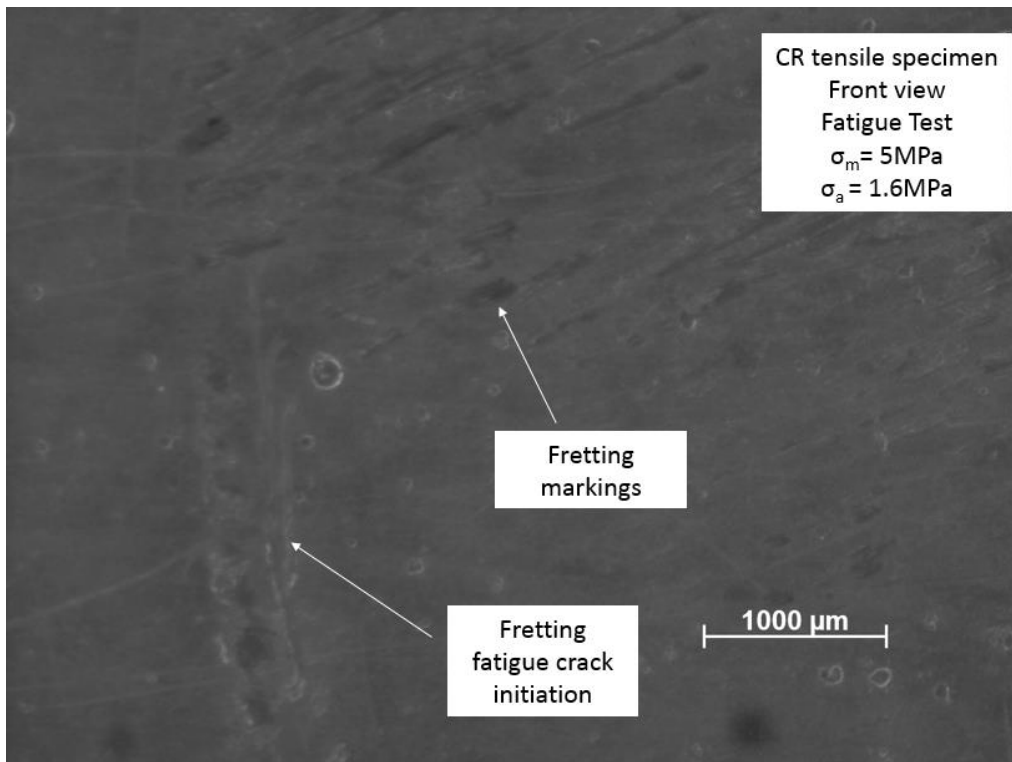


Figure A6.21: Fretting damage and crack initiation in a CR tensile specimen.

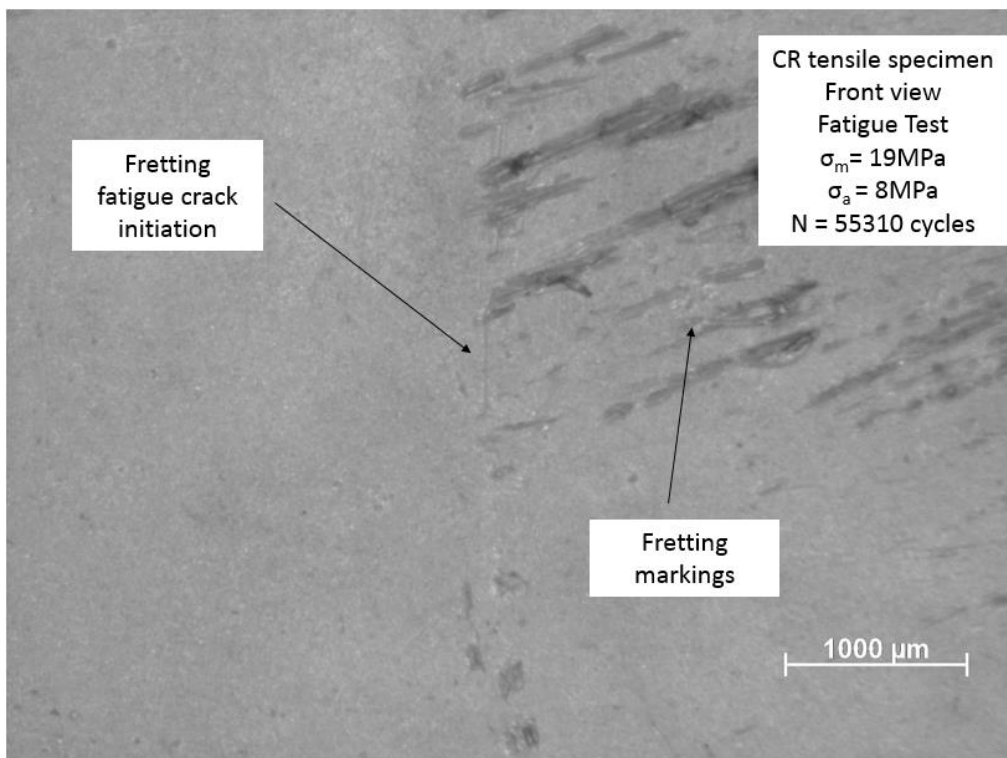


Figure A6.22: Fretting damage and crack initiation in a CR tensile specimen.

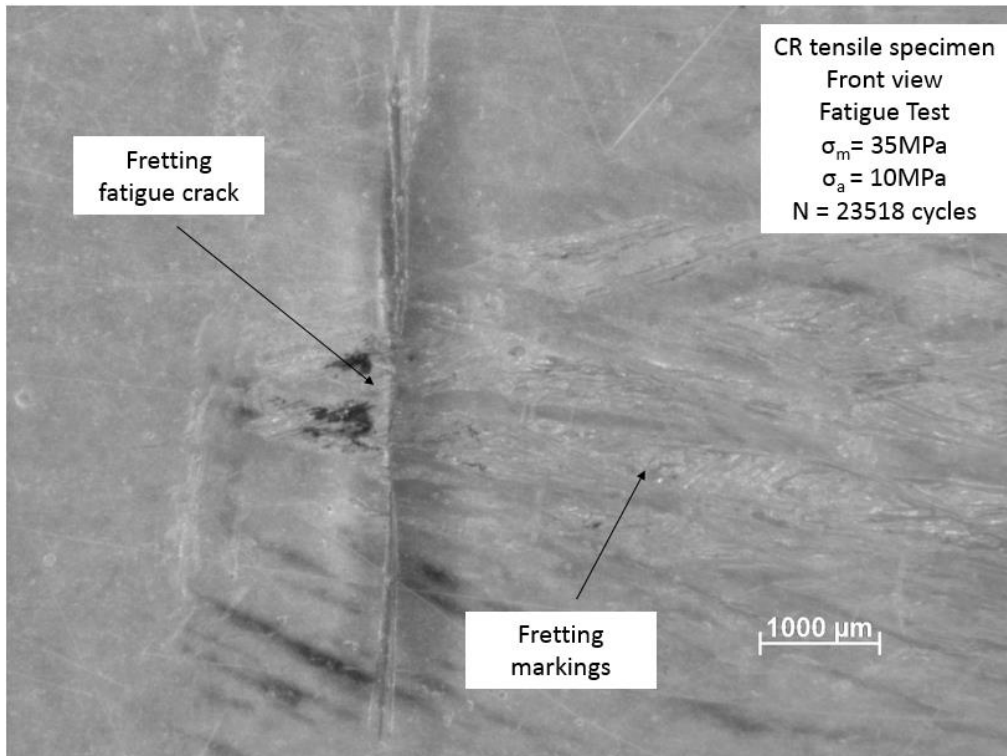


Figure A6.23: Fretting crack in a CR tensile specimen (front view).

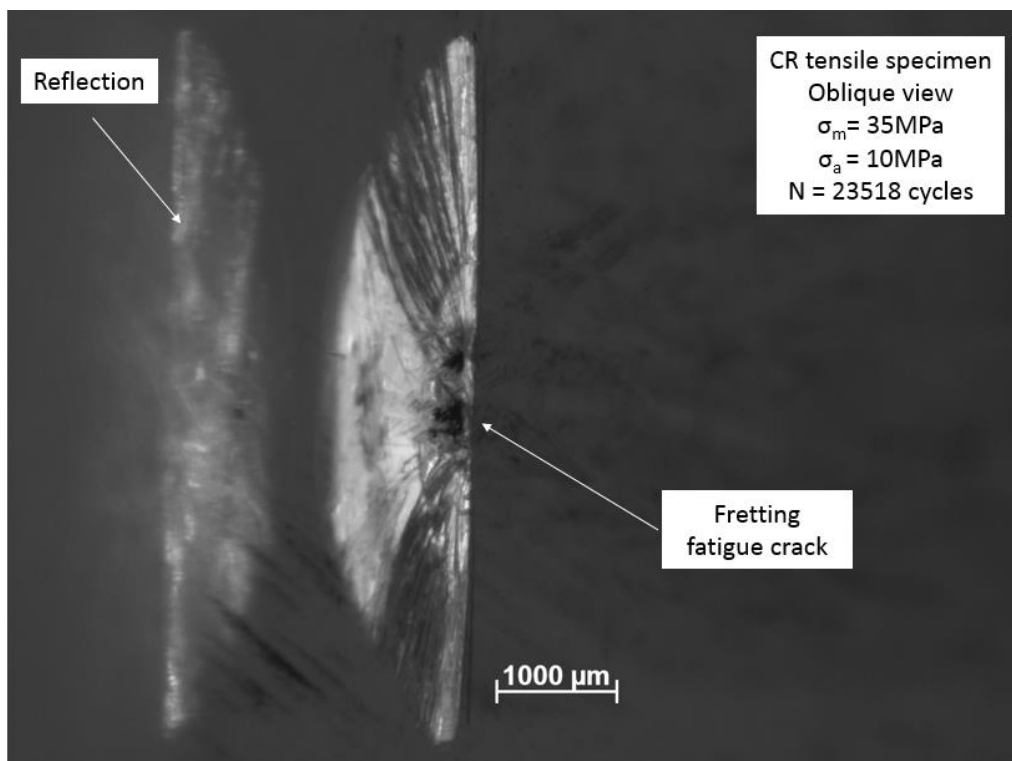


Figure A6.24: Fretting crack in a CR tensile specimen (oblique view).

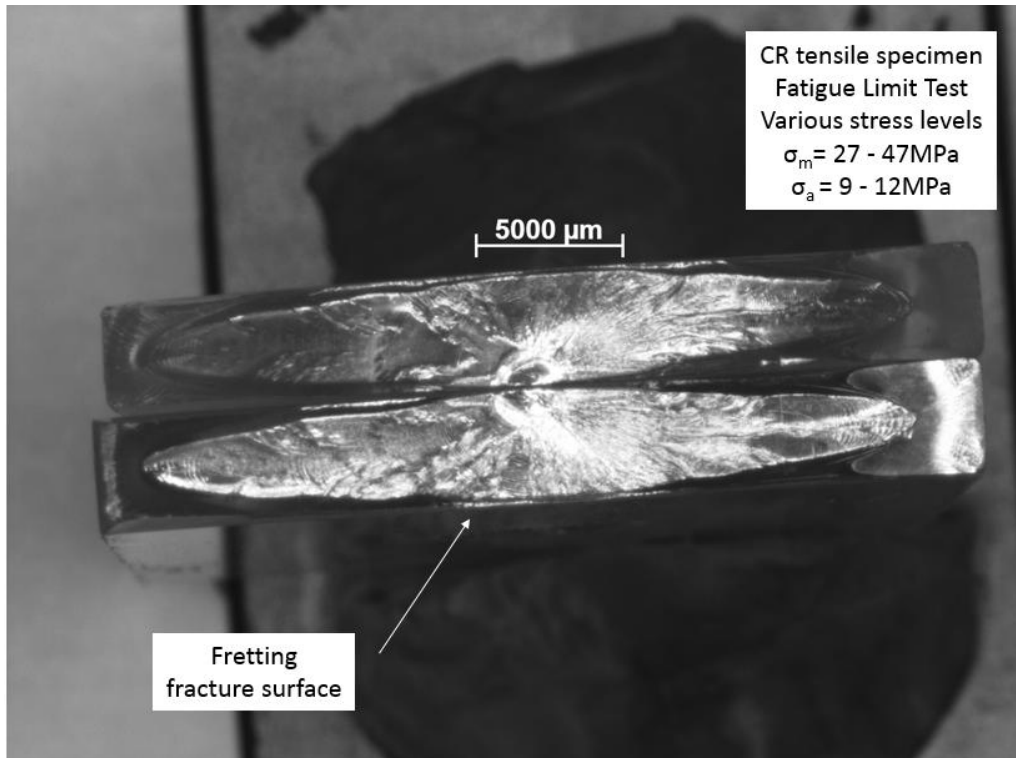


Figure A6.25: Fretting fracture surface.

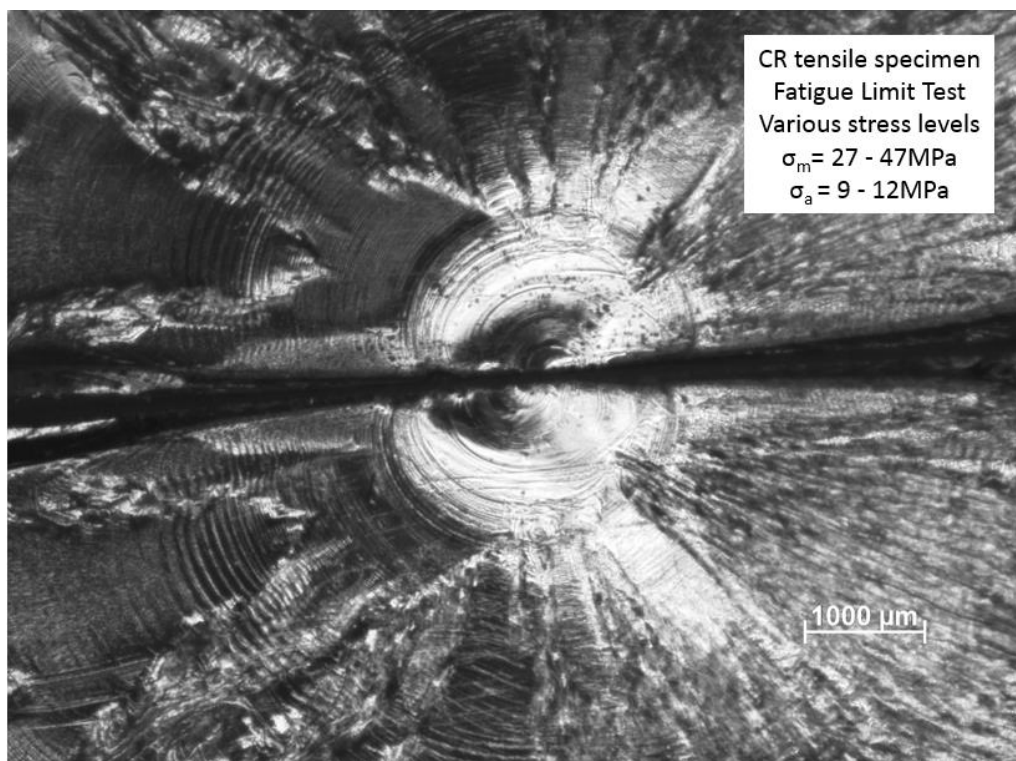


Figure A6.26: Fretting fracture surface (zoom).

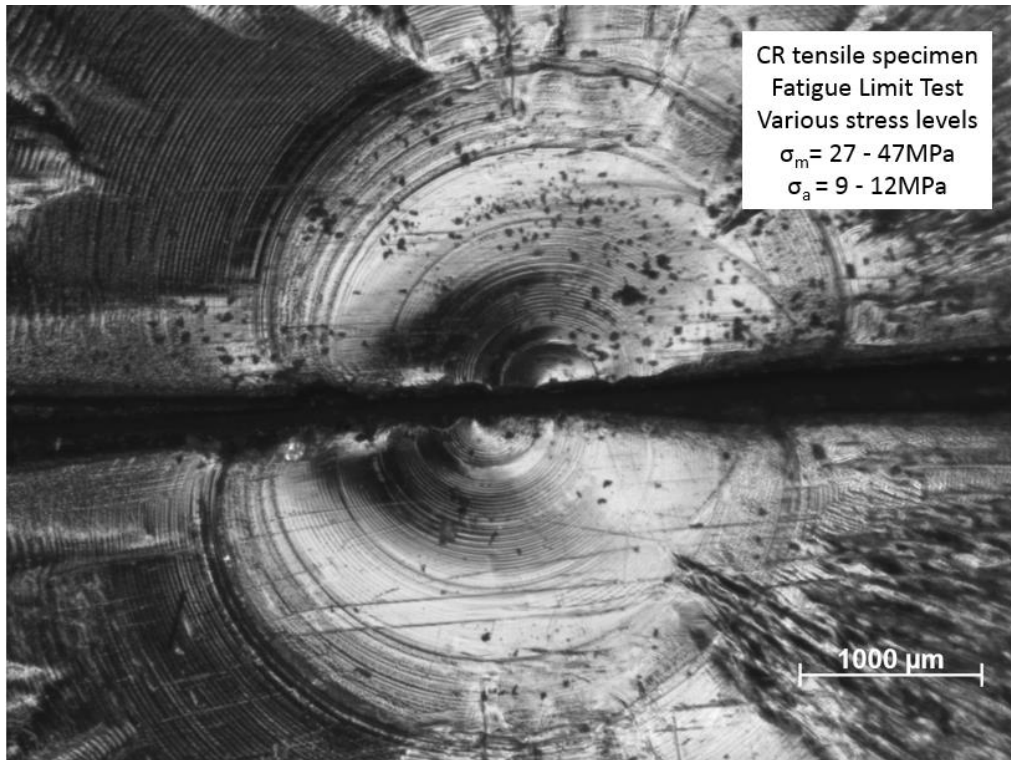


Figure A6.27: Fretting fracture surface (initiation detail).